

Air-based contactless actuation system for thin substrates

The concept of using a controlled deformable surface

Vuong, Phuc

DOI

[10.4233/uuid:2d375f1b-3857-4c03-87e8-cb0fc45f3f13](https://doi.org/10.4233/uuid:2d375f1b-3857-4c03-87e8-cb0fc45f3f13)

Publication date

2016

Document Version

Final published version

Citation (APA)

Vuong, P. (2016). *Air-based contactless actuation system for thin substrates: The concept of using a controlled deformable surface*. [Dissertation (TU Delft), Delft University of Technology]. <https://doi.org/10.4233/uuid:2d375f1b-3857-4c03-87e8-cb0fc45f3f13>

Important note

To cite this publication, please use the final published version (if applicable). Please check the document version above.

Copyright

Other than for strictly personal use, it is not permitted to download, forward or distribute the text or part of it, without the consent of the author(s) and/or copyright holder(s), unless the work is under an open content license such as Creative Commons.

Takedown policy

Please contact us and provide details if you believe this document breaches copyrights. We will remove access to the work immediately and investigate your claim.

AIR-BASED CONTACTLESS ACTUATION SYSTEM FOR THIN SUBSTRATES

THE CONCEPT OF USING A CONTROLLED DEFORMABLE
SURFACE

AIR-BASED CONTACTLESS ACTUATION SYSTEM FOR THIN SUBSTRATES

THE CONCEPT OF USING A CONTROLLED DEFORMABLE SURFACE

Proefschrift

ter verkrijging van de graad van doctor
aan de Technische Universiteit Delft,
op gezag van de Rector Magnificus prof. ir. K.C.A.M. Luyben,
voorzitter van het College voor Promoties,
in het openbaar te verdedigen op
maandag 03 oktober 2016 om 12:30 uur

door

Phuc Hong VUONG

Master of Science
Sungkyunkwan University, Korea
geboren te Binh Duong, Vietnam.

This dissertation has been approved by the

Promotor: Prof. ir. R. H. Munnig Schmidt

Copromotor: Dr. R. A. J. van Ostayen

Composition of the doctoral committee:

Rector Magnificus,
Prof. ir. R. H. Munnig Schmidt
Dr. R. A. J. van Ostayen

Chairman
Delft University of Technology
Delft University of Technology

Independent members:

Prof. dr. ir. F Al-Bender
Prof. dr. ir. J. van Eijk
Prof. dr. ir. P. Breedveld
Prof. dr. ir. J. L. Herder
Prof. dr. ir. J. Westerweel

University of Leuven
Delft University of Technology
Delft University of Technology
Delft University of Technology
Delft University of Technology



Copyright © 2016 by P. H. Vuong

ISBN 978-94-6186-714-8

Printed by: CPI-Koninklijke Wöhrmann – Zutphen

An electronic version of this dissertation is available at
<http://repository.tudelft.nl/>.

To my parents

PREFACE

A research project can start only when a question arises. Initially, the research question, which seemed to be magical to me at that time, was if it is possible to handle a thin object without touching it.

"Dear Prof. Van Ostayen, Prof. Munnig Schmidt, Prof. Spronck, Prof. van Eijk and Dr. Wesselingh,

Thank you for the great answer 'Yes' for the initial research question. I am going to go to Delft because I am so attracted by this research topic and by your work."

This was a letter that I could have written when I was appointed to this Ph.D. position.¹ My appreciation increased over time. Indeed, now I recognise that they had created a seed for me to grow this thesis.

Growing this thesis is a journey that, fortunately, I could have never done alone. Therefore I am trying to use words to express my deepest gratitude, which cannot be described fully by words, to those who have supported and accompanied me on this journey.

First of all, I would like to thank my supervisors, Prof. Rob Munnig Schmidt and Dr. Ron van Ostayen, for their effort and patience in guiding me to develop my research skills. I am glad that I have worked under their great supervision where I always had all the freedom in performing my research so that I was able to push my capabilities to their limit. Without them, my research would not have come this far, and my thesis would not have come to this point.

Ron, I always admire your knowledge in the field of Tribology and your enthusiasm for this research. With these, you helped me to start smoothly, even though the topic is in a field that was totally new to me at that point. During the years, you have always been by my side in this research. I still remember the weekend that we had quite a long discussion through emails when I started with my finding of different sets of optimal design parameters. It amazed me. Your enthusiasm, knowledge and experience have had a major impact on me, on my research, and on my thesis, thank you.

Rob, I have been fortunate to be one of your students. Firstly, with your lectures of the 'Mechatronic system design' course and your book, you have brought me to a new level of my knowledge about mechatronics where the bridge between mathematical equations and the physical world becomes clearer to me than ever. Secondly, with your managing experience, your advice has always been very valuable, particularly for me to organise my research and to keep it on track. I would like to thank you for your contribution to my development of personal skills as well as to the success of my research project.

I would like to thank Ir. Jo Spronck, who had a great contribution to the result of this work. Jo, there are always in my mind the images of the interview meeting in Korea, in

¹At that time I used the initial 'Prof.' for all the supervising staff members.

which you were very open and supportive. I appreciate your support for the decision of appointing me to this PhD position. Although we did not have a lot of discussions during my research, I have learned a lot from you, especially about the various approaches that you use to solve problems, thank you.

I have spent most of my time at TU Delft surrounded with my fellow PhD colleagues, Jan Schutten, Rudolf Saathof, Ruijun Deng, Oscar van de Ven, Johan Vogel, Takeshi Morishima and Arjan Meskers. I wish to thank them all for forming a pleasurable environment that let me enjoy every single day in the last four and a half years. Especially, Johan, Oscar and Ruijun, thank you for your effort in making our office enjoyable still in the last year, even though we were all in the most stressful period.

Jan, I will never forget the great period that we worked together at the beginning of my journey. I appreciate your effort in helping me to get acquainted quickly with the new environment. Oscar, thank you so much for being the person that I usually go to with a question on how to do anything, for instance using a new piece of software or with a sensor in our lab. Johan, you always amaze me with your knowledge and your aspiration for sharing knowledge. I appreciate every piece of information given by you during the sightseeing trips that we both have joined, e.g. to Zaanse Schans, Amsterdam, Dordrecht. Also, I should not forget to send you many thanks for your help in translating the Summary of my thesis and the Propositions into Dutch.

I also wish to thank the technical support staff, Rob Luttjeboer, Harry Jansen, Patrick van Holst, Nisse Linskens and Hans Drop, for their contribution to all the experimental setups. Without them, it would have taken much longer for me to accomplish this research project.

It would have been very tough if I stayed in Delft without my friends from the Vietnamese Community in Delft. Therefore, I am grateful to them for bringing me the feeling that Vietnam is not that far from here.

Deeply from my heart, I want to thank my parents and family for their love, support, and encouragement that have always been present. Words are not sufficient in this case. Therefore, I dedicated this thesis to them, to express not only my gratitude but also the saying that I love them.

Finally, I wish to thank my wife Ho Xuan Thao Nguyen for her love that has been the strongest inspiration for this accomplishment. Thao Nguyen, I would like to let you know that your contribution to this thesis is more than mine. Without you, this thesis would not have been here.

*Vuong Hong Phuc
Delft, August 2016*

CONTENTS

Summary	1
1 Introduction	5
1.1 Motivation	5
1.2 Different contactless actuation principles.	9
1.3 Research objective	17
1.4 About this thesis	17
2 Concept exploration and comparison	19
2.1 Actuation using an air film	19
2.2 Different concepts	21
2.2.1 Pressure variation concept	21
2.2.2 Deformable surface concept	22
2.3 Optimal design	25
2.3.1 Step surface analysis	27
2.3.2 Tilt surface analysis	32
2.4 Comparison.	35
2.4.1 Motor function comparison	35
2.4.2 Bearing function comparison	36
2.5 Conclusion	40
3 Numerical model and experimental validation	41
3.1 The tilted air bearing experiment	41
3.1.1 Setup description	41
3.1.2 Experimental result	44
3.2 Numerical model development	46
3.2.1 Model improvement - nonlinear restriction	46
3.2.2 Model improvement - substrate deformation coupling	47
3.3 Conclusion	51
4 Actuator design for a three planar DoF system	53
4.1 Actuator design for a three DoF system	53
4.1.1 Effect of actuator shape	54
4.1.2 Effect of inlet and outlet area.	56
4.1.3 Minimise the flow for a required force	58
4.2 Static performance of a three DoF system.	61
4.3 Conclusion	64

5 Flowerbed - design decisions and manufacturing	65
5.1 Contactless actuation system - Motion control	65
5.1.1 Limiting factors of motion control performance	65
5.1.2 Motion control using a contactless actuation system	67
5.2 Thin film flow dynamics	69
5.3 Mechanical structure of the flowerbed	74
5.3.1 Design decisions	74
5.3.2 Flowerbed construction	84
5.3.3 Mechanical dynamics	86
5.4 Predicted overall dynamics performance	90
5.5 Conclusion	91
6 Dynamic behaviour validation	93
6.1 Setup description	93
6.2 Mechanical dynamics validation	95
6.2.1 Preliminary resonance test.	95
6.2.2 Transmissibility from plate position to flower angle	96
6.3 Dynamic response of the force	100
6.4 Conclusion	105
7 Conclusions and recommendations	107
7.1 Conclusions.	107
7.2 Recommendations	109
7.2.1 Recommendations on Flowerbed	110
7.2.2 General recommendations on the principle	110
A Overview of previous research	113
A.1 Contactless actuation using an active air film	113
A.1.1 Motor Function	113
A.1.2 Bearing Function	116
A.2 Contactless wafer positioning stage.	118
A.2.1 Multi-DoF contactless actuation system	118
A.2.2 Contactless wafer positioning stage	118
A.3 Conclusions and recommendations from previous research	126
B Clamping module - the third method of force control	127
Nomenclature	129
References	131
Curriculum Vitæ	137
List of Publications	139

SUMMARY

A commercial product is made from components that are processed through several steps in a factory. In industry, there are demands to move an object, from one processing stage to another one, or within a processing stage, e.g. milling, printing, engraving. The topic of this thesis is the controlled movement of an object. The targeted objects here are thin substrates such as silicon wafers, solar cell wafers and glass sheets. Being very fragile, this type of substrate requires to be highly cared for while handling. Furthermore, due to the characteristics of the industries in which these substrates are used, a very high level of cleanliness of the substrates is required. Currently, mechanical contact between handling tools and substrates is identified to be one of the main factors that causes breaking failures and contamination. Therefore, it is demanded to have a handling system that is able to move thin substrates without mechanical contact.

In 2006, a new principle of contactless actuation was invented by Van Ostayen at TU Delft, that was aimed for the demand described above. Similar to a conventional air bearing, this principle uses a thin air film to levitate the substrate. Its distinguishing feature is the modified bearing surface that allows the viscous traction force created by the air film flow to be controllable and to be sufficient to move the substrate. Studying this principle, research had been conducted by Wesselingh in the period from 2007 to 2011. During this research, this principle was proven to be very promising. It was judged to be highly applicable for the targeted industries, and thus could be brought to the market.

To bring this principle to the market, the first step that should be made is to gain more knowledge about the principle so that industrial requirements can be translated and converted into a design of a contactless handling system with confidence. Gaining more insight is determined to be the goal of the research presented in this thesis. To be exact, the research goal is phrased as following: "*Exploring the principle by investigating different potential concepts, studying the achievable performance regarding two main aspects: the ratio of force to flow rate, and the dynamic response in terms of force*".

Serving this goal, the research starts by searching for different concepts that can be used to control the propulsion force created by such a system. The performance of these concepts is then evaluated and compared. Since one of the purposes of this principle is to prevent contamination of fragile and susceptible products, the air used in this system must be clean. Because clean air is costly, the performance is defined as the ratio of the force to the flow rate. In order to evaluate the performance of the potential concepts, an analytical model has been developed. Based on this model, the actuator geometry is optimised such that the ratio of the force to the flow rate can be maximised. Finally, using the optimal geometry, a comparison between different concepts can be performed and has been presented.

In order to have a more accurate prediction, a numerical model is also developed, based on the same set of equations used in the analytical model. This model has been verified successfully with an experimental setup, studying the statically tilted air bearing.

The results show that the prediction is very accurate, not only for the force and the flow but also for the pressure distribution and the substrate deformation. Furthermore, with this setup, using just approximately 50% of the available area, the acceleration achieved on a 100 mm wafer has exceeded 10 m s^{-2} .

Next to the study on static performance, this research also focuses on enhancing the dynamic performance of this type of contactless actuation system. For a controlled motion application, a fast response of the force from the command is desired. Any delay in this response will result in a lower achievable bandwidth of the closed loop controller. It has been learned from the former research that the biggest delay is caused by the slow air flow dynamics inside the manifold, which is used to connect the controlling valves and the actuator array. In this research, instead of valves, the controlling elements are proposed to be the bearing surface itself. The propulsion force is controlled by means of deforming the bearing surface, i.e. tilting the actuator. Since the controlling element is located at the position where the propulsion force is actually generated, the force response is expected to be fast.

In order to control the deformation of the bearing surface, a mechanism has been proposed. Based on this, an experimental setup, which is called 'Flowerbed', has been designed and realised. From the modelling prediction, the achievable force bandwidth of Flowerbed is approximately 1000 Hz. However, due to practical limitations of the experimental setup and the measuring equipment, the bandwidth can be verified up to 400 Hz. Compared to the demonstrator developed in the previous research, the dynamic force response has been improved, even with the increased size of the system.

SAMENVATTING

Een commercieel product wordt samengesteld uit componenten die in een fabriek in verschillende fases zijn bewerkt. Vanuit de industrie is er uiteraard vraag naar het verplaatsen van een object van de ene procesfase naar de volgende of het verplaatsen binnen een procesfase, bijvoorbeeld bij frezen, printen, graveren en dergelijke. Het onderwerp van deze thesis is het gecontroleerd verplaatsen van een object. De objecten waar het hier om draait zijn dunne substraten, zoals siliciumplakken, zonnecelplakken en glasplaten. Vanwege hun breekbaarheid dienen dergelijke substraten zorgvuldig te worden gehanteerd. Daarbij moeten de substraten, vanwege de aard van de industrie waarin ze gebruikt worden, zeer schoon gehouden worden. Momenteel wordt het mechanisch contact tussen de hanteerhulpmiddelen en de substraten gezien als één van de hoofdoorzaken die breukfalen en contaminatie veroorzaken. Vandaar dat er behoefte is naar een hanteersysteem dat de dunne substraten kan verplaatsen zonder mechanisch contact. In 2006 werd er door Van Ostayen aan de TU Delft een nieuw principe voor contactloze actuaties uitgevonden dat zich richtte op de hierboven beschreven behoefte. Net als een conventioneel luchtlager gebruikt dit principe een dunne luchtlaag ter levitatie van het substraat. Verschillend is echter het gemodificeerde lageroppervlak, dat het mogelijk maakt de viskeuze tractiekracht, die veroorzaakt wordt door de stroming in de luchtlaag, te regelen en voldoende sterk te maken om het substraat te verplaatsen. Onderzoek rond dit principe werd uitgevoerd door Wesselingh in de periode van 2007 tot 2011. Tijdens dit onderzoek werd aangetoond dat dit principe zeer veelbelovend is. Het werd geacht zeer toepasbaar te zijn in de beoogde industrie en daarom potentie te hebben als product op de markt. Om het principe op de markt te brengen moet als eerste stap meer kennis omtrent het werkingsprincipe vergaard worden, zodat de industriële vereisten kunnen worden vertaald en omgezet in een ontwerp van een betrouwbaar contactloos hanteersysteem. Het verkrijgen van meer inzicht is het doel van het onderzoek dat gepresenteerd wordt in deze thesis. Meer precies kan het doel als volgt geformuleerd worden: "Het in kaart brengen van het principe door het onderzoeken van verschillende potentiële concepten, bestuderend de haalbare prestaties voor wat betreft twee hoofdaspecten: de verhouding tussen kracht en stroomsnelheid en de dynamische responsie in termen van kracht". Om dit doel te bereiken start het onderzoek met het zoeken naar verschillende concepten die gebruikt kunnen worden om de door het systeem voortgebrachte voortstuwingskracht te regelen. De prestaties van deze concepten zijn vervolgens geëvalueerd en vergeleken. Omdat één van de doelen van dit principe het voorkomen van de contaminatie van breekbare en gevoelige producten is, moet de lucht die gebruikt wordt in het systeem schoon zijn. Omdat schone lucht duur is wordt de prestatie gedefinieerd als de verhouding tussen de kracht en de stroomsnelheid. Om de prestaties van de potentiële concepten vast te kunnen stellen is een analytisch model ontwikkeld. Gebruikmakend van dit model is de geometrie van de actuator zodanig geoptimaliseerd dat de verhouding tussen kracht en stroomsnelheid kan

worden gemaximaliseerd. Tenslotte kan met behulp van deze optimale geometrie een vergelijking tussen de verschillende concepten gemaakt en gepresenteerd worden. Om een meer accurate voorspelling te verkrijgen is er ook een numeriek model ontwikkeld, gebaseerd op dezelfde vergelijkingen als die gebruikt worden in het analytische model. Het numerieke model is succesvol geverifieerd aan de hand van een onderzoekopstelling waarin luchtlager werd bestudeerd terwijl deze statisch gekanteld was. De resultaten tonen aan dat de voorspelling zeer nauwkeurig is, niet alleen voor wat betreft de kracht en de luchtstroming, maar ook voor wat betreft de drukverdeling en de vervorming van het substraat. Verder werden met de opstelling, gebruikmakend van slechts ongeveer 50Naast het bestuderen van de statische prestaties concentreert dit onderzoek zich ook op het verbeteren van de dynamische prestaties van dit type contactloze actuatuatiesysteem. Voor toepassingen waarin de beweging geregeld wordt is een snelle responsie van de kracht op een bewegingsopdracht gewenst. Elke vertraging van de responsie leidt tot een verlaging van de haalbare regelbandbreedte van de gesloten-lus-regelaar. In het voorgaande onderzoek is ontdekt dat de voornaamste vertraging wordt veroorzaakt door de langzame stromingsdynamica van de luchtstroom in het verdeelstuk dat de regelventielen en de matrix van actuators met elkaar verbindt. In dit onderzoek wordt voorgesteld om, in plaats van ventielen als regelementen, gebruik te maken van het lageroppervlak zelf. De voortstuwingskracht wordt dan geregeld door middel van het vervormen van het lageroppervlak; dat wil zeggen, door het onder een hoek brengen van de actuator. Omdat het regelement geplaatst is precies daar waar de voortstuwingskracht wordt voortgebracht, is een snelle responsie te verwachten. Er is een mechanisme om de vervorming van het lageroppervlak te regelen voorgesteld. Op basis hiervan is een onderzoekopstelling, het zogenaamde 'Bloemperk' ontworpen en gerealiseerd. De te behalen krachtbandbreedte van het Bloemperk, die op basis van modelvoorspellingen verwachtte wordt, ligt ongeveer bij 1000 Hz. Vanwege praktische beperkingen van de onderzoekopstelling en de meetapparatuur kon de bandbreedte tot 400 Hz worden geverifieerd. In vergelijking met de opstelling ontwikkeld in het voorgaande onderzoek is de dynamische responsie verbeterd, terwijl de afmetingen van het systeem juist werden vergroot.

1

INTRODUCTION

In industry, there are demands to move an object, from one processing stage to another one, or within a processing stage, e.g. milling, printing, engraving. In semicon industry and solar cell industry, thin silicon substrates are the objects that need to be moved. Being very fragile, this type of substrate requires to be highly cared for while handling. Furthermore, due to the characteristics of the industries in which these substrates are used, a very high level of cleanliness of the substrates is required. Additionally, under the pressure of reducing production costs, there is a trend towards the use of thinner and larger substrates. Consequently, handling these substrates becomes more challenging, thus new handling tools need to be developed. The work presented in this thesis is a study on one of the new principles of handling thin substrates, that is to employ the viscous traction force of a thin air film flow to drive the substrates.

In this introductory chapter, first, some examples are illustrated, presenting industrial demands and interest as a motivation for the research on this principle in developing a contactless actuation system. Followed, a brief section describes different available principles that have been researched in this field. Finally, the main question for the research presented in this thesis is proposed.

1.1. Motivation

It is true that in nature, every thing is moving, from a small thing such as an electron to a big thing such as a planet. It is not possible to find the reasons for the movement of every thing. However, from a personal perspective, a reason for several things to move could be to get work done. People are moving themselves to have their work done. Also people are moving things to get their work done. To the author of this thesis, understanding and controlling motion of things are of great interest, that leads him into this research.

In industry, components are moved and processed in a factory in order to be built to a final product. Hereafter, the term 'transport' is used to refer to the action of moving objects between different processes, e.g. on a conveyor. Whereas the term 'positioning' is for the action of driving an object to reach a designed position or to follow a

pre-defined trajectory in a process such as printing, cutting, milling, bonding etc. The definitions of transport and positioning are different since the purposes are different, however, they both have the same qualitative requirement: objects' motion need to be controlled. Then the term 'handling' is used to refer to the action of controlling objects' motion in general.

Looking into the history of industry development, the demand for handling objects has existed for a very long time. Pyramids could not have been there if there was not a method to move and place construction stones into position. Because of this huge demand, many principles have been invented and applied in industry. For transport, frequently the principle of using belts and/or rollers can be found. In some cases, especially when the handled object is not fragile and can easily be polluted e.g food industry, and chemical industry, employing vibrating conveyors has been considered to be the best option. For some specific tasks, where orientation and precision are highly required, a robot can be used as a transporter. Similarly for positioning, various systems have been developed for this purpose. Depending on the requirements of the working space and precision level, different concepts have been used, from motors and screw drives for a large positioning stage in a CNC machine to piezo actuators and compliant mechanism for a small stage of a microscope.

Since the world keeps moving, new products come into life, thus new demands for handling objects arise continuously. The targeted objects of the handling principle presented in this thesis are thin substrates. These require to be highly cared while handling since they are fragile and susceptible to being polluted. In order to illustrate the new demand of handling such an object, following, two examples are presented.

The first example is in semiconductor industry where integrated circuits are produced. Most of the processes in this industry deal with silicon substrates, which are called 'wafers'. Typically, after being sliced from a grown mono-crystalline cylindrical ingot, a wafer has an diameter of 300 mm with a thickness of about 0.75 mm (Figure 1.1a). Then it goes through several processing steps (up to hundreds of steps) before being cut into small pieces and packaged into final chips. Nowadays, the smallest feature of a chip is 14 nm (data in 2014). Moreover, effort is being made in order to achieve even smaller feature size [5]. Consequently, the cleanliness level of the fabricating environment is required to be higher and higher due to the fact that smaller features are more susceptible to contamination. Because of this, all the possible contamination sources are being examined. As stated in [7], mechanical contacts between wafers and handling tools have been identified to be one of the contamination sources.

Even though the front side of the wafer has been treated and monitored carefully regarding its cleanliness, about 0.5-1% yield loss of product is incurred with a systematic pattern shown in Figure 1.1b. As explained in [7], small amounts of metal-ion contamination have been created on the back side of wafers due to mechanical contacts with handling tools, e.g. the three lift pins. During some processing steps, 30% off this contamination is transferred from the back side of a wafer to the front side of another one. This impact has been observed even when the stainless steel lift pins are exchanged by non-metallic pins. Different solutions have been considered to solve this problem. Of course, from the author's point of view, an obvious solution is to develop handling tools for wafers that do not require any mechanical contacts.

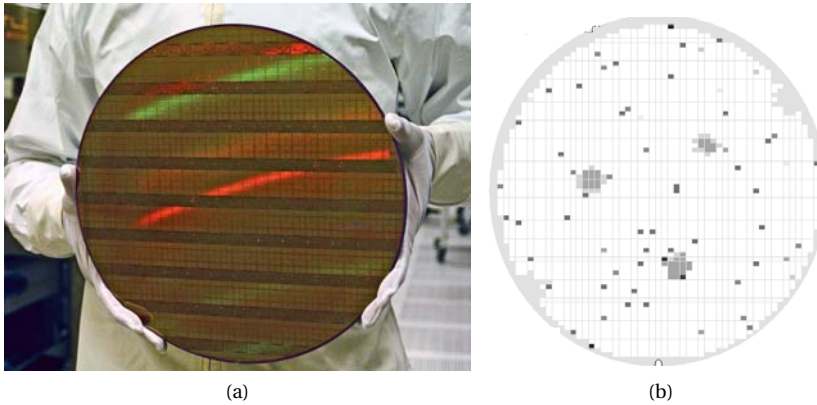


Figure 1.1: A 300 silicon wafer used for making chips (source Intel) (a), An example pattern of failures caused by particles originated from mechanical contacts (source [7])(b)

The second example illustrating the demand for contactless handling systems is in solar cell industry. In this field, the main driver is not the feature size but the cost reduction. Still, avoiding contamination is important, but less a problem compared to the previous example. Instead, the concentration is focused on the efficiency of material use, of which silicon material contributes approximately 57% to the cell price nowadays (data in 2014) [1]. It is obvious that a more efficient use of silicon can be achieved by reducing the thickness of the silicon substrate. This is the reason why the decreasing trend of the silicon substrate thickness has been recorded in the period 1990-2014, which is shown in Figure 1.2. In this graph, it can be observed that the thickness has not been reduced in the period 2008-2014. As explained in [1], because of the lower market prices for silicon substrate, the same thickness has been preferred to be used in order to not increase the breakage on production lines. However, as shown in Figure 1.3, the reducing trend of substrate thickness is predicted to continue in the next period due to the expected tight silicon market situation. As mentioned explicitly in [1], one of the requirements for the enabling of thickness reduction is to have innovative handling concepts. Again, the handling principle presented in this thesis is highly promising for the applications in this field.

Presented above are just two examples illustrating some of the advantages of using a contactless actuation system for handling thin substrates. Besides these examples, there are many more to be found in literature that stimulate researchers to work on these contactless systems.

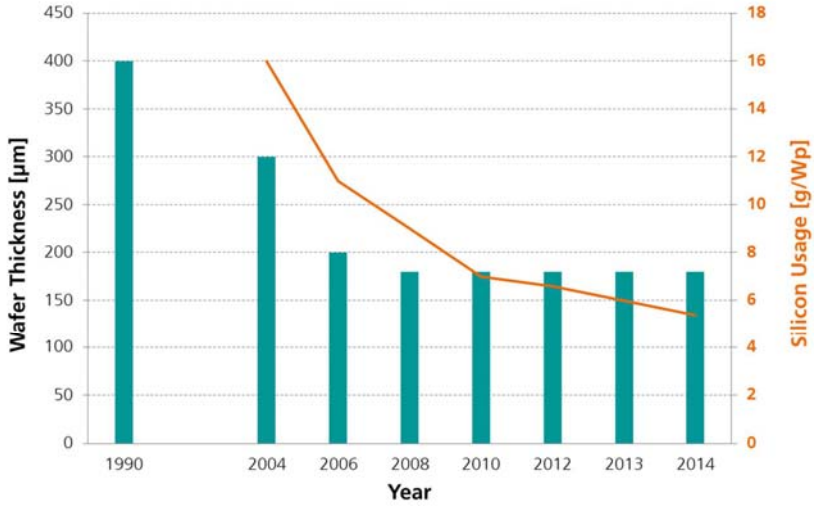


Figure 1.2: Reduction of the silicon substrate thickness used in solar cell industry in the past (source Fraunhofer PSE AG 2015)

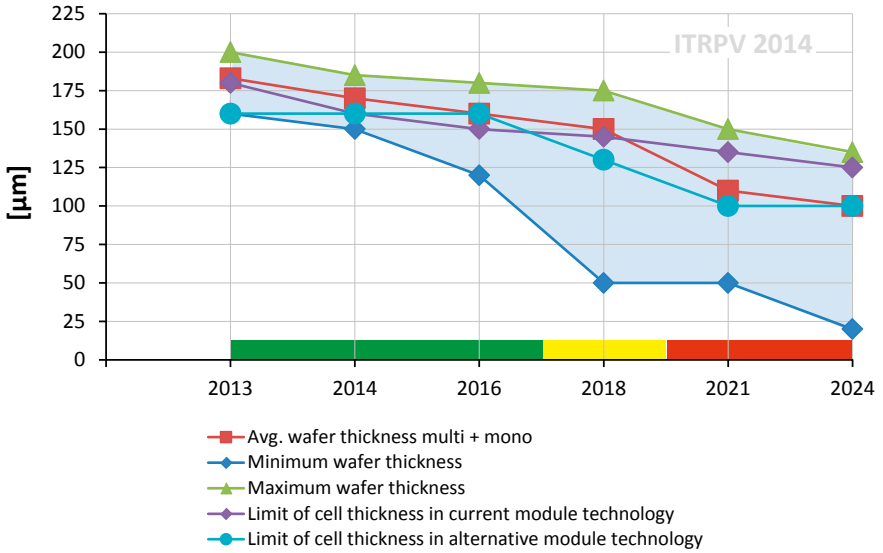


Figure 1.3: Expected trend for the reduction the silicon substrate thickness in future (source [1])

1.2. Different contactless actuation principles

This section presents several different principles that have been described in literature for developing a contactless actuation system. Not intended to present a quantitative comparison, it has been written as an illustration how contactless actuation systems are attractive to researchers. Also, it gives an overview picture of the technologies to one that wants to develop a contactless actuation system for her own application.

Historically, the first demand for having a contactless actuation system is to avoid dry friction between two solid objects. Without dry friction, motion of an object can be controlled more precisely due to the absence of the stick-slip effect. Without contact between solid objects, the wear process is eliminated, resulting in a reduction of maintenance costs, e.g. one of the reasons for the development of Maglev trains. More recently, as presented above, a contactless actuation system is demanded to be used as a handling tool so that the contamination source from mechanical contacts can be eliminated, and the likelihood of breaking thin substrates can be reduced. In another field, microassembly (for instance chemical reaction control), because the size of handled objects is at microscale level, adhesion forces such as electrostatic, van der Waals, surface tension forces become dominant and challenging to deal with. Therefore, using a contactless actuation system is considered to be the most promising alternative for this task.

Typically, a contactless handling system requires forces for two functions: levitation (bearing) and propulsion (motor). The levitation function is required as an action of making the handled object free from gravity, whereas the propulsion function is about controlling object's motion while it is levitated. In literature, the main differences between systems are how the forces are created and for which function they are used. Following, a brief review of different force types used in this field is presented. At the end of this section, Table 1.1 summarises different force combinations that have been used in developing a contactless actuation system.

Electromagnetic force is one of the contactless force types that has a long history of research. Therefore it is not surprising that electromagnetic forces have been used widely in this field of contactless actuation system.

Electromagnetic force is a result of the interaction between electric and magnetic fields. Depending on how these fields are configured, which is highly various, two main types of forces can be generated between two objects: reluctance force and Lorentz force. Reluctance force is an attracting force created on an ferromagnetic object when an electric current is fed to a coil that is wound around a nearby ferromagnetic yoke (Figure 1.4a). It is highly non-linear. Approximately, this force is proportional to the current squared and inversely proportional to the distance squared (defined from the mover to the yoke with the assumption that their surfaces are flat and parallel). In contrast, Lorentz force can be considered to be linear in the operating stroke, and proportional to the controlling element, current. It is created when a current is fed to a coil that is inserted in a magnetic field as shown in Figure 1.4b. For a more detailed understanding on electromagnetic physics and its applications, readers can refer to [45] where the matters in this topic are presented in a nice engineering and systematic way.

The limitation of electromagnetic force is mainly determined by the allowable ther-

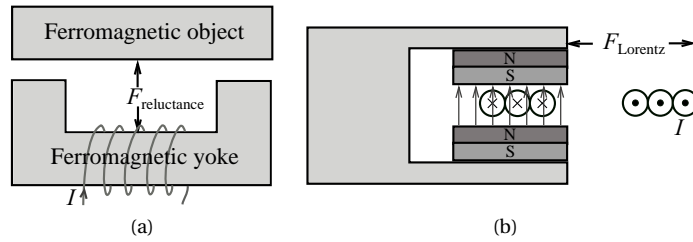


Figure 1.4: Reluctance force (a), Lorentz force (b)

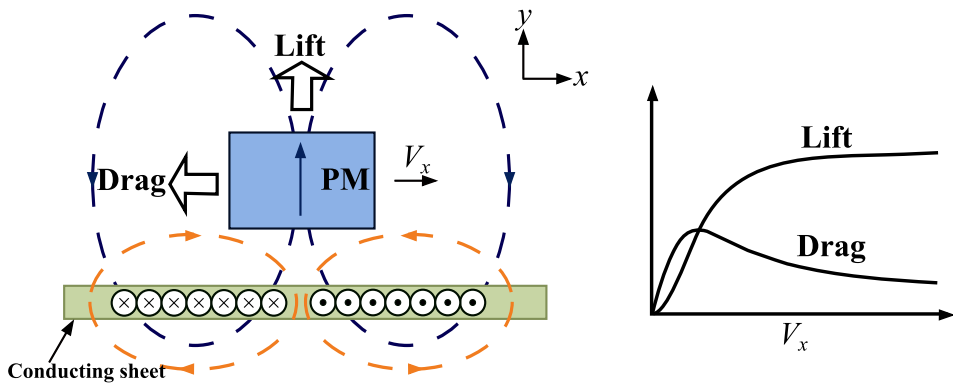


Figure 1.5: The principle of electrodynamic suspension. Repulsive forces are created by the interaction between the two magnetic fields. The first field is from a strong permanent magnet, the second one is from the Eddy current induced by the change of the first field. (source [42])

mal dissipation in the coil, which is usually high. Therefore, the achievable force density (force per unit of mass) of an electromagnetic actuator is very high. This makes both types of electromagnetic forces suitable for either levitation function or propulsion function of a contactless actuation system. However, since the reluctance force operates on a relatively shorter distance and is single-directional, it is more frequently used for levitation, e.g magnetic bearings. In contrast, because of the possibility of controlling the commutation between different coils (see [45] for details), Lorentz force can be generated over a long stroke. Also, because of the linear property, it is more suitable for propulsion function, e.g linear motors.

For some special cases, e.g. high speed motion of a Maglev train, repulsive forces that are caused by the interference between two magnetic fields can be used for levitation as well [42], [19]. Illustrated in Figure 1.5, in this concept, which is called electrodynamic suspension, the first magnetic field is generated by either strong permanent magnets or superconducting magnets that are attached on the mover. The second magnetic field in this figure is from the Eddy currents flowing in a conducting plate placed at the stator, induced by the change of the first magnetic field, which is caused by the movement of the mover. At a sufficiently high speed, the levitation function can be realised stably without any controllers.

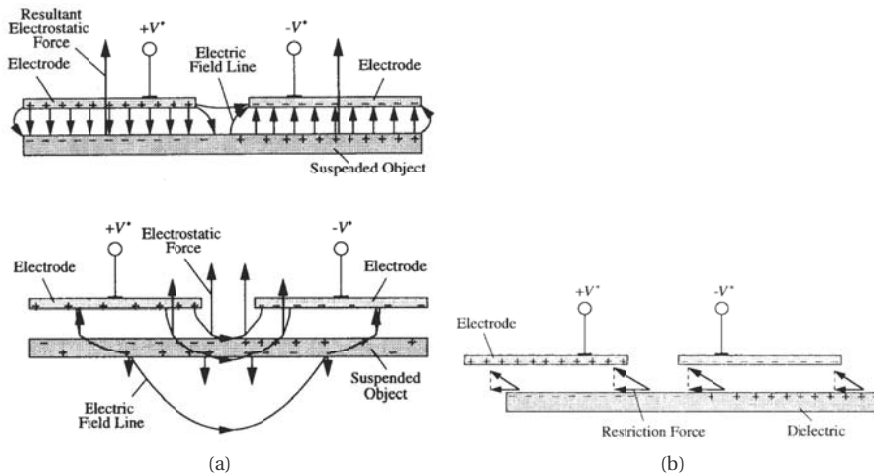


Figure 1.6: Electrostatic forces just after supplying voltages: top figure for conducting materials, bottom figure for dielectrics (a), electrostatic forces used for propulsion function (b) (source [23])

In literature, it can be found that many contactless actuation systems have been developed using electromagnetic forces. Whenever dry friction needs to be eliminated from a controlled motion system, electromagnetic forces could be considered for obtaining the contactless property. However, there is one requirement that makes them not suitable for all applications: functional components need to be attached to the handled object, or, at least, handled objects have to be made of ferromagnetic or electrically conductive materials.

Electrostatic force is another contactless force type that has been used for contactless handling applications. First published by Coulomb in 1784, it has been described as the forces that electric charges exert on each other.

Illustrated in Figure 1.6a, when non-zero opposite voltages are applied at two electrodes, the handled object is electrically polarised such that an attracting force is generated, which is the summation of electrostatic forces induced between the charges in the electrodes and the object. Compared to electromagnetic force, the restriction of the used materials is not that tight for an electrostatic force to be created. However, the electrical resistivity of the object's material plays an important role in the dynamic response of the resultant force [23]. For electrical conducting materials, the polarization is affected instantly by a change of the applied voltages due to the fact that electrons can move freely in conductors. For dielectric materials, which are slightly conducting, it takes a much longer time for the polarization to be steady. Shown in Figure 1.6a, just after the voltages are supplied, the polarization is stronger in the middle area of the object because the path of the electric field here is shorter. Therefore, in order to enhance the dynamic response, in literature, it is frequently observed that the electrodes are divided into smaller sections when the object is made of low conducting materials.

For developing a contactless actuation system, electrostatic forces have been used

for both levitation and propulsion functions. Shown in Figure 1.6b, the levitation function is obtained by the force that is distributed over the overlap area between the object and the electrodes. In contrast, the propulsion force can be created only at the boundary, when the activated electrodes are misaligned with the object. The limitation of electrostatic force is determined by the maximum intensity of the electric field that can be created in an environment such that sparking electric discharges do not occur. For an example, in a typical atmospheric environment, the maximum intensity is about $3 \cdot 10^6 \text{ V m}^{-1}$. The resulting levitating force density is approximately 40 N m^{-2} , which is just sufficient for lifting a 0.7 mm thick substrate. Since the propulsion force is only generated at the edge of the handled object, it can achieve a much lower level, in the order of one hundred of μN (achieved on a 200 mm diameter wafer [25]).

It has been proven that a contactless handling system can be built, fully based on electrostatic forces [24] [25] [58]. The benefit of using only electrostatic forces is that the system is able to be operated in vacuum environment. However, for obtaining a stable levitation function, it requires to have feedback controllers, which are usually complicated to design because of, first, the coupling between two functions that are created by the same set of electrodes, second, the delayed polarization that depends strongly on the substrate material properties and the operating environment, e.g. humidity. Therefore, there are also systems that use electrostatic forces only for propulsion, in combination with another principle such as air cushion for levitation [14], [37].

Ultrasonic vibrations have been used as the sources of forces for contactless handling systems that operate in an environment filled with air or fluid. In literature, two distinct principles can be found: using the squeeze film effect and using standing waves.

The first principle, which is sometimes called near-field acoustic levitation, is more based on fluid dynamic effects than acoustic effects. First presented with theory and experiments in 1964 by Salbu [44], the so-called squeeze bearing was able to levitate objects with a vibration source. Figure 1.7 can be used as an explanation of this principle. When the gap between the object and the levitating system is oscillated with a sufficiently high frequency, the gas in this gap can be considered to be trapped, having no time to escape. The relation between the pressure and the volume of this trapped amount of gas can be described as a curve of an isothermal gas. Because of the difference in pressure between the compression and decompression, the resulting average pressure is higher than ambient, thus the levitating force is created as an integration of this pressure. Since this effect is originated from the compressibility of the film medium, this principle works only with gas.

For contactless handling applications, this type of force is mainly used for the levitation function. Being comparable to conventional air bearings, the achievable levitating force from this principle is very high, more than sufficient for lifting thin substrates. For the propulsion function, for transport applications, it is usually obtained by controlling the vibration source to travel along a conveyor [18], [51], [41], [21], [59]. With this method, a propulsion force density can be achieved in the order of $0.3 - 0.5 \text{ N m}^{-2}$ [18], [59]. For applications where the objects are required to be kept in place, propulsion function need to be created by another principle such as using vacuum nozzles for small objects (small force) [40], or using tactile shoulders for large objects (not fully contact-

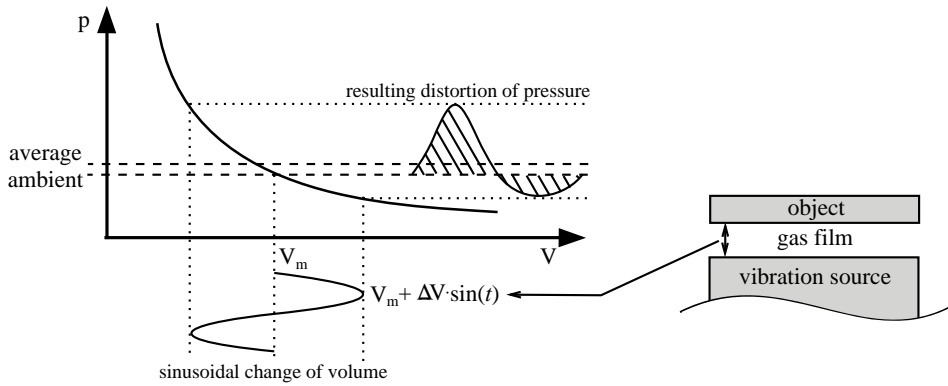


Figure 1.7: The principle of squeeze film levitation. Because of the difference in pressure between the compression and decompression, the resulting average pressure is higher than ambient (source [40])

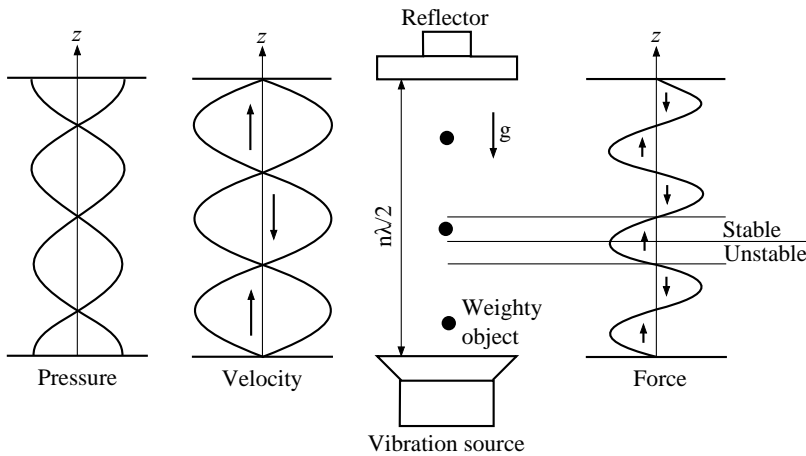


Figure 1.8: Levitation using acoustic standing wave principle. Small objects can be trapped slightly under the pressure nodes (source [54])

less) [39].

In contrast, the second principle of employing an ultrasonic vibration source can be applied in both air and fluid environment due to the fact that it is based on sound standing waves. The first experiment illustrating this principle has been presented in [57]. This principle can be explained by Figure 1.8. Using a sound source in combination with a reflector, that is ideally placed with a distance of a multiple of half wavelength, standing waves can be created. Shown in this figure, on the centre axis, the pressure of the fluid presence with nodes and anti-nodes. Because of this, a small object can be levitated in a region that is slightly under every pressure node. Furthermore, because the axial velocity of the fluid is highest at the pressure nodes and radially reduces toward outside, a slight vacuum pressure is created with Bernoulli effect that pulls the object into the centre axis. As a result, the object is trapped by a sound standing wave.

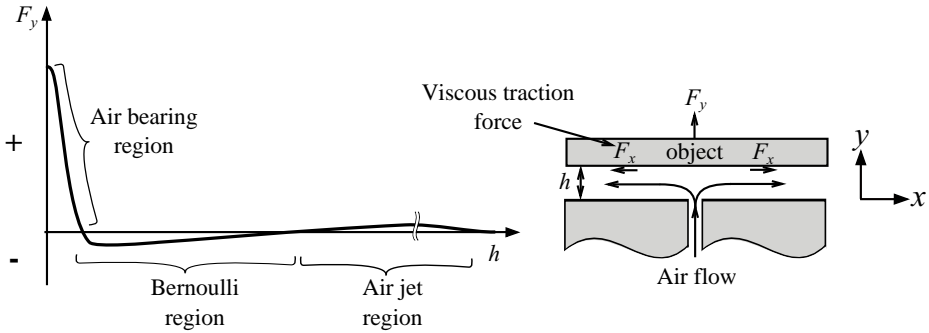


Figure 1.9: Four types of forces can be generated with an air flow. Mainly depending on the thickness of the gap h , the normal force can be created as the result of one of three different phenomena. The fourth type of force is the viscous traction force of the air flow inside the gap, acting tangentially. (adapted from [16])

Until now, this principle is applicable for small objects that have a weight in the order of a few grams. The Bernoulli vacuum created in this configuration is very limited, resulting in small lateral forces. In order to move the object in three spacial degrees of freedom, researchers usually arrange the actuator pairs in different directions such that the object is trapped by different standing waves at the same time [35], [15], [36]. More recently, using just one array of acoustic sources, a holographic field of sound has been generated, successfully in manipulating an object by actuation forces created on one side [33].

Air flow is the final force source presented in this section that has been used for contactless handling applications. With an air flow depicted in Figure 1.9, four types of forces can be created on this object: three in normal direction and one in tangential direction.

Depending on the operating conditions, especially the thickness of the air gap, the force in normal direction can be created as the result of one of three different phenomena. Firstly, when the air film thickness is sufficiently small such that the flow in the film is laminar, the pressure distributes over the full overlap area between the object and the system, resulting in a levitating force which is equal to the integral over the surface of this pressure. This is the principle that is used in conventional air bearings. The achievable force is therefore very high. However, in contactless applications, this type of forces has been used for levitation function only.

Secondly, with a larger film thickness, when the velocity of the air flow is sufficiently high, the Bernoulli effect can result in an attracting force that is able to lift an object from the top side (in this figure this force directs downward). In literature, this force type is usually for the levitation function. In addition, as demonstrated in [26], the Bernoulli effect created by strong air jets can be used as a source that generates potential flow fields for the propulsion function.

Thirdly, when the film thickness further increases, a repulsion force is again created on the object, caused by an (inertia) impact of the air jet. In the field of developing a contactless actuation system, this type of forces has been used widely for both levitation

and propulsion functions. Shown in [26], [30], potential flow fields are created and controlled such that their impact can be used to move an object while it is levitated on an air bearing like table. Using this concept, the propulsion force depends strongly on the object's shape, as well as its thickness. Reported in [26], the highest force of $20.8 \cdot 10^{-3}$ N has been achieved on a H-shaped object that has 9 mm thickness with planar dimensions of 39×33 mm². However, the propulsion force reduces to about $1 \cdot 10^{-3}$ N, when handling a thinner (0.7 mm) object that has similar planar dimensions.

For handling thin objects, the concept of tilted air jets has been used more often. With inertia forces created by tilted air jets, both levitation and propulsion function can be produced. This design has been used for many different sizes, from small objects [12], [50], [20], [60] to large objects [6], [9]. With this principle, the achievable propulsion force is in the order of 25 N for a flow rate of one cubic metre per second [9].

The fourth type of force that can be generated by an air flow is viscous traction force, acting tangentially (Figure 1.9). This type of force has been used to drive the spindle of some high-speed rotary systems for micro machining applications [8], [10]. For positioning applications, viscous traction force of an air flow has been also used for the propulsion function successfully [52],[56]. This thesis presents a further study on using viscous traction force for the applications of positioning thin substrate. Presented later in Chapter 3, an experiment shows that the propulsion force can be achieved in the order of 350 N for a flow rate of one cubic metre per second.

Summarised in Table 1.1 , in order to provide the reader with an overview of this contactless actuation topic, different principles found in literature are presented as the combinations of the force types used for levitation and propulsion functions.

		Propulsion function						
		Electro-magnetic	Electrostatic	Ultrasonic-travelling wave	Ultrasonic-Standing wave	Air Bernoulli	Air jet (inertia)	Air viscous
Bearing function	Electro-magnetic	[27], [45] ⁽¹⁾	-	-	-	-	-	-
	Electrostatic	-	[24],[25]	-	-	-	-	-
	Ultrasonic-Squeeze film	-	-	[41],[18]	-	-	-	-
	Ultrasonic-Standing wave	-	-	-	[57],[33]	-	-	-
	Air bearing	[45] ⁽¹⁾	[14],[37]	-	-	[26] ⁽²⁾	[26] ⁽²⁾ , [30]	[56],[53],[8],[10]
	Air Bernoulli	-	-	-	-	-	[40]	-
	Air jet (inertia)	-	-	-	-	-	[12],[9],[6]	-

Table 1.1: Summary of contactless principles have been researched in literature

⁽¹⁾ The number of publications in these boxes does not reflect the applicability of the principles. The references have been chosen because they are representative for that particular concept.

⁽²⁾ The propulsion function of this principle is originated from the Bernoulli effect, that is used to generate an air flow field. The actual propulsion function is from the air flow inertia force for thick objects, and viscous force for thin objects.

1.3. Research objective

The research presented in this thesis focuses on the principle of using the viscous traction force of a thin film flow to actuate a thin substrate, while it is levitated by the bearing force created by the same thin air film. Stimulated by the promising results of using this principle for positioning applications [56], the goal of this research is determined to be **"Exploring the principle by investigating different potential concepts, studying the achievable performance regarding two main aspects: the ratio of force to flow rate, and the dynamic response of the force"**.

The exploration is determined to be, firstly, classifying embodiment variants of the principle. Secondly, performance metrics need to be proposed for the assessment of different embodiments. Thirdly, predictive models are required to be developed so that the performance limits of different embodiment variants can be determined, thus a fair comparison can be achieved. Fourthly, in order to validate the models, experiments are necessary to be performed, both on static and dynamic aspects. Finally, based on the developed models, design charts can be set up for such a contactless actuation system.

1.4. About this thesis

The exploration is presented in this thesis with the following structure. After the first chapter where the motivation is addressed and a study on different principles is presented, with the knowledge gained by studying the former work, the principle exploration can be started and is presented in Chapter 2. Firstly, it introduces different concepts that can be used to control the propulsion forces. Secondly, a geometric optimisation for the ratio of force to flow rate is obtained based on an analytical model. Finally, different concepts are compared, taking the optimum performance of each one. Also in this chapter, a promising concept has been chosen for further research, deforming the bearing surface by the tilt motion of small sections.

Chapter 3 presents the experimental results verifying the predictive model, confirming the validation of the optimisation. Also, because it is necessary to have a more detailed and comprehensive model in order to predict more accurately the system's behaviour, the development of a numerical model is described in this chapter.

While the main studying objects in Chapter 2 and 3 are single DoF actuators, Chapter 4 explores the actuator designs that can be used to develop a planar DoF system. It analyses the influence of the design properties such as actuator shape, and the inlet/outlet area on the system performance. Then, the design guideline for such a contactless actuation system can be developed.

In chapter 5, focus shifts from the static performance to the dynamic behaviour. The possibility of improving the dynamic response is one of the reasons for the concept of tilting bearing surfaces to be chosen for further research. This will be interpreted in Chapter 5. First, it describes the mechanical structure of an experimental setup, which is named 'Flowerbed'. Then, the design decisions are made, based on the results of both static and dynamic prediction. Finally, Flowerbed is realised and its overall dynamic behaviour is predicted, including pneumatic and mechanical aspects.

In line with the story, Chapter 6 presents experimental results of the measured dy-

1

dynamic behaviour of Flowerbed.

Closing this thesis, Chapter 7 summarises the most important results obtained in this work. And as usual, there are still remaining challenges and questions for future research on this topic. These are also addressed in this final chapter.

2

CONCEPT EXPLORATION AND COMPARISON

In this chapter, first, the principle of using viscous force of a thin air film flow to actuate a thin substrate is briefly reinterpreted. Then, some new possibilities for controlling this force are introduced. The performance of these concepts will be analysed and optimised based on the relation between the generated force and the consumed flow. Finally a comparison between some of these concepts will be presented.

2.1. Actuation using an air film

As introduced briefly earlier, the actuation principle that is focused in this thesis is to use the viscous traction force of an air film flow to actuate a thin substrate. In air bearing applications, viscous force is not beneficial since it represents friction loss. However, if the bearing surface is modified deliberately, this force can be increased and controlled, in order to be used for the propulsion function of a contactless actuation system [52]. Shown in Figure 2.1, one way to modify the surface to obtain the motor function is to partly recess the surface with a pocket in the order of several tens of μm . The inlet and outlet grooves are located inside this recess, at two opposite sides. Each recess with the surrounding dam can be identified as one actuator cell. A demonstrator based on a modification of this concept has been built successfully in the research of Wesselingh [56]. Although in [56] the inlets and outlets were arranged somewhat differently, the basic principles were still similar, thus could be explained using Figure 2.1.

In [56], typically, the actuator cell was square in shape and had a size of $10\text{ mm} \times 10\text{ mm}$. The size of the recess was chosen to be $8\text{ mm} \times 8\text{ mm}$, resulting in a dam width of 2 mm . The recess depth was chosen to be $20\ \mu\text{m}$. With this actuator geometry, and a pair of inlet/outlet grooves located on opposite edges, a force is generated on the substrate when a pressure difference ($p^+ - p^-$) is applied between the inlet and outlet. Analysing one cell, the force density (force per unit area) is characterised as:

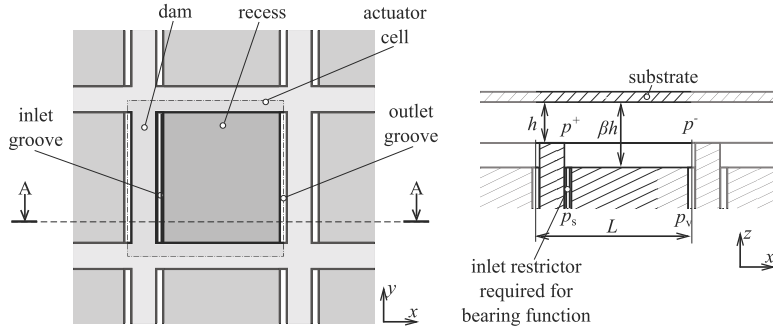


Figure 2.1: By modifying the bearing surface, the viscous traction of a thin film flow can be used to actuate a substrate. The force created by each actuator cell is proportional to the pressure difference ($p^+ - p^-$) and the depth of the recess $(\beta - 1)h$.

$$\bar{F} = \frac{1}{L} \frac{(\beta - 1)h}{2} (p^+ - p^-) \quad (2.1)$$

in which $(\beta - 1)h$ is the depth of the recess. And in [56], the force was controlled by varying the pressure difference using proportional valves.

Next to the propulsion function, the bearing function can also be produced by the same air film. This bearing function is defined as a combination of two properties: the bearing load capacity and the bearing stiffness. The load capacity is resulted as an integral of the pressure over the bearing area. It represents the capability of carrying the object's weight. For the applications of handling thin objects, the required load capacity is usually small, in the order of tens of Pa, thus it can be achieved easily.

The second property of the bearing function, the bearing stiffness, is required in order to keep the fly height stable. Additionally, this distributed stiffness is also used to prevent mechanical contact, even if the substrate is not initially flat. Similar to a conventional air bearing, a positive bearing stiffness can be realised by placing an additional flow restrictor at the inlet so that the inlet restriction is higher than the outlet restriction. Because of this asymmetric design, an actuator cell shown in Figure 2.1 can generate force in just one direction.

In order to develop a multi DoF actuation system, two alternatives was considered in [56]. The first one was to use multi-directional cells in which the flow can be controlled by a multi-port (proportional) valve. Using this method, however, resulted in a challenge: the bearing stiffness was more difficult to be ensured. The restriction of an air port must be increased whenever it is used as an inlet and reduced when it is an outlet. Furthermore, at the crossover moment while switching the flow direction, the flow is zero, the bearing stiffness therefore becomes zero. The second alternative was to construct a multi DoF system based on clusters of single DoF actuators. Each cluster consisted of three or four actuator cells that were arranged in such a way that each cell could generate force in a different direction. Compared to the first option, this method was simpler, therefore was selected in the research of Wesselingh. The main disadvantage of this method was that only a part of the area could be used to create force for each direction.

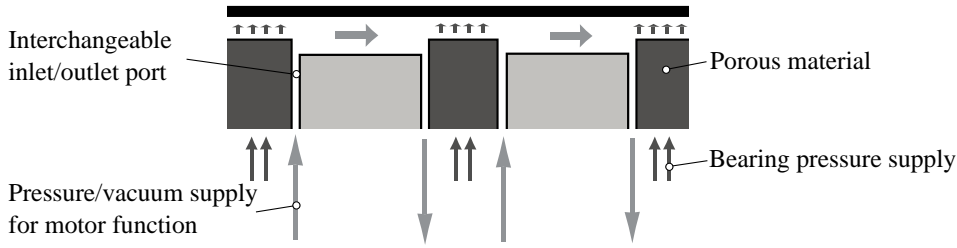


Figure 2.2: The concept of using porous media to generate bearing function separately

A study on the previous research has been performed and presented in Appendix A. Starting from the knowledge gained in this previous study [56] a concept exploration for this actuation principle will follow.

2.2. Different concepts

From Equation 2.1, it can be observed that the traction force created by an actuator cell is proportional to the depth of its recess and the difference between the pressure at the inlet and outlet. In other words, the force can be controlled by varying either the supply pressure or the recess depth. A combination of pressure control and geometry control can be used as well. However, to make a clear comparison, the concept exploration of this contactless actuation principle will be divided into two main groups: pressure variation concepts and deformable surface concepts.

2.2.1. Pressure variation concept

This group of concept uses valves to control the inlet/outlet pressure in order to generate the required force on the substrate. The bearing surface is fixed as designed. The concept implemented in the demonstrators of the previous research belongs to this group. Learned from [56], there are two main disadvantages affecting this concept. Firstly, for a multi DoF system, at any moment the effective force is created only by a quarter of the active area. The other three quarters produce balanced forces and mainly contribute to the bearing function. The second disadvantage is the complex air supply manifold that is required for the connection between the actuator inlet/outlet points and the external controlling valves. This pipe network is the main contributor to the pressure dynamics. With a length of approximately 120 mm for each channel in the manifold of the last demonstrator of [56], the resulting frequency response implies a bandwidth limitation of the pressure controller at around 120 Hz (see Appendix A). For a bigger manifold, which must be used for a system that handles larger substrates, this bandwidth might be lower because of the longer channels that result in the higher order dynamic behaviour of the air flow to occur at lower frequencies.

For a multi DoF actuation system, compared to the method of using clusters of actuators in [56], the surface area can be used more efficiently. One of the alternatives is to separate the bearing function and the motor function. In the application of handling

thin substrates, the required bearing load capacity is quite low. Furthermore, from the analysis in the previous research, the resulting bearing stiffness is very high, more than sufficient. Using a smaller area to produce the bearing function is therefore more effective. For instance, the bearing function can be concentrated at the dam area instead of distributed on the full surface of the actuators. As shown in Figure 2.2, one of the possible solutions is to employ porous media in constructing the dam as a separate bearing entity with its own pressure supply. Because the substrate is already levitated at a stable fly height by this bearing system, the restriction at the inlet and outlet points can be designed to have an equally low value. The inlet and outlet points are therefore interchangeable so that one actuator cell can generate force in various directions. More importantly, with a separated bearing entity providing positive stiffness continuously, actuator cells can change the force direction without care of stiffness loss while switching the flow direction. Additionally, when no traction force is required, the traction air flow across the pocket can be turned off, thus the air flow can be used more efficiently.

A preliminary analysis of different configurations using this concept shows promising results for the static behaviour. However from the dynamics point of view, if external valves are still used in combination with a manifold, the controller bandwidth is not improved. In order to enhance the control bandwidth, further research and development are required. For instance, small and fast proportional valves need to be developed so that they can be integrated closely to the actuator surface, in order to eliminate the limitation caused by the air flow dynamics in the manifold.

2.2.2. Deformable surface concept

In contrast to the pressure variation concept, the deformable surface concept varies the traction force by deforming the bearing surface while keeping the supply pressure constant. As an example, Figure 2.3 illustrates how a force can be controlled in one DoF by a deformable surface. The bearing surface is created with two groups of elements that are able to move up or down in a range of tens of μm . The inlet and outlet supply pressure are kept at a constant level. In the neutral operating point ($F = 0$), these two groups are controlled to have the same height. When a force is required, for instance towards the right hand side direction, the elements located at the right side of the inlets move down simultaneously, resulting in an increase of the viscous traction force generated by the flow across these elements. As a result, the total net force will be non-zero and directed towards the expected orientation. With this method, the force can be controlled without any external (proportional) valves. This concept does not suffer the limitation caused by the pressure dynamics of the manifold because the force controlling components are designed at the same position where the force is actually generated.

Moving a part of the bearing surface up and down is not the only feasible concept. In fact, this up-and-down concept is suitable only for a single DoF application. Organizing the up/down elements including the inlet and outlet ports for a full planar DoF actuation system is a challenge. Instead, the bearing surface can be deformed differently in order to achieve a similar effect. Figure 2.4 illustrates an actuation surface consisting of bendable elements, for instance actuated by bending piezo. The bending motion can be used to control the traction force while the pressure source and sink are kept at a constant

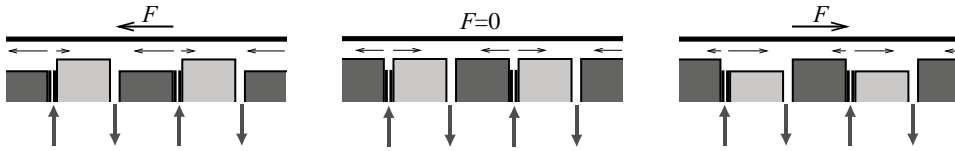


Figure 2.3: Deformable surface concept-Up/down configuration

level. However constructing a deformable surface with bendable wings is complicated and expensive.

Another configuration, the "flowerbed" concept, is therefore introduced as shown in Figure 2.5. Each actuator cell (hexagonal shape) has one inlet point positioned at its centre. The air is supplied from the base through a flexible stem, and returned at the edges of the cell through a vacuum chamber. These stems are mechanically connected together by an intermediate plate. Any in-plane movement of this plate relative to the base will uniformly tilt all the actuator surfaces. Thus the traction force can be controlled by the position of this intermediate plate.

The performance of this tilting configuration can be further improved with a modification of the inlet. In order to increase the efficiency of the actuator area, porous media can be used to (virtually) move the inlet. Shown in Figure 2.6, instead of one central inlet point, the whole actuator surface serves as the inlet by means of porous media. The air is provided through the supplying gap underneath the actuator surface. During the tilting motion, the thickness of this gap changes resulting in a movement of the virtual inlet point. For instance, when the actuator tilts to the right hand side direction, the thickness of the the left part of the supplying gap increases, resulting an increase of the air flow coming from the left part of the porous media to the bearing gap. In this situation, the shift to the left side of the virtual inlet point will help in reducing the flow while generating the same force compared to the simple tilting configuration. The benefit of shifting the inlet point is illustrated in the analysis presented in the next section.

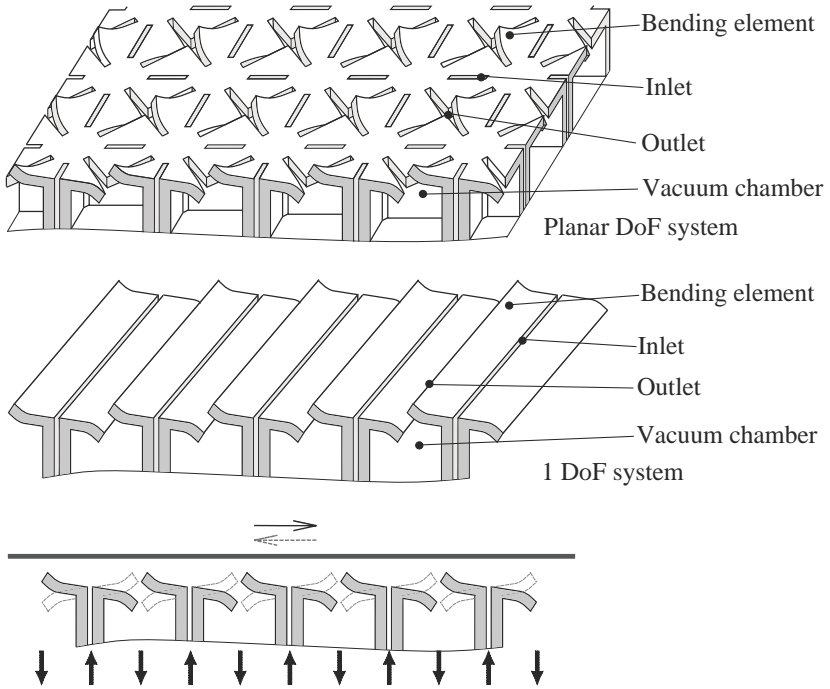


Figure 2.4: Deformable surface concept-Bending configuration

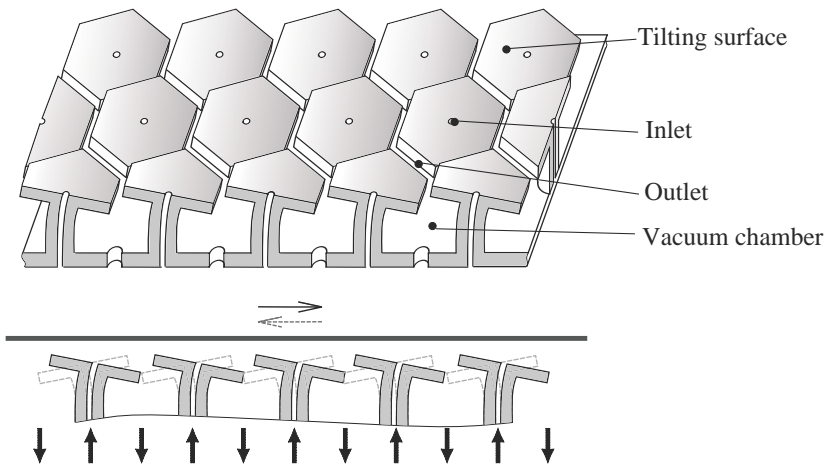


Figure 2.5: Deformable surface concept-(Simple) tilting configuration

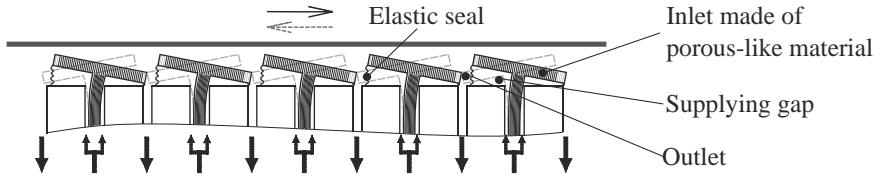


Figure 2.6: Modified tilting configuration can be used for further improvement from the simple tilting concept. In this configuration, the supplying gaps help in virtually moving the inlet points in the bearing gap. For instance, when the actuators tilt to the right hand side direction, the thickness of the the left part of the supplying gaps increases, resulting an increase of the air flow coming from the left part of the porous media to the bearing gap. This results in a shift to the left side of the virtual inlet point, that will reduce the flow while generating the same force compared to the simple tilting configuration.

2.3. Optimal design

This contactless actuation principle has been invented with the purpose of preventing contamination that might be created by any mechanical contact. The air used in this type of systems therefore must be clean. Because clean air is costly, the static performance of an actuation system is evaluated based on the ratio of the force density to the flow density. The force density and the flow density are defined as the force and the flow per unit area of the array of actuators. In other words, after normalising to the surface area, the system that gives higher force for the same flow rate will be judged to be more efficient.

In this section, the static performance of these concepts is analysed, mainly based on the motor function. A full comparison of different concepts including the bearing performance will be presented in the next section. Because the main interest is the static performance, it will not be discussed in this section how the force is controlled (pressure variation or deformable surface). The analysis is presented in two different groups of the bearing surfaces: the step like surfaces and the tilting surfaces. For each study, both the incompressible flow model and the compressible flow model are used.

In order to compare different concepts, it is sufficient to start with single DoF actuators. Therefore, the actuators in this analysis are assumed to have an infinite width (the dimension in y -axis in all the figures). Besides, the inlet and outlet ports are assumed to be infinitely small so that the flow path length will be equal to the actuator length (the dimension in x -axis). The outlet restriction R_o is assumed to be zero, resulting in an outlet pressure (in the air film) p^- identical to the vacuum supply pressure p_v . This assumption is made because in practice the outlet restriction is desired to be as small as possible in order to minimise the pressure drop over this restrictor so that the vacuum source can be used efficiently.

The mathematical model has been developed based on the thin film lubrication assumptions. It is valid when the flow can be assumed to be laminar and "zero-slip" boundary conditions are applied. The pressure is assumed to be constant with respect to the film height. The pressure distribution p can be described using the Reynolds' equation for a thin film [11]. For single Dof, we have:

$$\frac{\partial}{\partial x} \left(-\frac{\rho H^3}{12\eta} \frac{\partial p}{\partial x} + U \frac{\rho H}{2} \right) = 0 \quad (2.2)$$

in which the pressure distribution p is a function of x that needs to be solved. H is also a function of x and expresses the film thickness. U is the in-plane velocity of the substrate relative to the actuation system. η is the dynamic viscosity of air, and ρ is the air mass density.

In the application area for this principle, contactless thin substrate handling and positioning, the substrate speed is small compared to the speed of the air flow. Presented in Chapter 3, an example of the air flow velocity is in the order of tens of meter per second, much higher than the required substrate's velocity of a typical positioning application. Therefore it is acceptable to assume that the substrate is stationary (zero speed relative to the handling system).

Again, since the carried object is just a thin substrate, the required load capacity of this bearing system can be assumed to be exactly zero:

$$w = \int (p - p_a) dA = 0 \quad (2.3)$$

in which p is the pressure distribution in the air film, p_a is ambient pressure. It should be noted that the zero load capacity assumption has been made in order to represent that the substrate is levitated with zero acceleration in normal direction. For a thicker (heavier) substrate, this assumption can still be made with an offset of p_a .

With the assumptions that have been made, the motor function of a contactless actuator can be analysed with the pressure distribution obtained by solving:

$$\frac{\partial}{\partial x} \left(-\frac{H^3}{12\eta} \frac{p}{R_g T} \frac{\partial p}{\partial x} \right) = 0 \quad (2.4)$$

in which the air density has been described as $\frac{p}{R_g T}$. The air is assumed to be an ideal gas, and the air film is considered to be isothermal so that the air density is proportional to the pressure p .

The boundary conditions used to solve Equation 2.4 are the zero load capacity constraint and the assigned outlet pressure (p^-). With the obtained pressure distribution, the force density can be derived:

$$\bar{F} = \frac{1}{L} \int_0^L -\frac{H}{2} \frac{\partial p}{\partial x} dx \quad (2.5)$$

Also from the obtained pressure distribution, the flow density can also be derived. For convenience, it is chosen to be calculated at the inlet, as the sum of the flows through the left and the right domains:

$$\bar{m} = \frac{1}{12\eta L} \frac{p^+}{R_g T} \left(H^3 \frac{\partial p}{\partial x} \Big|_{x^+} - H^3 \frac{\partial p}{\partial x} \Big|_{x^-} \right) \quad (2.6)$$

in which x_{inlet} is the location of the inlet.

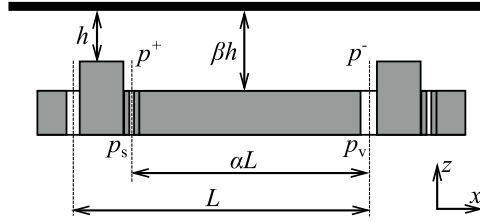


Figure 2.7: Actuator geometry used for the analysis

2.3.1. Step surface analysis

An actuator that has an infinite width and a cross-section as shown in Figure 2.7 is investigated. The length of the actuator and its recess are L and αL respectively, $0 < \alpha < 1$. The fly height h is defined as the distance from the highest point of the system (the dam) to the substrate. β describes the ratio of the film thickness in the recess domain to the fly height, $\beta \geq 1$. For the step surface actuator, the film thickness function H in Equation 2.4 is a constant. $H = h$ for the left domain of the inlet (dam) and $H = \beta h$ for the right domain (pocket).

Incompressible flow model When the pressure difference in the system is relatively small compared to ambient pressure, the air can be assumed to be incompressible. In other words, this assumption is valid only in the operating condition that the vacuum supply pressure p_v is closed to ambient pressure p_a . With this assumption, the air density is constant, Equation 2.4 becomes:

$$\frac{\partial^2 p}{\partial x^2} = 0 \quad (2.7)$$

The pressure distribution p in the air film is a linear decrease from the inlet pressure p^+ to the outlet pressure p^- (Figure 2.10). The load capacity per unit area can be derived:

$$\bar{w} = \frac{1}{L} \int_0^L (p - p_a) dx = \frac{p^+ + p^-}{2} - p_a \quad (2.8)$$

Note that all the pressure symbols express absolute pressure values.

From the zero load capacity assumption, the inlet pressure p^+ can be calculated:

$$p^+ = 2p_a - p^- \quad (2.9)$$

The outlet restriction has been assumed to be zero, thus p^- can be substituted by p_v . Then, the force density and the mass flow density can be obtained:

$$\bar{F} = \frac{1}{L} \frac{(\beta - 1)h}{2} (p^+ - p^-) = \frac{(\beta - 1)h(p_a - p_v)}{L} \quad (2.10)$$

$$\bar{m} = \frac{p_a}{R_g T} \frac{h^3}{6\eta L^2} \left(\frac{1}{1 - \alpha} + \frac{\beta^3}{\alpha} \right) (p_a - p_v) \quad (2.11)$$

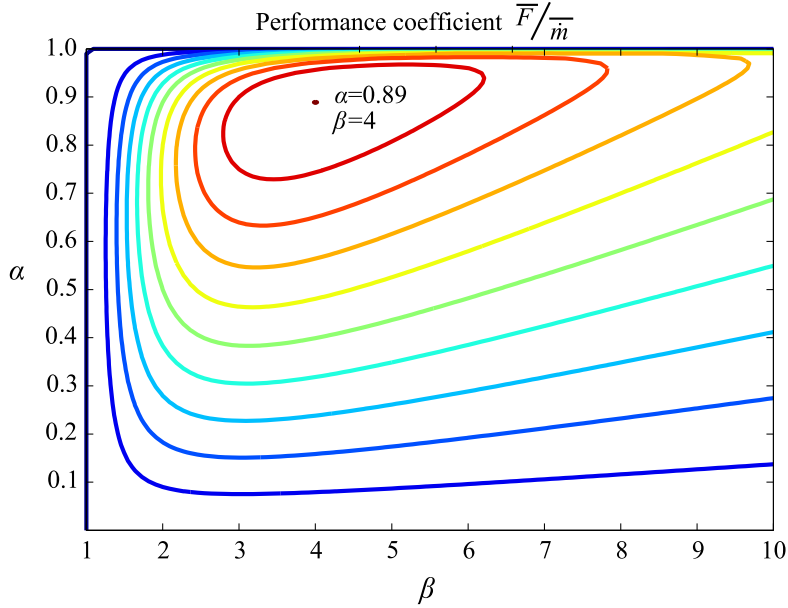


Figure 2.8: The efficiency graph obtained with the incompressible model. The efficiency is maximal at $\alpha = 0.89$ and $\beta = 4$

For a desired force density \bar{F}^* , the required actuator length L^* needs to be:

$$L^* = \frac{(\beta - 1)h}{\bar{F}^*} (p_a - p_v) \quad (2.12)$$

Substitute this L^* into Equation 2.11, the mass flow density is required to be:

$$\bar{m}^* = \frac{p_a}{R_g T} \frac{h \bar{F}^{*2}}{6\eta(p_a - p_v)} \frac{\left(\frac{1}{1-\alpha} + \frac{\beta^3}{\alpha}\right)}{(\beta - 1)^2} \quad (2.13)$$

With a desired design fly height h and a defined vacuum pressure p_v , for any values of the desired force density \bar{F}^* , the required flow density is minimal when the last term of Equation 2.13 is minimized. This occurs when $\alpha = 8/9$ and $\beta = 4$. Figure 2.8 shows the efficiency of the system for various α and β . This graph can be used to identify the optimum geometry parameter for different cases. For instance, in the symmetric up/down deformable surface concept ($\alpha = 0.5$), the recess depth should be designed to have a value of 2.2 times of the designed fly height ($\beta = 3.2$).

Substitute the optimal parameters $\alpha = 8/9$ and $\beta = 4$ into Equation 2.10 and 2.11, the force and flow density will be:

$$\bar{F} = \frac{3h}{L} (p_a - p_v) \quad (2.14)$$

$$\bar{m} = \frac{p_a}{R_g T} \frac{h^3}{\eta L^2} \frac{9}{2} (p_a - p_v) \quad (2.15)$$

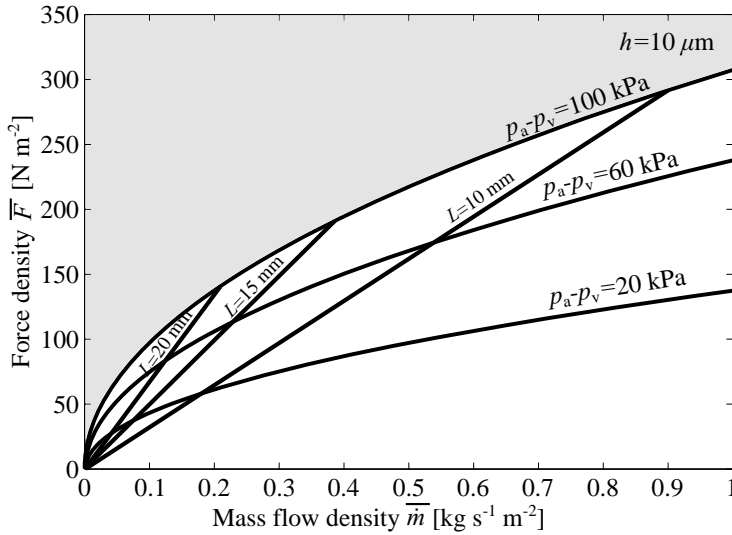


Figure 2.9: The limit performance curve of the optimum geometry of a step surface actuator (incompressible model). For a given actuator length L , when the relative vacuum supply pressure ($p_a - p_v$) increases, the force and flow density will increase linearly following a straight line. Assuming that ambient pressure is 100 kPa, the relative vacuum pressure is limited to 100 kPa due to the fact that the vacuum source is naturally limited to 0 Pa absolute. Therefore, the straight line stops at a point on the curve that is called the limit performance curve.

Limit performance graphs can be obtained for different fly heights using these formulas. Shown in Figure 2.9 is the graph for a fly height of $10 \mu\text{m}$. If the actuator length L is designed to have a fixed value, which is true in practice, and when the vacuum supply pressure is equal to ambient pressure, both the force and flow density are zero. When the relative vacuum supply pressure ($p_a - p_v$) increases, the force and flow density will increase linearly following a straight line. Assuming that ambient pressure is equal to 100 kPa, the relative vacuum pressure is limited to 100 kPa due to the fact that the vacuum source is naturally limited to 0 Pa absolute. Therefore, the straight line stops at a point on the curve that is called the limit performance curve. Indeed, for a fly height of $10 \mu\text{m}$, it is not possible to design a system that will result in a combination of the force density and the flow density inside the shaded area of this graph. This limit performance curve has been obtained by calculating the force density and flow density with the equations 2.14 and 2.15 while varying the length L . It will be lower if the relative vacuum pressure supply is limited to a smaller value.

Apart from presenting the limitation for different working conditions, this graph also helps to design a contactless actuation system. For instance, if a vacuum source is specified with a limit vacuum pressure and the flow rate at that operating point, the graph can be used to determine the length of the actuator that will generate the highest force density.

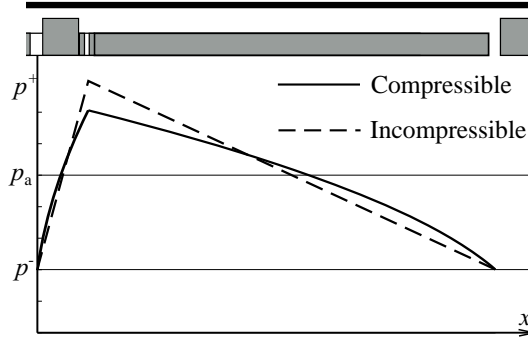


Figure 2.10: The pressure distribution difference between the incompressible model and the compressible model (zero load capacity)

Compressible flow model For high values of $(p_a - p_v)$, i.e. 100 kPa, the curves in Figure 2.9 are not correct because the incompressible assumption is no longer valid. It is necessary to use the compressible flow model for the analysis. The air density term in the Reynolds' equation cannot be treated as a constant any more. For compressible media, leaving out all the constant terms, Equation 2.4 becomes:

$$\frac{\partial}{\partial x} \left(-\frac{p \partial p}{\partial x} \right) = 0 \quad (2.16)$$

Applying the boundary conditions $p = p^+$ and $p = p^-$ at the inlet and outlet respectively, the pressure distribution p can be solved. Not a linear drop of the pressure p from the inlet to the outlet, the result of Equation 2.16 is a linear drop of p^2 . The load capacity per unit area can be derived:

$$\bar{w} = \frac{2}{3} \frac{(p^{+2} + p^+ p^- + p^{-2})}{p^+ + p^-} - p_a \quad (2.17)$$

Figure 2.10 illustrates a result of the pressure distribution p . In this Figure, the inlet pressure p^+ has been calculated from the zero load capacity constraint regarding to the supply vacuum pressure p_v (p^- is substituted by p_v):

$$p^+ = -\frac{1}{2} p_v + \frac{3}{4} p_a + \frac{1}{4} \sqrt{-12 p_v^2 + 12 p_a p_v + 9 p_a^2} \quad (2.18)$$

Because of the non-linearity of the pressure distribution, the resulting inlet pressure p^+ is smaller compared to the one obtained with the incompressible model. This results in a reduction of both the force density and flow density. They can be calculated:

$$\bar{F} = \frac{1}{L} \frac{(\beta - 1)h}{2} (p^+ - p_v) \quad (2.19)$$

$$\bar{m} = \frac{(p^+ + p_v)}{2 R_g T} \frac{h^3}{12 \eta L^2} \left(\frac{1}{1 - \alpha} + \frac{\beta^3}{\alpha} \right) (p^+ - p_v) \quad (2.20)$$

in which p^+ is obtained from Equation 2.18.

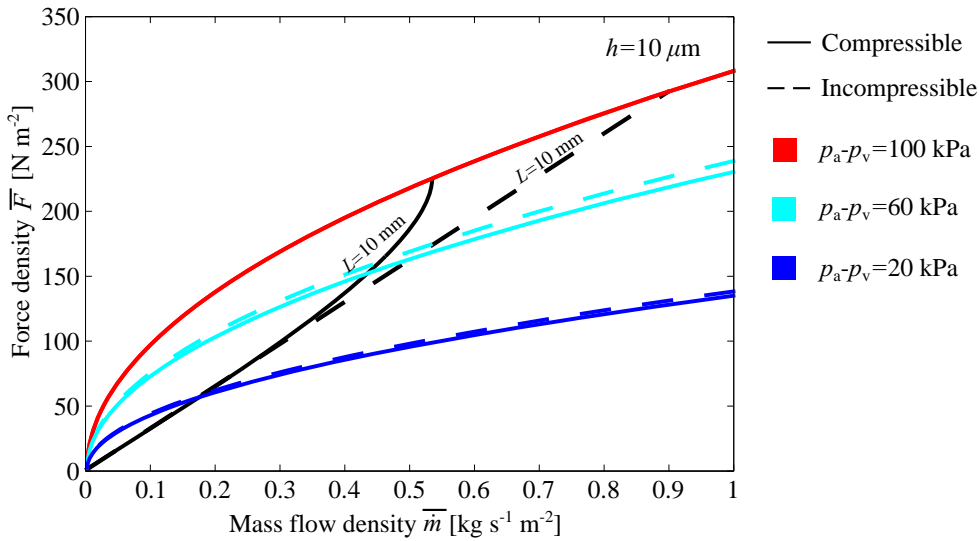


Figure 2.11: Comparison between the incompressible model and the compressible model. In this graph, using the incompressible model, for a given actuator length, when the relative vacuum pressure increases up to the limit value, e.g. 100 kPa, both the force density and flow density increase linearly (black-dash line for $L = 10$ mm). For the same situation, if the compressible model is used the relation between the force density and flow density is described by the black-solid curve. It can be concluded that the incompressible and compressible models are identical when the relative vacuum pressure is low (about 20 kPa). The disagreement between the two models increases with higher levels of the relative vacuum pressure. At 100 kPa, even though the limit curves obtained by the two models are close, the results are different (the reason for the two separate points on this limit curve obtained by the two models with the same length $L = 10$ mm).

The optimized geometry parameters are found using the same strategy as used in the previous study for incompressible media: searching for the geometry parameters α and β to maximise the force density for a given mass flow density. And perhaps surprisingly, they are still 8/9 for α and 4 for β . With this set of parameters, performance limit graphs can be built based on the compressible flow model.

Shown in Figure 2.11 is the performance limit graph for a fly height of of $10 \mu\text{m}$. As expected, for small values of the relative vacuum pressure, the results obtained by the two models are close together. The disagreement increases when the relative vacuum pressure ($p_a - p_v$) increases. It can be observed in this graph that the limit curves for the two models are very close when ($p_a - p_v$) = 100 kPa. However, it cannot be concluded that both models give the same result in this condition. When the relative vacuum pressure ($p_a - p_v$) increases, using the compressible model, the increase of the force and the flow is not linear any more. Therefore, for any point on this curve, the length of the actuator that is required may be different depending on the model. In practise, the graph obtained by the compressible model is recommended to be used to design a contactless actuation system.

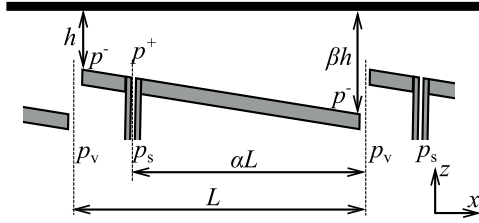


Figure 2.12: Tilt actuator geometry used for the analysis

2.3.2. Tilt surface analysis

In this study, a tilting actuator that has an infinite width and a cross-section as shown in Figure 2.7 is investigated. The length of the actuator is defined as L . α determines the location of the inlet, $0 < \alpha < 1$. The fly height h is defined as the distance from the highest point of the system to the substrate. β describes the ratio of the maximum film thickness in the actuator to the fly height, $\beta \geq 1$.

Incompressible flow model The analysis for the tilting actuator also starts with incompressible media model. Assuming the air incompressible, its density is independent from the pressure. Leaving out all the constant parameters, the Reynolds equation for the air film (Equation 2.4) becomes:

$$\frac{\partial}{\partial x} \left(-H^3 \frac{\partial p}{\partial x} \right) = 0 \quad (2.21)$$

in which H is a function of x represents the fly height distribution $H = h + x \frac{(\beta-1)h}{L}$.

Applying the boundary conditions $p = p^+$ and $p = p^-$ at the inlet and outlet respectively, the pressure distribution p can be solved. Then the inlet pressure p^+ is calculated regarding to the vacuum pressure p^- and ambient pressure p_a with the constraint of zero load capacity. The resulting equations are long and not very useful to be presented here. Instead, they are used to derive three examples of the pressure distribution of the air film in a tilting actuator as shown in Figure 2.13. It can be observed that with the zero load capacity constraint, the resulting inlet pressure p^+ is dependent on the inlet location (α). It is higher when the inlet moves to the high side of the actuator. The force density and the flow density then can be obtained using the solved pressure distribution. The result of force density is:

$$\bar{F} = \frac{1}{L} \frac{(\beta-1)h}{2} (p_a - p_v) \quad (2.22)$$

It is interesting to observe that the force density equation does not depend on α . That means the resulting force of a tilting actuator is not dependent on the location of the inlet even though the resulting inlet pressure p^+ is. Compared to the force of a step actuator, which is not dependent on the inlet location either, the generated force from a tilting actuator is half if they have a same step height (defined as the distance from the lowest point to the highest point). Because of the similarity between the tilting actuator

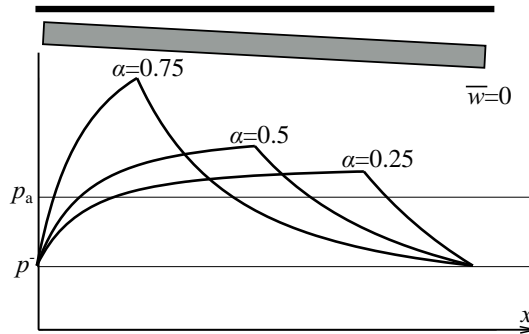


Figure 2.13: Pressure distribution of a tilt actuator for different inlet locations (incompressible model, zero load capacity)

and step actuator, the same optimization strategy has been implemented for the tilting actuator. The result of this optimization is shown in Figure 2.14. The highest efficiency is achieved with $\alpha = 0.73$ and $\beta = 7$. For the case that α is required to be 0.5, e.g. bi-directional tilting configuration, β should be equal to 5.5.

With the optimal geometry parameters, the limit graphs for tilting actuators can be built. Shown in Figure 2.15 are the curves for two cases. One is for the freely chosen inlet position and the other is for the inlet at the centre ($\alpha = 0.5$). This figure shows the benefit of the movable inlet configuration as discussed in the previous section.

Compressible flow model It is necessary to use the compressible flow model to analyse the tilting actuator when it is operating with a high value of the relative vacuum pressure. Leaving out all the constant components, the Reynolds equation for a compressible air film in a tilting actuator is:

$$\frac{\partial}{\partial x} \left(-H^3 \frac{p \partial p}{\partial x} \right) = 0 \quad (2.23)$$

Because of the presence of the pressure squared in the result of Equation 2.23, it is not possible to derive the inlet pressure p^+ symbolically from the zero load constraint equation. Therefore, a numeric result has been obtained, only for the case of central inlet point ($\alpha = 0.5$). Unlike for the step surface actuator, the force density for a tilting actuator derived with the compressible model is identical to the one obtained with the incompressible model (Equation 2.22). This means the force density still increases linearly with the increase of the relative vacuum pressure ($p_a - p_v$) for any value of the actuator length L . This interesting phenomenon will be visited again later in Chapter 4 with a general mathematical proof for 2 DoF tilting actuators. In addition, the optimal parameters are also different if the compressible assumption is used. For instance, the numeric result shows that β should be equal to 5 when $\alpha = 0.5$ (instead of 5.5 using the incompressible model).

Figure 2.16 shows the difference of the limit curves obtained by the two models for a fly height $h = 10 \mu\text{m}$. When p_v is closed to ambient pressure, the results are comparable. The mismatch increases when the relative vacuum pressure ($p_a - p_v$) increases. The limit curves obtained with compressible assumption are higher because the calculated

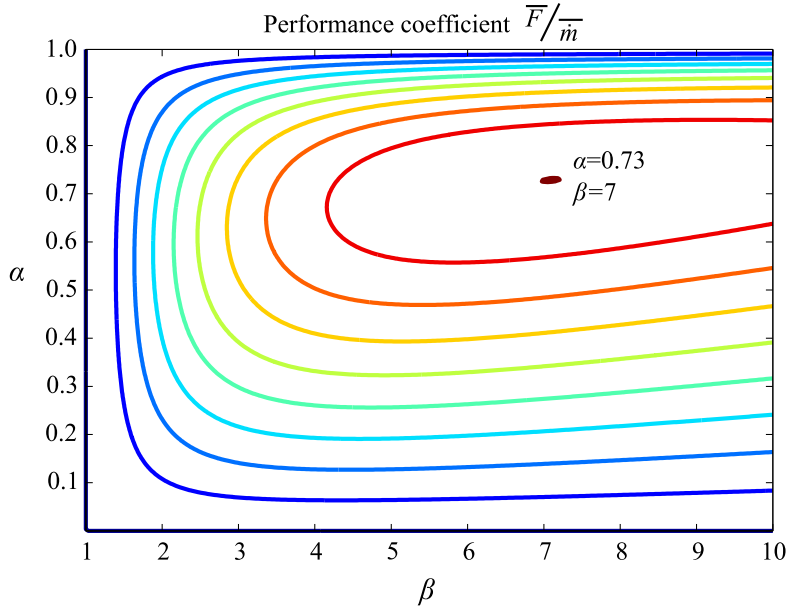


Figure 2.14: The efficiency graph of tilting actuators obtained with the incompressible flow model. The efficiency is maximal at $\alpha = 0.73$ and $\beta = 7$

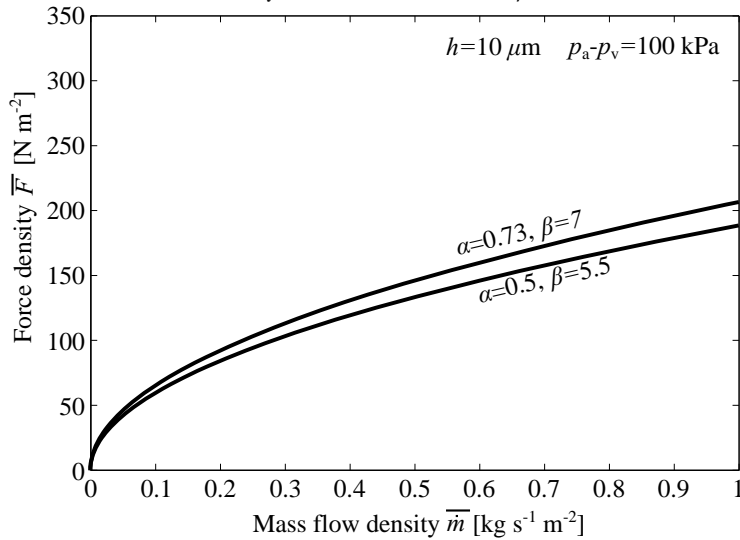


Figure 2.15: The performance limit curves of tilting actuators obtained with the incompressible flow model for two cases: One is for the freely chosen inlet position, then the optimum $\alpha = 0.73$ can be used; and the other is for the inlet required to be at the centre due to the symmetric reason.

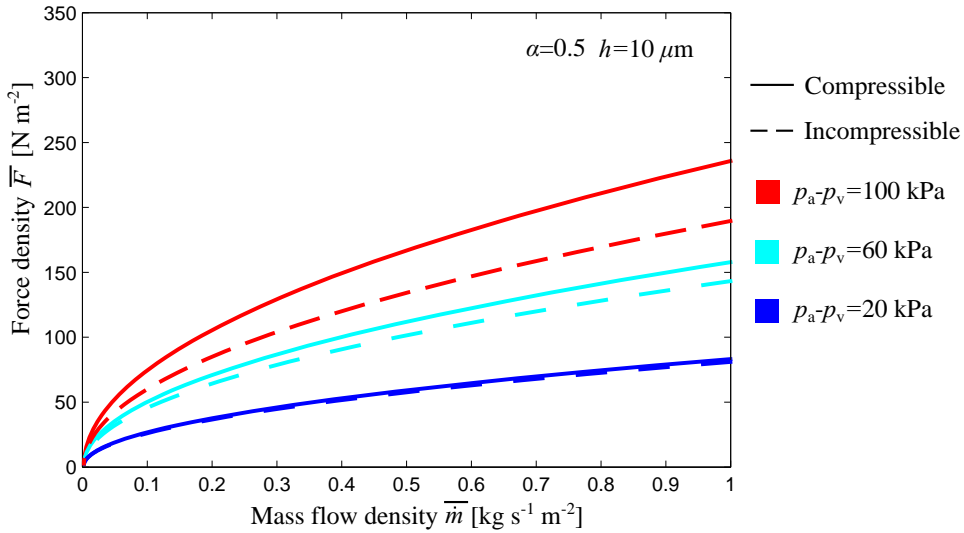


Figure 2.16: The performance limit curves of tilting actuators with central inlet point ($\alpha = 0.5$). The disagreement between the two models increases when the relative vacuum pressure ($p_a - p_v$) increases

flow density is smaller while the force density is similar compared to the incompressible model.

2.4. Comparison

2.4.1. Motor function comparison

Before the concept comparison is presented, it should be noted that all the numerical results of the analysis above have been obtained with the assumptions of zero load capacity and atmospheric ambient pressure. Because of that the maximum relative pressure ($p_a - p_v$) has been considered to be limited to 100 kPa. In reality, this is not the absolute limitation, for instance when it is possible for the system to operate in higher ambient pressure or with an opposite transport section (higher p_a , resulting in higher relative vacuum pressure). Although it is possible to extend the study for these cases, for simplicity, the comparison is presented with a typical set of operating conditions: the designed fly height is $10 \mu\text{m}$, bearing load capacity is zero, the relative vacuum supply ($p_a - p_v$) is 50 kPa.

With the analysis described above, different concepts that have been introduced in 2.2 can be compared. Figure 2.17 shows the limit curves for different concepts in identical operating conditions. The best curve is from the step surface actuator when both geometry parameters α and β are optimised. This array of actuators however can generate a force in only one direction because of the asymmetry between the inlet and outlet. For a bi-directional system, the simplest option is to arrange two single-directional actuators opposite. This results in the limit curve that is lowest in this figure due to the

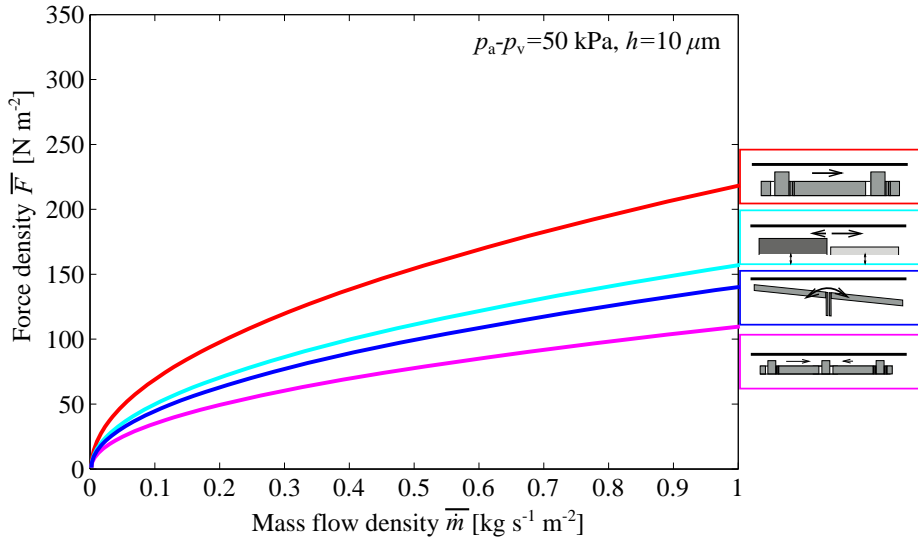


Figure 2.17: The comparison between concepts using the compressible model

fact that only half of the area is used for each direction. In contrast, the deformable step surface concept can be used to make a bi-directional system. In this configuration, because α needs to be 0.5, the limit curve is lower. However, its performance is still better compared to using pairs of opposite optimised actuators. Also shown in this figure, the deformable tilt surface concept is not as good as the deformable step surface concept. It is however much simpler to structure for a three planar degree of freedom actuation system.

2.4.2. Bearing function comparison

In order to make a full concept comparison, the bearing function also needs to be investigated. It has been stated in [56] that for a given supply pressure the maximum bearing stiffness can be achieved when the inlet restriction R_i is chosen to be equal to the actuator restriction R_a . This statement is true however not useful because the pressure supply p_s can be freely selected based on the load capacity constraint and is not theoretically limited. Indeed, from the study in the previous section, as long as the thin substrate floats on top of the contactless actuation system, the force is determined by the relative vacuum pressure only. The positive pressure is required to keep the substrate levitated (maintain a constant load capacity). In theory, the pressure supply can be designed to have a very big value. Together with a corresponding inlet restriction for the load constraint, the resulted stiffness can be higher than the one found in [56]. Following is a brief mathematical proof for this statement. Then a strategy of designing the inlet restriction in practise will be proposed. Finally, the bearing performance of different concepts will be compared.

For simplicity, the stiffness analysis is presented for the step surface actuator with

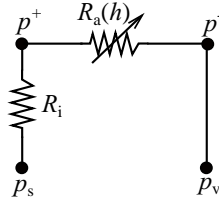


Figure 2.18: Flow schematic of an actuator

the assumption of incompressible media. Considering a step surface actuator in Figure 2.7, its equivalent flow schematic can be presented as in Figure 2.18.

With the incompressible assumption, the volume flow is preserved. At the design fly height $h = h_0$, the balance flow equation is:

$$\frac{p_s - p_v}{R_a(h_0) + R_i} = \frac{p^+(h_0) - p_v}{R_a(h_0)} \quad (2.24)$$

in which $R_a(h_0)$ and $p^+(h_0)$ are respectively the restriction of the actuator gap and the inlet pressure at the designed fly height. $p^+(h_0)$ is defined by the zero load capacity constraint, $p^+(h_0) = 2p_a - p_v$. Equation 2.24 can be written as:

$$\frac{p_s - p_v}{R_a(h_0) + R_i} = \frac{2(p_a - p_v)}{R_a(h_0)} \quad (2.25)$$

For a small variation of the fly height from the designed value, the inlet pressure will change. And thus the load capacity will change. This variation in load capacity as a result of a change in fly height is equal to the bearing stiffness. Using the balance flow equation, the inlet pressure when the substrate flies with a height h can be calculated:

$$p^+(h) = \frac{p_s - p_v}{R_a(h) + R_i} R_a(h) + p_v \quad (2.26)$$

The bearing stiffness per unit area at the designed fly height h_0 can be obtained:

$$\bar{k}(h_0) = - \left. \frac{dw(h)}{dh} \right|_{h=h_0} = - \left. \frac{1}{2} \frac{dp^+(h)}{dh} \right|_{h=h_0} \quad (2.27)$$

$$= - \left. \frac{dR_a(h)}{dh} \right|_{h=h_0} \frac{R_i(p_s - p_v)}{2(R_a(h_0) + R_i)^2} \quad (2.28)$$

Combine with Equation 2.25, the stiffness at the designed fly height becomes:

$$\bar{k}(h_0) = - \left. \frac{dR_a(h)}{dh} \right|_{h=h_0} (p_a - p_v) \frac{R_i}{R_a(h_0)(R_a(h_0) + R_i)} \quad (2.29)$$

Note that the actuator restriction $R_a(h_0)$ and its derivative $\left. \frac{dR_a(h)}{dh} \right|_{h=h_0}$ at the designed fly height h_0 are dependent only on the actuator geometry. From this equation, the maximum stiffness is obtained when the last term is maximised.

$$\bar{k}(h_0)_{\max} = - \left. \frac{dR_a(h)}{dh} \right|_{h=h_0} (p_a - p_v) \frac{1}{R_a(h_0)} \text{ when } R_i \rightarrow \infty \quad (2.30)$$

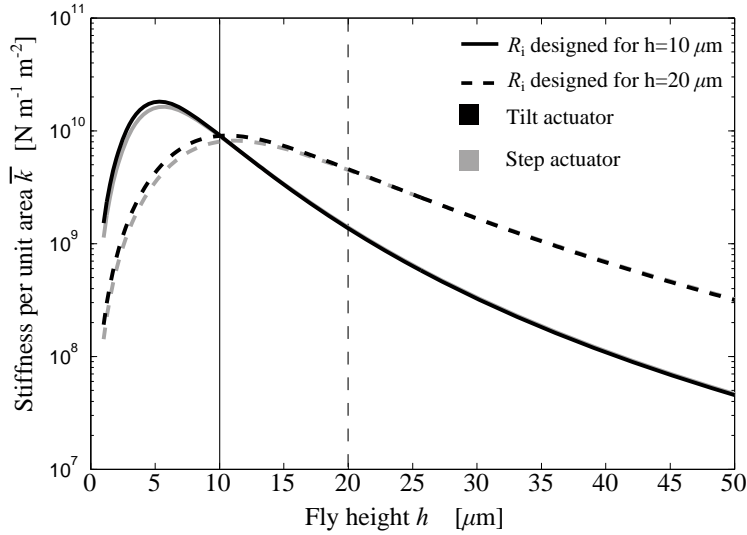


Figure 2.19: Comparison between the step surface actuator and the tilt surface actuator for the stiffness per unit area at different fly heights. R_i is fixed at designed values: designed height is 10 and 20 μm when $p_s = 300 \text{ kPa}$ and $p_v = 50 \text{ kPa}$. With this method of selecting R_i for the substrate to fly at the designed height when the (assumed) maximum pressure is applied, the maximum bearing stiffness can be achieved (for this specified operating condition). As presented in this graph, if the load changes, for instance by an out-of-plane external force, the fly height will change, thus the bearing stiffness changes accordingly.

In words, the inlet restriction should be as big as possible in order to maximise bearing stiffness. The supply pressure p_s needs to be correspondingly increased to generate a sufficient inlet pressure p^+ for the substrate to fly with the designed height. This statement also holds for the tilt surface actuator. Furthermore, it is still true when the bearing stiffness is derived with the compressible assumption.

In practise, the pressure supply will be the limiting factor. In order to maximise the bearing stiffness, the inlet restriction should be chosen such that the substrate can fly with the designed height when the maximum supply pressure is applied. For a comparison, the supply pressure is assumed to have a maximum level of absolute 300 kPa. As shown in Figure 2.19, the bearing stiffness of different concepts is compared given the operating condition that $(p_a - p_v) = 50 \text{ kPa}$.

In this graph, for each type of actuator, the inlet restriction is first calculated for a designed fly height, e.g. 10 and 20 μm . The bearing stiffness is then obtained for different fly height (compressible model) while the inlet restriction is fixed with the designed value. For the step surface actuator, even though it has been stated that the stiffness is dependent on the actuator geometry, within the condition of the pressure supply, the calculated inlet restriction changes such that the system will give the same stiffness behaviour. In other words, if p_s and p_v are constrained the maximum stiffness is independent of the geometry parameters α and β . In contrast, for the tilting surface actuator, the stiffness behaviour relies on the actuator geometry. Presented in this figure is the stiffness of a tilt surface actuator with $\alpha = 0.5$ and $\beta = 5$, the parameter set for the optimum

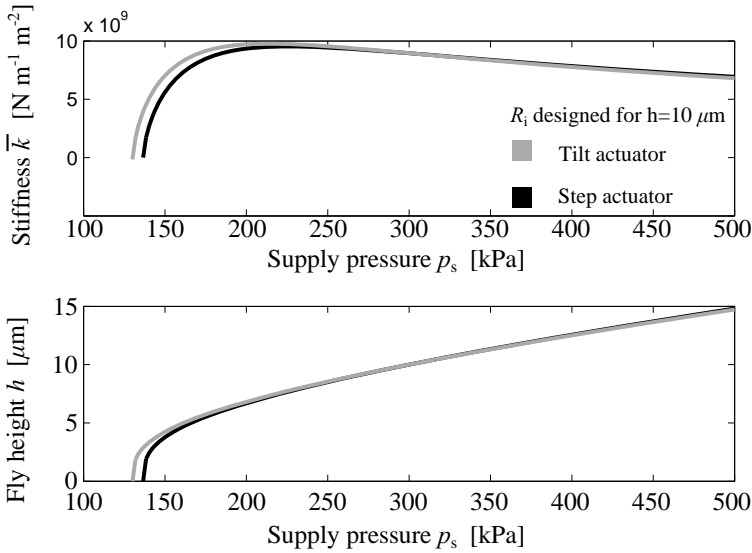


Figure 2.20: Fly height and stiffness per unit area for different supply pressure values. R_i is fixed at designed values: designed height is 10 and 20 μm when $p_s = 300 \text{ kPa}$ and $p_v = 50 \text{ kPa}$. The substrate starts to fly up when p_s reaches a value that makes the load capacity to change from negative to zero. After that, the fly height continuously increases in order to maintain the zero load capacity constraint.

motor function. A final remark for this graph is that the y -axis represents the stiffness per unit area that is independent of the actuator length. This means the stiffness behaviour of an actuator array is similar for every point on a limit curve of the motor function, which has been presented in previous sections.

The graph in Figure 2.19 shows the stiffness variation when the fly height is changed because of a load capacity deviation, for instance an out-of-plane external force or an out-of-plane acceleration. In a contactless actuation system, the fly height and the stiffness also change when the supply pressure is varied. In Figure 2.20, the resulting fly height and the corresponding bearing stiffness are depicted when the supply pressure is increased from 100 kPa (p_a) to 500 kPa. The inlet restriction is fixed with the value that is designed for the substrate to fly with a height of 10 μm when $p_s = 300 \text{ kPa}$ and $(p_a - p_v) = 50 \text{ kPa}$. The substrate starts to fly up when p_s reaches a value that makes the load capacity to change from negative to zero. After that, the fly height continuously increases in order to maintain the zero load capacity constraint. It can be observed that the stiffness is very small when the substrate just starts to fly up. The reason is that in this situation, the actuator restriction R_a is extremely big compared to the inlet restriction R_i , a small perturbation of the fly height cannot change the result of the inlet pressure p^+ . Similar reason can also be used to explain the low stiffness when the fly height is large, R_a becomes too small compared to R_i . From the stiffness analysis, it can be concluded that the stiffness performance of all concepts are comparable.

2.5. Conclusion

In this chapter, first, different concepts have been introduced that can be used to build a contactless actuation system using the viscous traction force of an air film. The possible advantages and disadvantages of each one have been described. Second, a mathematical model has been developed in order to characterise the performance of each concept. It is based on both incompressible and compressible assumptions in order to build a better understanding of the principle. Making use of this model, the optimum geometry for each concept has been found. It does not only help in designing a system that can generate the largest force for a limited flow rate but also in determining the theoretical limit of the viscous traction force principle. With the optimal parameter sets, different concepts have been compared in regard of the static performance. For a single-directional system, the best performance is from the static step surface concept. For a bi-directional system, the best choice would be the deformable step surface that has a moderate performance and is simple to manufacture. Of course with some modifications, the static step surface concept can be used to structure a bi-directional system. However, it will be either more complex or have less performance. For a three planar degree of freedoms system, because of simplicity and feasibility, the deformable tilt surface is most suitable even if its performance is slightly lower than the deformable step surface. In addition to analysing the motor function, the bearing function has also been studied. Within the same operating conditions, the stiffness created by all concepts is very high and comparable, and certainly sufficient for practical applications.

Next to characterising the performance of different concepts, a guide line of designing a contactless actuation system has been proposed. To summarise, it consists of three steps:

1. Step 1: The operating fly height is chosen considering the manufacturability of aspects such as tolerance, flatness and roughness.
2. Step 2: The length of each actuator in the array is determined using the performance limit curve for the designed fly height in step one. In any application, the active area is limited by the substrate area. With the specifications of the vacuum supply on the pressure level and the maximum flow rate at that level, the vacuum pressure p_v and the flow density can be defined. From this information, the limit curve can be obtained. Using this curve, the actuator length can be designed in order to achieve a desired force. Note that smaller actuator gives higher force, but manufacturing small actuators is more expensive and challenging. This step can be modified to determine the required vacuum supply for a specific application.
3. Step 3: The inlet restriction is chosen such that the substrate can fly at the designed height when the pressure and vacuum supply are applied with their practical limits. This inlet restriction will guarantee the highest bearing stiffness that can be created by this system.

3

NUMERICAL MODEL AND EXPERIMENTAL VALIDATION

In the previous chapter, an analytical model has been developed in order to predict the static performance of a contactless actuation system, based on Reynolds equation for thin film media. Using this model, the actuator geometry has been optimised such that the air consumption is minimised for a required force. To make reliably use of this optimisation for designing, this model needs to be validated. This chapter presents an experimental validation as well as some model improvements.

3.1. The tilted air bearing experiment

Because of the combination of the performance and the feasibility, the tilting deformable surface concept has been chosen for the further development of a three planar degree of freedom contactless actuation system. Therefore, an air bearing with statically tilted surface sections has been built as an experimental setup for the validation of static performance, focusing mainly on the achieved force and the consumed flow.

3.1.1. Setup description

Shown in Figure 3.1 is a sketch of the tilted air bearing (not to scale). Its realisation is illustrated in Figure 3.2. The setup's components are:

Bearing part The tilted bearing is made of aluminium using conventional milling. It consists of seven sections that are structured like a stair with a designed step height of $25\ \mu\text{m}$. Each section has a length of 10 mm and a width of 60 mm. This size of the bearing is designed for it to be fully covered by a 100 mm diameter wafer. An inlet groove is designed at the middle of each step. Outlet grooves are located at the sides. Every groove has five holes connected to the manifold. Four of them are used to evenly distribute

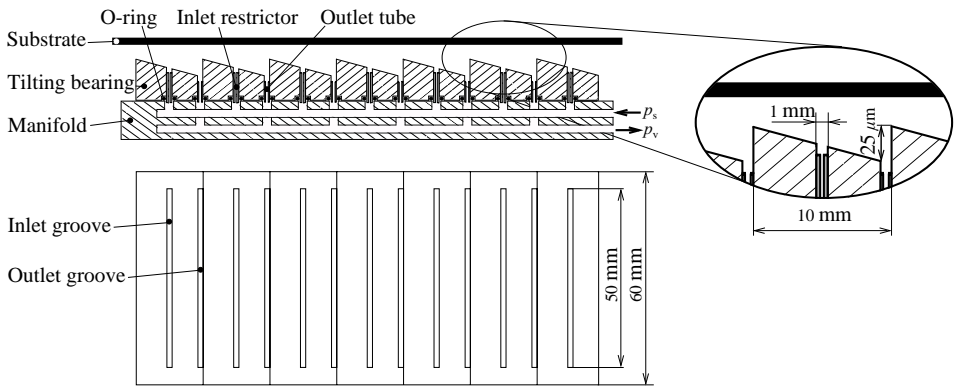


Figure 3.1: Schematic cross-section view of the tilting air bearing (not to scale)

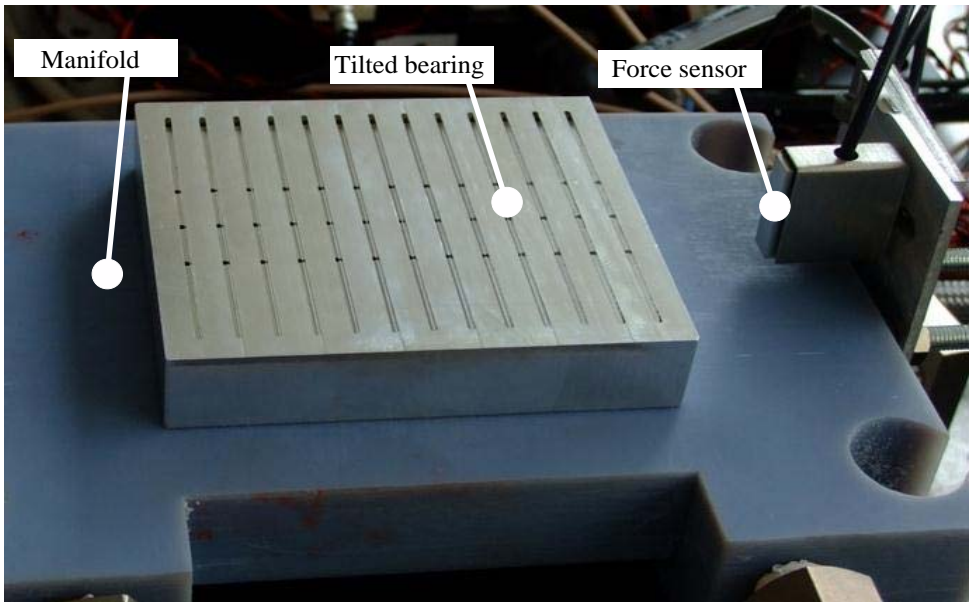


Figure 3.2: Photo of the realised statically tilted air bearing setup

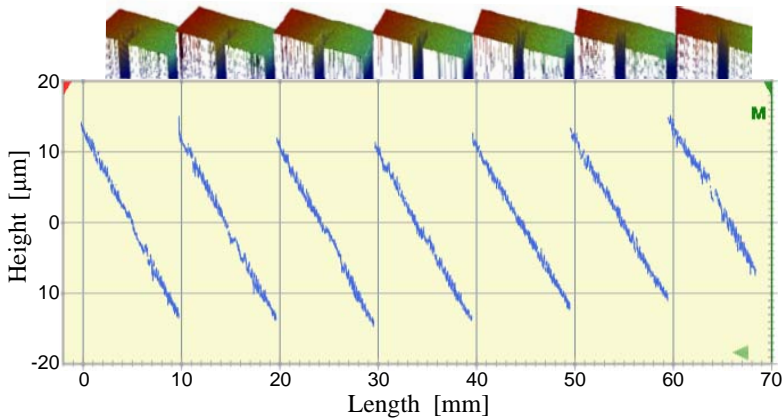


Figure 3.3: Measured surface topology of the tilted air bearing

the air flow to/from the actuator. The remaining hole links to a sensing channel of the manifold that is used to measure the pressure at the grooves (p^+ and p^-).

The bearing surface topology has been measured with a white light interferometry instrument. As shown partly in Figure 3.3, the surface quality is not perfect but good enough for the validating experiments. The resulting step height varies from $24 \mu\text{m}$ to $26 \mu\text{m}$.

Restrictors All the inlet and outlet grooves of the bearing part are connected to the manifold through capillary tubing. The outer diameter and the length are chosen to be 1.6 mm and 14 mm respectively. For the outlets, the only function of these tubes is sealing (combined with O-rings). The inner diameter of the outlet tubes is therefore chosen to have the biggest value that is available, 1 mm. In contrast, the function of capillary tubes at the inlets is to increase the flow restriction in order to create a positive bearing stiffness on the floating substrate. The inner diameter of the inlet tubes is chosen to be 0.38 mm. As stated by the tubing supplier, the inner diameter tolerance is ± 0.013 mm, resulting a relatively large deviation of the calculated restriction, $\pm 12\%$ for 0.38 mm tubes. Furthermore, the flow inside the inlet restrictor is purely turbulent, the Poiseuille equation for the flow resistance cannot be used to choose the length and the inner diameter of the inlet restrictors. Therefore, they have been dimensioned according to an experimental restriction measurement. The inlet restriction is designed to be approximately equal to the actuator restriction when the fly height is $10 \mu\text{m}$.

Manifold The manifold used in this experimental setup has been made with an additive manufacturing method, Polyjet 3D printing. This printer has two jetting heads that projects outlines of the part, layer by layer. One head sprays a photo-polymer liquid, which get cured almost instantly by an UV lamp, and creates a solid, plastic-like model as desired. The other head injects support material that is like wax and needs to be washed away afterwards. This manufacturing method is cheap and fast, but suitable

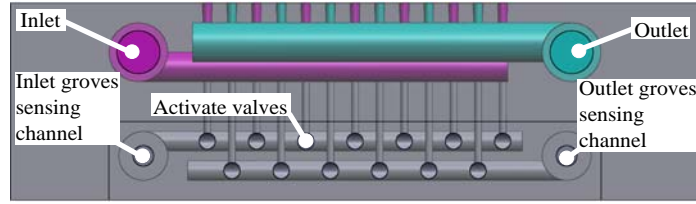


Figure 3.4: Transparent front view of the manifold

3

only for a small and simple manifold. The support material inside the canal system is very difficult to be removed if it is long and has a complicated structure.

Shown in Figure 3.4 is the (transparent) front view of the manifold. It consists of one pressure supply channel, one vacuum channel and two sensing channels. The diameter of the supply and vacuum channels is relatively big compared to the restrictors' diameter (10 mm for the main section and 3 mm for the branches) so that the manifold restriction is negligible. Thus it is valid to measure the supply and vacuum pressure (p_s and p_v) at the entrances of the channels (outside the manifold). Next to these main channels, there are two sensing channels that are used to measure the pressure at the grooves (p^+ and p^-), one for the inlets and one for the outlets. Each groove is connected to a channel through an activating valve that is set by a screw. With this structure, only two pressure sensors are required to measure all the pressure values in the grooves. Because all the measurements obtained with this setup are static, it can be considered that there is no flow that goes through these sensing channels (blocked by the sensors). Therefore, the pressure drop over the sensing channels is zero, thus the read out values from the sensors are identical to the pressure at the grooves.

Sensors There are three types of sensors used in this experimental setup. A force sensor is placed at one side of the setup to measure the generated force from the tilting air bearing (Figure 3.2). It is a Futek sensor, model LSB200 s-beam load-cell, and has a force measuring range from -0.2 N to 0.2 N. In order to measure the flow rate, a mass flow sensor has been placed in series with the setup at the supply side. This flow sensor, AWM720P1 from Honeywell, can measure a flow up to 200 SLPM. The pressure is measured with MPX pressure sensors from Freescale. These sensors are available in various ranges, from tens of Pa to several Bars. In order to achieve high accuracy, four different sensors have been chosen that have just wide enough range to read the pressure levels in different channels of the manifold.

3.1.2. Experimental result

With this statically tilted air bearing, the static performance has been obtained. The first experiment is to measure only the achieved force and the flow rate. The measurements of the fly height and the pressure distribution in the air film will be presented in the later sections. In this experiment, the vacuum pressure p_v is kept at a constant level, i.e. 75 kPa absolute. The supply pressure p_s is increased from ambient pressure, 100 kPa absolute. When the supply pressure reaches 140 kPa absolute, there is no remaining

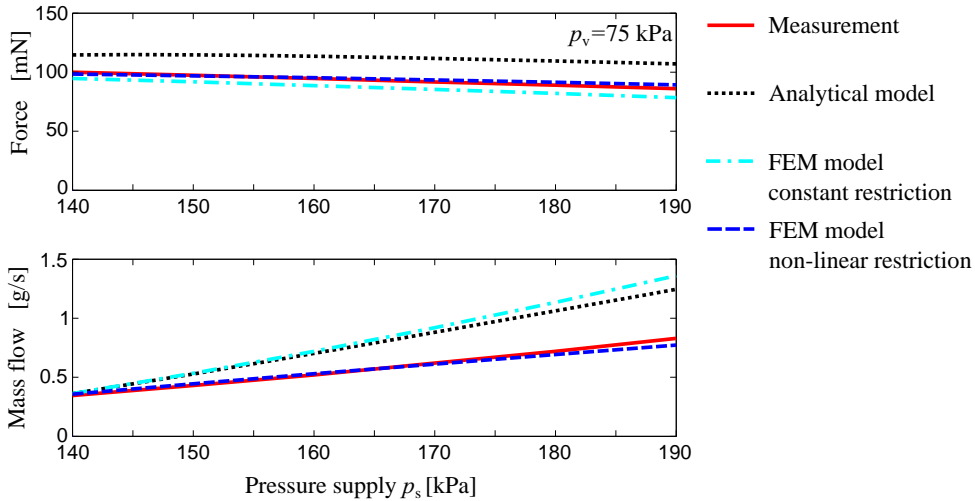


Figure 3.5: Result comparison between measurement and prediction. The operating conditions is $p_a - p_v = 25$ kPa. p_s is varied, and is sufficient to make the wafer fully levitated.

contact between the wafer and the bearing surface. In Figure 3.5, the resulting force and the flow rate are shown when the wafer is fully levitated. From the result, a force density of 23.8 N m^{-2} can be achieved with a relatively low vacuum supply. This force can generate an acceleration of 10 ms^{-2} on a substrate that has 1 mm thickness.

In the measurement result, it can be observed that when the supply pressure increases, the force decreases whereas the flow increases. One might think this contradicts the analysis in Chapter 2 where it has been stated that the traction force is dependent only on the vacuum supply. Actually, in that analysis, the zero outlet restriction assumption has been made for simplicity. That assumption however, has limited validity in reality. The practical outlet restriction is small but not zero. When the supply pressure is increased, the fly height increases. This results in a significant increase of the flow due to the fact that the flow is proportional to the fly height to the third power. Therefore, the pressure drop over the outlet tube increases because of its non-zero restriction. As a result, the achieving force slightly reduces. As shown in Figure 3.5, when a non-zero value is used for the outlet restriction in the analytical model, this trend of the result has been predicted.

From the result shown in Figure 3.5, there is a large quantitative difference between the analytical prediction and the measurement. This makes sense since the analytical model does not take into account the effect at the edges of the system where the air goes in or out without generating force in the desired direction. In addition, in the analytical model the inlets and outlets are assumed to be infinitely small while in reality the grooves' area takes approximately 20% of the total surface. In order to have a better prediction, an FEM model has been developed, and is presented in the next section.

3.2. Numerical model development

In order to predict the performance of the tilting air bearing more accurately, a FEM model has been developed based on Reynolds equation for thin film flow. The geometry of the bearing surface has been implemented directly into the model, including the grooves' geometry. The edge effect is easily taken into account by setting the outer edges to have a fixed value, ambient pressure p_a . At the inlets and outlets, the mass flow equations are entered:

$$\dot{m}_{\text{inlet}} = \frac{p_s + p}{2R_g T} \frac{p_s - p}{R_i} \quad (3.1)$$

$$\dot{m}_{\text{outlet}} = \frac{p + p_v}{2R_g T} \frac{p - p_v}{R_o} \quad (3.2)$$

where R_i and R_o are the inflow and outflow resistance respectively.

The fly height h_0 determination is realised using

$$\int (p(h_0) - p_a) dA = 0 \quad (3.3)$$

The result of this FEM model is presented in Figure 3.5. Compared to the result obtained by the analytical model, the predicted force is much closer to the measurement. Indeed, because the edge effect is taken into account, the effective area, on which the force is generated, is better estimated. However, the predicted flow is still far off from the measurement result. This is caused by an incorrectly calculated fly height. Two possibilities of the wrong prediction for the fly height have been considered. First, the restriction values in the model might be different from the real restriction. Second, the substrate in reality is not infinitely stiff, and its deformation due to the pressure difference might lead to a wrong calculation for the fly height, thus the flow. From this, two improvements of the FEM model are described.

3.2.1. Model improvement - nonlinear restriction

In Section 2.4.2, it has been explained that when the vacuum supply and the inlet restriction are kept constant, if the pressure supply increases the fly height will increase in order to maintain a constant load capacity, which is required to carry the substrate. This understanding can be formulated differently: when the pressure and vacuum supplies are kept constant, the resulting fly height will be smaller if a bigger inlet restriction is used. In other words, for a fixed operating condition p_s and p_v , the fly height is dependent on the inlet restriction (and on the outlet restriction).

In the FEM model described above, an experimental value of the inlet restriction has been implemented, $2 \cdot 10^9 [\text{Pa s m}^{-3}]$. This value is obtained by measuring the flow while applying a certain pressure difference across the restrictor, i.e. 25kPa. Using the same method, the outlet restriction has been obtained, $0.1 \cdot 10^9 [\text{Pa s m}^{-3}]$. However, these values might be not correct because the measurements have been conducted not with the exact pressure differences as found in the experiment. Therefore, in the model they have been multiplied by a constant tuning factor to observe if it is possible to correct the

flow prediction. With this tuning coefficient, the flow prediction in Figure 3.5 just moves up or down with a small change of the trend. This method is not suitable for correcting the flow prediction of the FEM model over the full range of the supply pressure.

The assumption of Poiseuille type of the air flow in the restrictor is not valid in this experiment. The flow resistance might be better derived from Darcy-Weisbach equation, for an incompressible flow in a circular pipe the pressure loss can be expressed:

$$\Delta p = f_D \frac{\rho V^2 L}{2 D} \quad (3.4)$$

where ρ is the fluid density, V is the mean flow velocity, L and D are the length and the diameter of the pipe, f_D is the Darcy-Weisbach friction factor that can be determined using Moody's chart [34] where the friction factor is plotted against Reynolds number for different values of relative roughness of the pipe.

Since the restrictors used in the setup are commercial tubes, it is very difficult to determine the relative roughness. Furthermore, it might not be valid to treat the air flow in the restrictors as incompressible. Therefore, the restriction has been measured with a method that is frequently used to determine the discharge coefficient of an orifice restrictor: measuring the mass flow rate (indirectly from the pressure level) while the gas is discharged from a vessel through the restrictor. With this method, the restriction can be obtained as a function of the pressure drop over the restrictor. As shown in Figure 3.6, the measured restriction increases non-linearly when the pressure difference increases. Using a fitting tool, the measured restriction has been modelled as a function of the pressure difference between the two ends of the restrictor, and implemented into the FEM model. Shown in Figure 3.5, the predicted flow obtained by this model is much better. When the supply pressure p_s increases, because of the resulting increase of the restriction, the fly height does not increase as much compared to the model with a constant restriction value. Therefore, the increasing trend of the flow has been improved, to be more accurate.

There is still a small difference between the prediction and the measurement. One of the reasons could be due to the deformation of the substrate that has not been modelled yet. Another reason is that the restriction measurement of one restrictor shown in Figure 3.6 does not represent well all restrictors in the system (60 pieces). Indeed, the restriction measurement of another randomly chosen "identical" restrictor shows about 10 % difference. This deviation might be caused by either the tolerance of the capillary tubes or the difference in the cut of each tube. For a 10% deviation of the restriction and a 4% deviation of the step height ($\pm 1\mu\text{m}$) added into the model, the simulation result has covered the experimental result (Figure 3.7).

3.2.2. Model improvement - substrate deformation coupling

This section presents an improved model that takes into account the deformation of the substrate. This deformation is caused by the non-uniform pressure distribution in the air film. But also, the pressure distribution is affected by the resulting deformation of the substrate due to the change of the local fly height. Due to the small film thickness and the strong dependence of the pressure on this film thickness, a direct non-linear

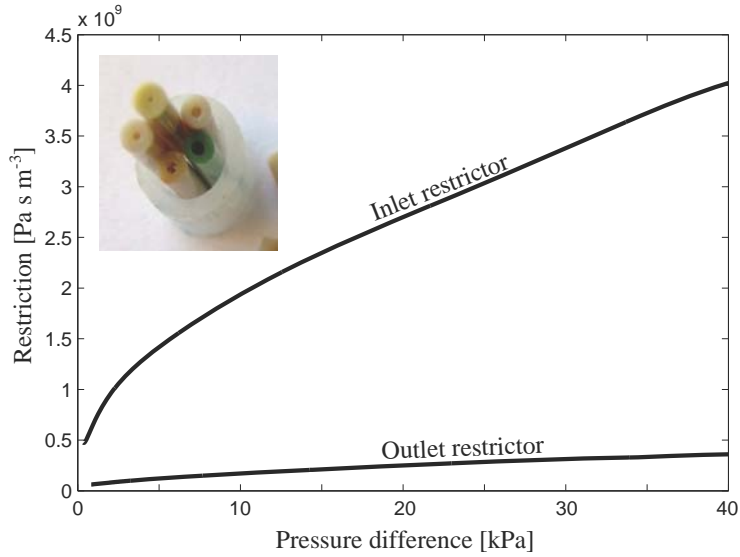


Figure 3.6: The measured restriction shows that it is not constant in the operating conditions of the tilted air bearing.

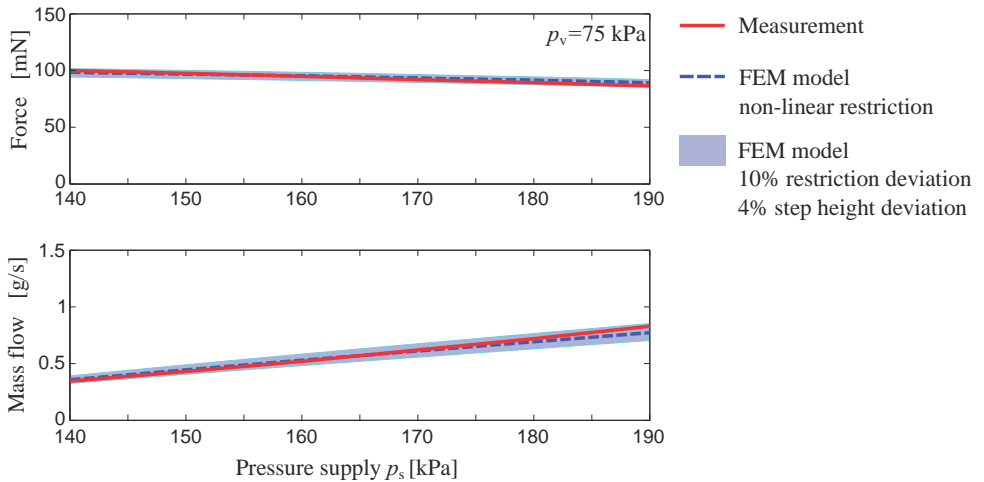


Figure 3.7: Assuming a 10% deviation of the restriction and a 4% deviation of the step height, the numerical results cover the experimental values. The prediction is produced by the FEM model implemented non-linear restriction.

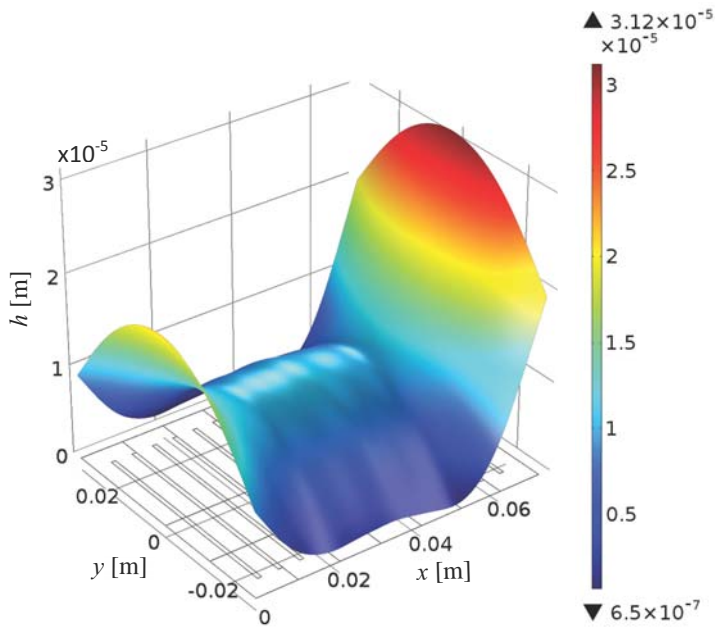


Figure 3.8: The fly height profile estimated by the improved FEM model. The shown fly height is defined as the distance from the substrate to a virtual flat surface that contains the highest point of the system. The operating conditions are $p_v = 75$ kPa absolute and $p_s = 140$ kPa absolute.

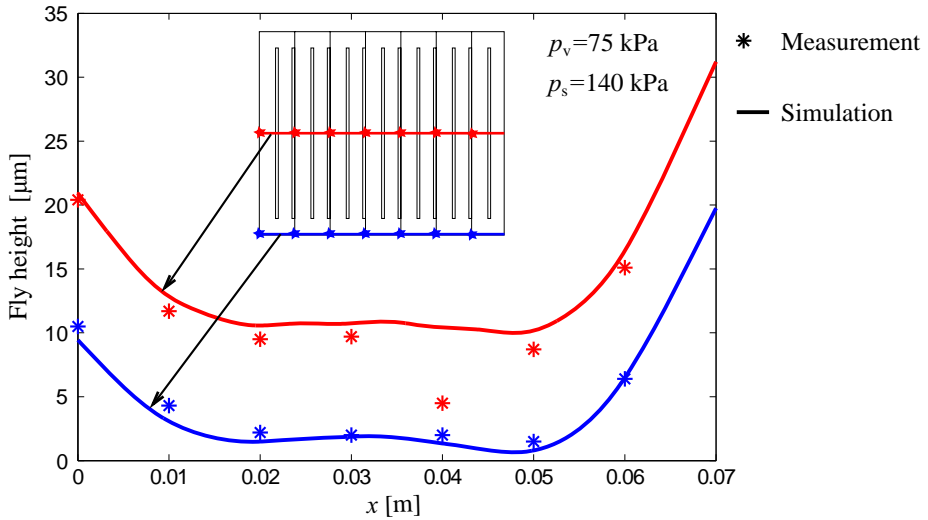


Figure 3.9: The fly height measured at several points shows a remarkable prediction of the fly height profile produced by the latest FEM model. The operating conditions are $p_v = 75$ kPa and $p_s = 140$ kPa.

solution of the model is complex. However, using a parametric study when the substrate is stepwise reduced from a high value (little deformation) to the actual thickness, a stable numerical procedure has been found. In Figure 3.8, the predicted profile of the fly height, which is a combination of the solved average fly height and the substrate deformation, is shown for the operating case $p_s = 140$ kPa absolute. Compared to the measured fly height at several points shown in Figure 3.9, this model has produced a remarkable accurate prediction for the distributed fly height. In addition, from the result of pressure measurements at the grooves, it can be concluded that the model with deformation coupling is also more accurate in predicting the pressure distribution (Figure 3.10). The force and the flow calculated by this model however do not exhibit a significant difference. This might be explained by the fact that the deformation only has a local effect. This improved model shows forces and flows that are close to the experimental result and the previous, more basic, model, thus confirming the observation that the basic model without substrate deformation is sufficiently accurate to predict force and flow.

This simulation also explains clearly why the substrate starts flying when the pressure supply reaches 140 kPa absolute. At this pressure the contact at the edge of the wafer is just broken. From the simulation, there are two types of deformation. The larger one, saddle shape, is caused by the different properties of the pressure and the bearing stiffness that are distributed in the area near the edges. The smaller deformation, the waves at the middle area, is the result of the pressure difference between the inlet and outlet in each segment. In order to reduce the fly height, thus the air consumption, the design effort should focus on preventing contacts at the edges caused by the global deformation. The deformation caused by the in/outlet pressure difference is small for this substrate, therefore not important.

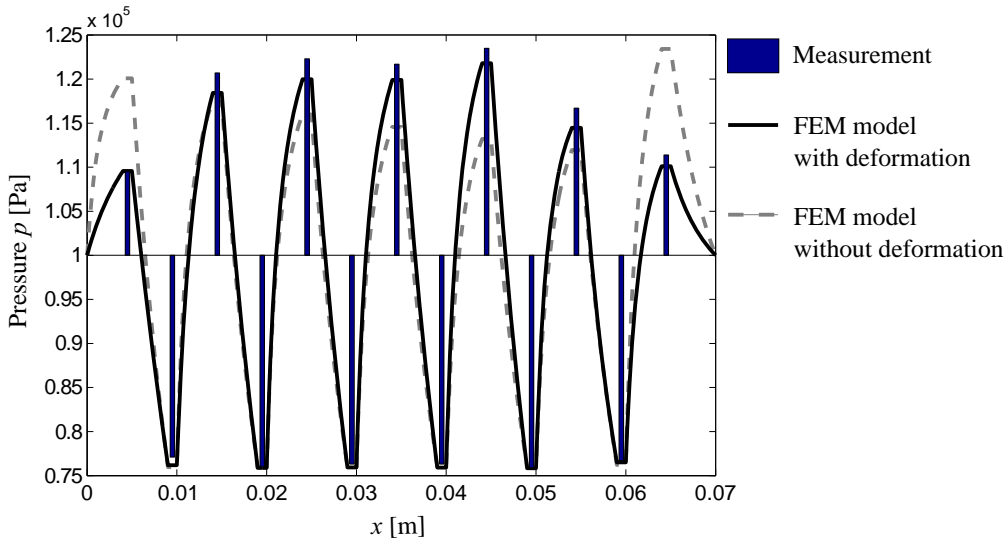


Figure 3.10: The FEM model that takes into account the substrate deformation shows a better prediction for the pressure distribution. The operating conditions are $p_v = 75$ kPa and $p_s = 140$ kPa.

3.3. Conclusion

In this chapter, an experimental setup has been described. The measurement result shows that the static behaviour of the tilting air bearing has been predicted by the analytical model based on Reynolds equation for thin film media. However, there is mismatch between the model and the experiment due to the fact that the analytical model cannot take into account the effect at the edge where the air flow does not generate desired forces. A FEM model has been developed also based on Reynolds equation, in order to obtain a more precise prediction. This latest FEM model has shown that the static performance of a tilting air bearing can be predicted accurately. The prediction has been verified, not only for force and flow but also for the substrate deformation and the pressure distribution. To summarise, some conclusions can be drawn from this chapter:

- Models developed based on Reynolds equation are efficient to predict the static behaviour of a contactless actuation system accurately. The prediction has been verified successfully by experiments.
- With only a good knowledge of the bearing surface geometry, the force can already be predicted well. However, in order to have an accurate estimation for the fly height and the flow rate, the restriction of the inlets and outlets must be modelled as well.
- One of the goals of this experimental setup is to verify the geometry optimisation based on the analytical model that is developed in Chapter 2. Even though the analytical model does not produce an exact prediction, it is still valid. Indeed, it has been developed based on Reynolds equation which has proven to be sufficient

to model this type of contactless actuation systems. The error of the analytical prediction is mainly caused by practical factors such as the edge effect and the non-linear restriction.

- A smaller fly height gives a better performance. 'What is the smallest fly height that we can realise in practice?' is an interesting question that has been partly answered in this chapter. Currently, the fly height is limited by the substrate deformation.
- The developed model has predicted accurately not only the force and the flow but also the pressure distribution and the substrate deformation. From the deformation prediction, mechanical contacts occur mostly at the edge of the substrate or the system due to the low bearing stiffness in that area. Adding a passive air bearing at the edge of the system that compensates for this reduction in bearing stiffness might be a solution in order to further reduce the fly height and the air consumption.

4

ACTUATOR DESIGN FOR A THREE PLANAR DOF SYSTEM

In previous chapters, predictive models have been developed and validated for a single directional actuator array. In this chapter, they are used to analyse the static performance of a three degree of freedom actuation system. The main goal of this analysis is to find the optimised design with respect to the shape of the actuator, the size of the inlet and outlet.

4.1. Actuator design for a three DoF system

Introduced in Chapter 2, a three DoF contactless actuation system can be built by arranging two DoF tilting actuators into an array. As illustrated in Figure 4.1, the planar translational actuation is produced by tilting all actuators in one direction. The rotational degree of freedom is obtained by the opposing tilting of actuator pairs. In this section, 2 DoF tilting actuators are analysed with the FEM model based on Reynolds equation for compressible thin film media, which is described in Chapter 3.

In all numerical studies presented in this section, the outlet pressure p^- is assumed to be constant, e.g. -50 kPa relative. The fly height, defined as the minimal distance between the actuator and the substrate, is assumed to be $10\ \mu\text{m}$. The inlet pressure p^+ is the result of the constant bearing load capacity constraint. The analysis starts with the

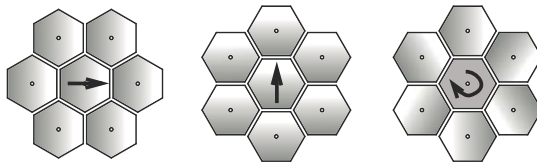


Figure 4.1: A three DoF contactless actuation system can be built by two DoF tilting actuators

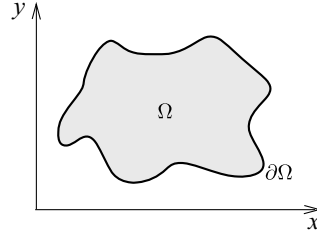


Figure 4.2: Representing a typical actuator, the region Ω bounded by $\partial\Omega$ is used for a mathematical proof, showing that the force created by a tilt actuator is not dependent on the actuator's shape.

study on the effect of actuator shape.

4

4.1.1. Effect of actuator shape

Equation 2.22 (section 2.3) has shown that the force density of a single DoF tilted actuator is proportional to the tilting angle and the relative vacuum pressure ($p_a - p^-$). It is rewritten:

$$\begin{aligned}\bar{F} &= \frac{1}{l} \frac{(\beta-1)h}{2} (p_a - p^-) \\ &\approx \frac{\varphi}{2} (p_a - p^-)\end{aligned}\quad (4.1)$$

in which $\varphi \approx \frac{(\beta-1)h}{l}$ is the tilting angle since $(\beta-1)h$ is the difference in height between the lowest point and the highest point of a single DoF actuator.

The force density of a single DoF tilted actuator is not dependent on either the actuator size (the length l) or the inlet location (parameter α). This interesting phenomenon is observed again with 2 DoF actuators. Following is the mathematical proof for this statement. Consider an actuator that has a freely chosen shape represented by the region Ω shown in Figure 4.2. Ω is bounded by a simple closed curve $\partial\Omega$ and has an area S_a . The pressure on the boundary $\partial\Omega$ is constant, e.g. outlet pressure p^- . An inlet is assumed to be inside Ω in order to generate a sufficient average pressure for the substrate to fly. This is represented by the equation of the load capacity that has been assumed to be zero because of the small weight of the thin substrate:

$$\int_{\Omega} (p - p_a) dx dy = 0 \quad (4.2)$$

When the actuator is tilted with a small angle φ , for instance in x -direction, the generated force can be calculated:

$$F_x = \int_{\Omega} -\frac{H}{2} \frac{\partial p}{\partial x} dx dy \quad (4.3)$$

in which H is the height distribution, $H = h_0 + \varphi x$.

Using the 2D form of integration by parts, we have :

$$\int_{\Omega} -\frac{H}{2} \frac{\partial p}{\partial x} dx dy = - \int_{\partial\Omega} \frac{H}{2} p dy + \int_{\Omega} \frac{1}{2} \frac{\partial H}{\partial x} p dx dy \quad (4.4)$$

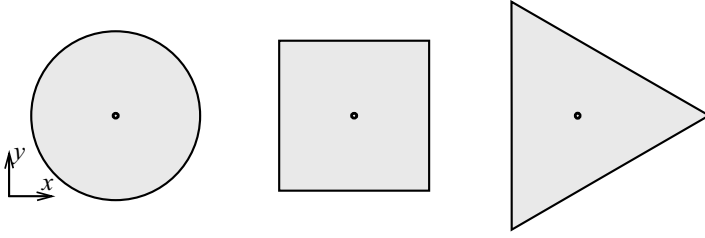


Figure 4.3: Three different actuators, which have a same area $S_a = 10^{-4} \text{ m}^2$, are used in the simulations. Each actuator has one inlet point, located at the centre. The outlet consists of all surrounding edges.

Because $\frac{\partial H}{\partial x}$ is constant for every point in Ω , and from the zero load constraint, the second term of Equation 4.4 can be equated to $\frac{1}{2}\varphi S_a p_a$.

On the boundary $\partial\Omega$ the pressure is constant, the first term of Equation 4.4 can be rewritten

$$\int_{\partial\Omega} \frac{H}{2} p dy = \frac{1}{2} p^- \int_{\partial\Omega} H dy \quad (4.5)$$

Using Green's theorem, we have $\int_{\partial\Omega} H dy = \int_{\Omega} \frac{\partial H}{\partial x} dx dy$, then

$$\int_{\partial\Omega} \frac{H}{2} p dy = \frac{1}{2} p^- \varphi S_a \quad (4.6)$$

Finally, the generated force of this tilting actuator can be calculated:

$$F_x = \frac{1}{2} S_a \varphi (p_a - p^-) \quad (4.7)$$

More general, from the proof, it can be concluded that the force density of a tilting actuator is not dependent on the shape of the actuator, nor on the position of the inlet. It is proportional to the tilting angle and the relative outlet pressure.

$$\bar{F} = \frac{F}{S_a} = \frac{1}{2} \varphi (p_a - p^-) \quad (4.8)$$

Furthermore, more interesting, the resulting force is not dependent even on the pressure distribution. This confirms the observation in Chapter 2 that both the compressible and incompressible model give identical force prediction for a single DoF tilting actuator.

For the flow an analytical solution is complicated to obtain. Instead, using a FEM model, two studies have been conducted in order to observe the effect of the actuator shape. First, the FEM model is used to calculate the force and the flow of three different actuators when the tilting angle φ varies from -4 mrad to 10 mrad. Illustrated in Figure 4.3, these three actuators have different shapes but an identical area, $S_a = 10^{-4} \text{ m}^2$. Each actuator has one inlet point, located at the centre. The outlet is the whole surrounding edge. The chosen tilting direction is about the y -axis that generates a force in x -direction.

The result of this study is shown in Figure 4.4. As it has been found earlier, the force of these three actuators are identical because of the identical area. In contrast, the resulting

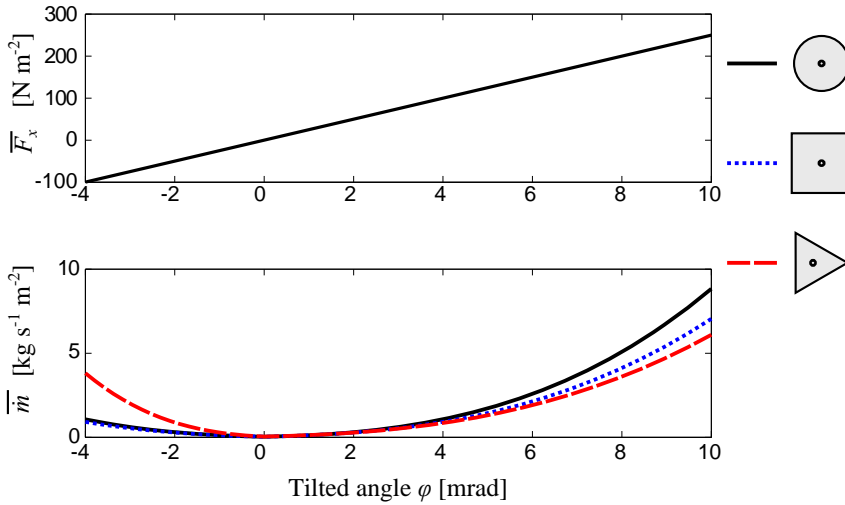


Figure 4.4: The force and flow result of different actuators. The tilting motion generates a force in x -direction. Noted that the flow at zero tilt is non-zero. In this figure, it is too small to be visualised clearly.

flow is dependent on the actuator shape. The required flow for the triangle actuator is smallest in right hand side tilting direction (positive φ) but largest in left hand side direction (negative φ).

In the second study, the FEM model is used to calculate the force and flow of these three actuators when they are tilted in different directions. For each actuator, the study is conducted in two situations: the inlet is located at the centre point and the inlet is shifted towards the edge. The tilting angle in this study is chosen to be 4 mrad.

The required flow is different depending on the shape of the actuator and the tilting direction. Figure 4.5 shows how the flow is affected by the actuator shape, the position of the inlet and the tilting direction. On average, the required flow of the circular shape actuator is smallest. This suggests that it is the best shape for two DoF tilted actuators. In addition, when the inlet location is shifted toward the edge, for some tilting directions (right hand side directions in this simulation) the required flow is smaller compared to the case of central inlet. This confirms the analysis in section 2.3.2 where the optimised inlet location parameter α has been found for single DoF tilted actuators, 0.73. However, this optimum parameter is only useful for a static actuation system where the force is required in only one direction. For two DoF actuators, a movable inlet is required in order to make use of this optimisation. When the actuator is tilted in a direction, moving the inlet to the high side of the actuator can reduce the flow rate while the produced force remains constant. If the inlet cannot be designed to be movable, the centre of the actuator is the best position for the inlet, according to the simulation result.

4.1.2. Effect of inlet and outlet area

From the study presented above, the best shape for two DoF tilted actuators has been found to be the circular shape. In the following analysis, that shape is used for the study

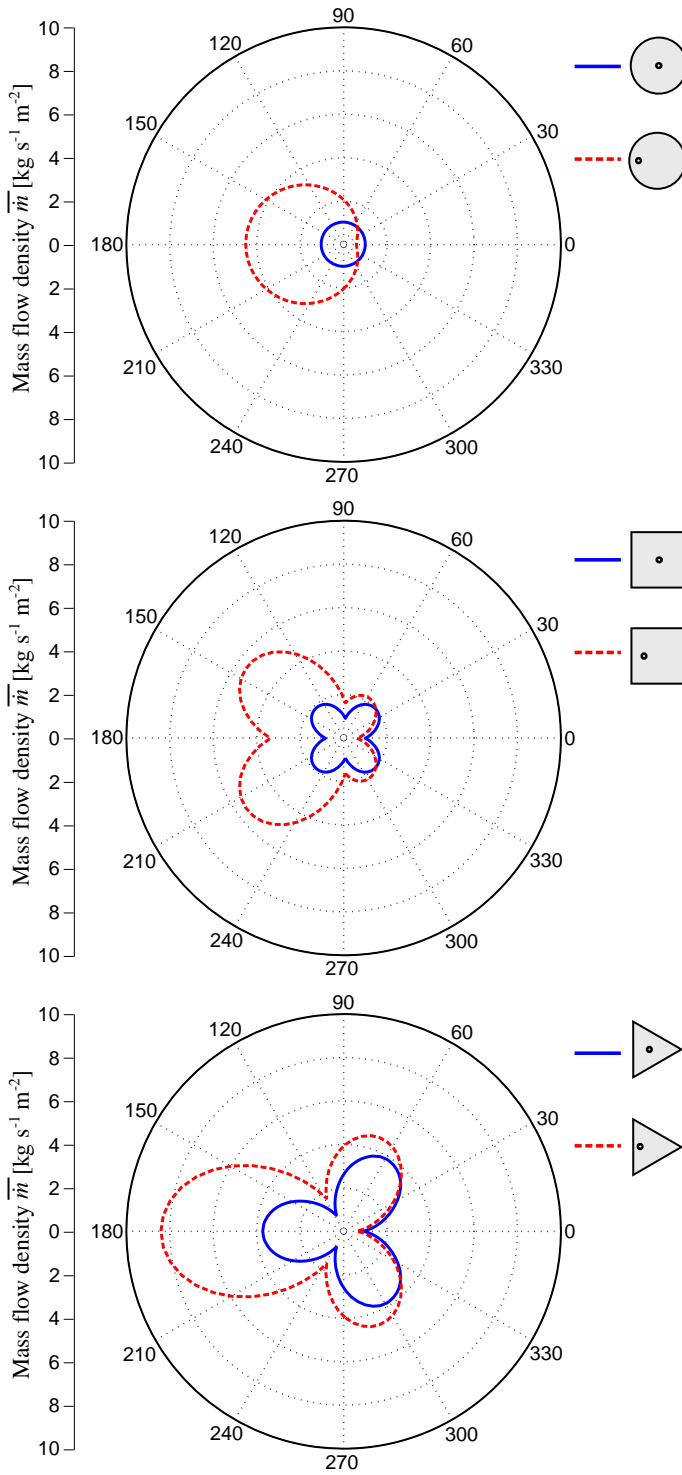


Figure 4.5: The flow result for different tilting directions. Simulation conditions:
 $h = 10 \mu\text{m}$; $p_v = 50 \text{ kPa}$; $\varphi = 4 \text{ mrad}$

on the influence of the inlet and outlet area. The model calculates the force and the flow of actuators that have the same circular shape and the same size, $S_a = 10^{-4} \text{ m}^2$. The difference is the percentage of the area that is used for the inlet and the outlet. The pressure in the outlet area is set to be constant, -50 kPa relative. The inlet pressure is calculated from the load capacity constraint. The chosen tilting angle for this study is 4 mrad. The film height, which is defined as the distance the highest point of the actuator and the substrate, is $10 \mu\text{m}$.

The result of this study is shown in Figure 4.6. The produced force density is not affected by the the inlet and outlet area. This can be proven analytically by extending the mathematical proof presented earlier. In contrast, the flow increases significantly when the area of the inlet and/or the outlet is increased. This can be explained by the reduction of the thin film area and therefore of the flow resistance in the thin film. Indeed, for this type of actuator the viscous traction force is generated by only the thin film flow. A smaller area of the thin film means a smaller active area, resulting a smaller efficiency.

When the inlet area is equal to the outlet area, e.g. 12.5 % or 25 %, the resulting relative inlet pressure is close to the relative outlet pressure (50 kPa in this study). However, when they are both 0%, the inlet pressure needs to be very high in order to carry the substrate since the outlet is a full circle while the inlet is just a singular point. In practice, the outlet/inlet area cannot be zero. For high efficiency the outlet area should be kept as small as possible. The inlet area should be design to be small as well, but the capability of the pressure supply needs to be considered. With a larger inlet area, a smaller supply pressure is required but with a bigger mass flow consumed by the actuator.

4.1.3. Minimise the flow for a required force

The next study presented in this section is to find the operating conditions where the flow is minimised for an arbitrary required force. In the analysis of a single DoF tilted actuator (section 2.3), it has been found that the optimum step height is four times the fly height ($\beta = 5$). The step height is defined as the difference in height between the lowest point and the highest point of the tilted actuator. Similarly for two DoF tilted actuators, the optimum parameter β does exist and will be found in this study. The circular shape actuator with 0 % inlet/outlet area has been chosen for this analysis. The efficiency F/\dot{m} is calculated when the tilting angle φ is kept constant and the actuator diameter is varied. Even though the actuators have different sizes, they produce a same force density due to the fact that the force density is proportional to the tilting angle (Equation 4.8). For a constant φ , the variation of the actuator diameter results in a variation of the step height.

Shown in Figure 4.7 is the performance coefficient result for different tilting angles. It can be observed that the maximum performance coefficient is achieved with different values of the actuator diameter depending on the tilting angle. However, the step heights of these three optimal cases are identical, $42 \mu\text{m}$. This strengthens the optimisation result presented in chapter 2 where the optimal ratio between the step height and the fly height has been found for different types of single DoF contactless actuator. This study has been repeated with different values of the fly height. From the result, it is safe to conclude that for this two DoF tilted actuator, which has circular shape and 0 % inlet/outlet area, 4.2 is the optimal ratio ($\beta = 5.2$).

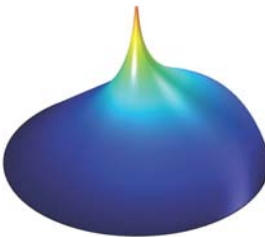
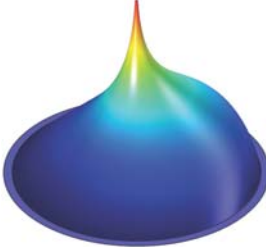
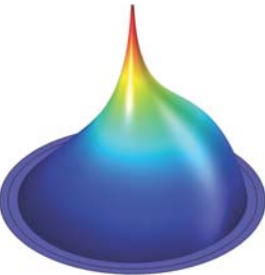
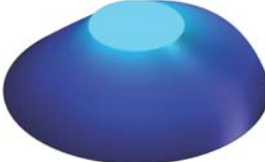
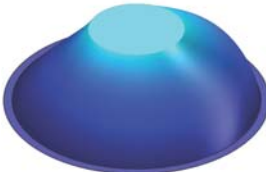
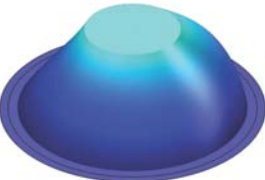



outlet inlet	0% of total area	12.5% of total area	25% of total area
0% of total area	 <p> $p^+ = 280.8$ [kPa] $\overline{F} = 100$ [N m⁻²] $\overline{m} = 1.073$ [kg s⁻¹ m⁻²] </p>	 <p> $p^+ = 305.5$ [kPa] $\overline{F} = 100$ [N m⁻²] $\overline{m} = 1.131$ [kg s⁻¹ m⁻²] </p>	 <p> $p^+ = 338.1$ [kPa] $\overline{F} = 100$ [N m⁻²] $\overline{m} = 1.213$ [kg s⁻¹ m⁻²] </p>
12.5% of total area	 <p> $p^+ = 146.9$ [kPa] $\overline{F} = 100$ [N m⁻²] $\overline{m} = 1.438$ [kg s⁻¹ m⁻²] </p>	 <p> $p^+ = 156.3$ [kPa] $\overline{F} = 100$ [N m⁻²] $\overline{m} = 1.551$ [kg s⁻¹ m⁻²] </p>	 <p> $p^+ = 168.5$ [kPa] $\overline{F} = 100$ [N m⁻²] $\overline{m} = 1.716$ [kg s⁻¹ m⁻²] </p>
25% of total area	 <p> $p^+ = 131.2$ [kPa] $\overline{F} = 100$ [N m⁻²] $\overline{m} = 1.812$ [kg s⁻¹ m⁻²] </p>	 <p> $p^+ = 138.8$ [kPa] $\overline{F} = 100$ [N m⁻²] $\overline{m} = 2.007$ [kg s⁻¹ m⁻²] </p>	 <p> $p^+ = 148.5$ [kPa] $\overline{F} = 100$ [N m⁻²] $\overline{m} = 2.307$ [kg s⁻¹ m⁻²] </p>

Figure 4.6: The result of the pressure distribution, the inlet pressure, the force density and the flow density when the size of the inlet and outlet is varied. Simulation conditions: $h = 10 \mu\text{m}$; $p_v = 50 \text{ kPa}$; $\varphi = 4 \text{ mrad}$

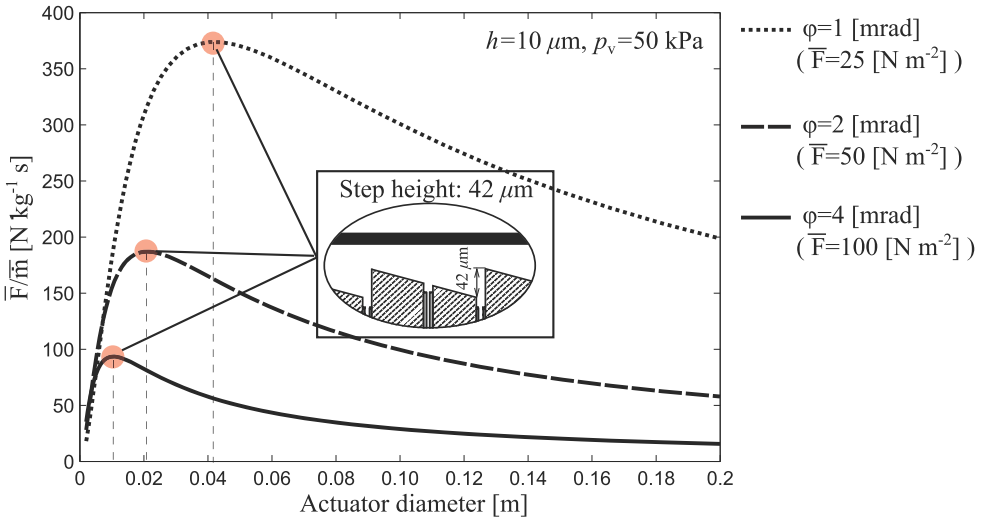


Figure 4.7: Observation on the performance coefficient of tilting actuators when different force density levels are required. The maximum coefficient is achieved with different values of the actuator diameter depending on the tilting angle. However, the step heights of these three optimal cases are identical, 42 μm .

With this optimal ratio, limit curves can be obtained for two DoF tilted actuators. Shown in Figure 4.8 is the limit curve for the fly height $h = 10 \mu\text{m}$. Compared to a single DoF actuator, the air consumption of a two DoF actuator is approximately double if a same force density is demanded. In two DoF actuators, half of the flow, that travels perpendicularly to the tilting direction, does not contribute in creating force. This waste of air happens with all multi DoF concepts discussed previously.

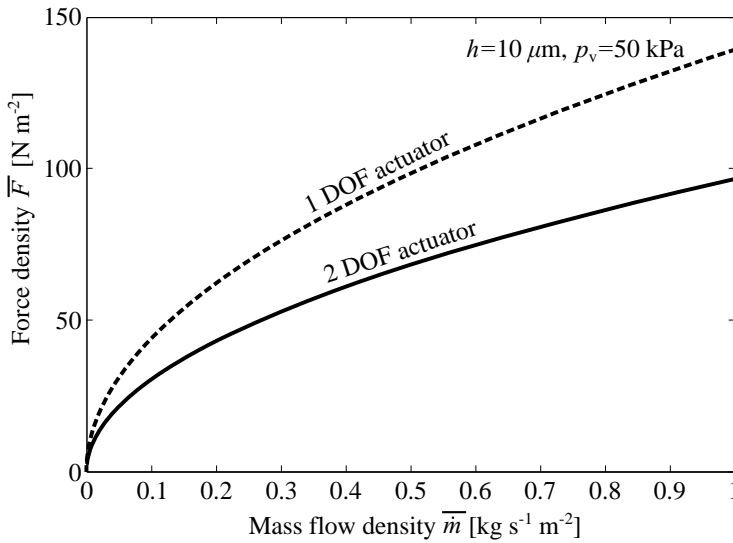


Figure 4.8: A static performance limit curve of two DoF actuators

4.2. Static performance of a three DoF system

This section presents the predicted static performance of a three DoF actuation system that will be described in detail in later chapters, the flowerbed setup. The first goal of the flowerbed setup is to prove that an array constructed from two DoF tilted actuators can manipulate a thin substrate in three planar degrees of freedom. The second goal is to validate the predicted dynamic performance of the tilted actuator concept. Specifications for the force and the flow of this setup are not defined with a specific application in mind. Therefore the dimensions of the actuator array have been chosen mainly for the convenience of the manufacturing process. However, the bearing surface of the flowerbed system has been designed with the knowledge gained from the static performance studies, in order to achieve the highest practical efficiency.

Depicted in Figure 4.9 is the final design of the flowerbed bearing surface. Firstly, the hexagonal shape is chosen for the tilting actuators. When a single actuator is considered, a circular shape actuator with an infinitely small inlet and outlet area gives the best performance regarding to the relation between the achievable force and the flow rate. When they are placed into an array, the outlet area cannot be infinitely small any more because of the unavoidable space between the circular shapes. An alternative that is close the circular shape therefore has been chosen: hexagon. With this shape, the actuators can be arranged with a minimised area of the outlet. Of course, in practice the outlet area cannot be zero because a small gap between actuators is always required for the constructing process.

Secondly, based initial studies using the developed FEM model, the sealing ring, which is the outer ring surrounding the field of tilting actuators that always stays static, has been designed. The function of this ring is to reduce the leaking flow from the envi-

4

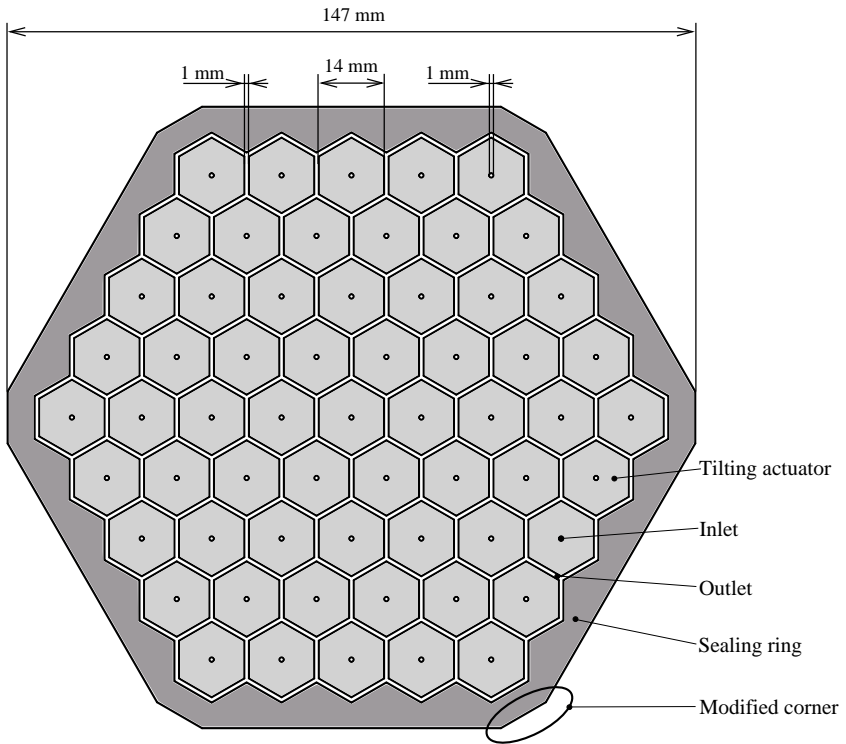


Figure 4.9: The final designed bearing surface of the flowerbed setup

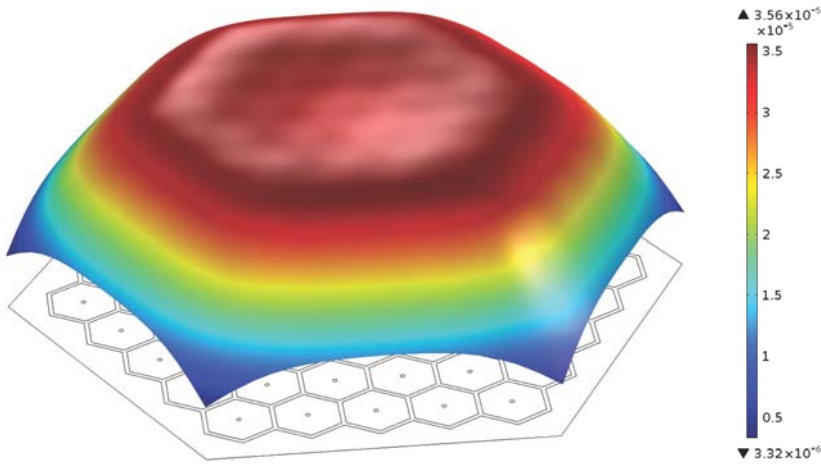


Figure 4.10: An illustrating example of the predicted substrate's deformation. The operating conditions in this simulation are $p_s = 200\text{kPa}$ and $p^- = 90\text{kPa}$ absolute.

ronment (ambient pressure) to the vacuum source. From a substrate deformation study, contact will occur at the edges of the flowerbed particularly at the corners. Therefore the corners have been modified in order to reduce the realisable fly height (for a lower flow rate). Figure 4.10 illustrates an example of the predicted deformation of the substrate when these corners are not modified. The width of the sealing ring is selected resulting from a compromise between reducing the leaking flow and reducing the fly height. A wider sealing ring performs better in preventing the leaking flow but it also requires a bigger fly height in order to avoid contacts caused by the substrate deformation. Narrowing this ring, the sealing function becomes worse but a smaller fly height can be realised.

With the designed bearing surface of the flowerbed, the static performance is described briefly in Table 4.1 for different vacuum pressures, which is the parameter that mostly influences the performance of the system. The required inlet pressure p^+ is calculated based on the carrying load capacity constraint. In practice, the required supply pressure p_s must be higher than p^+ depending on the designed inlet restriction. For this chosen size of the actuator, the optimised tilting angle is 3 mrad. The force and the flow presented in this table are calculated with this optimised tilting angle.

Outlet pressure p^-	(absolute) [kPa]	90	80	70	60	50
Required inlet pressure p^+	(absolute) [kPa]	152	191	223	250	274
Maximum force F	[mN]	133.5	226.3	398.5	529.8	660
Minimum mass flow \dot{m}	[g s ⁻¹]	2.92	5.86	8.74	11.51	14.12

Table 4.1: Predicted static performance of the flowerbed

4.3. Conclusion

In this chapter, an analysis for two DoF tilted actuators has been conducted in order to gain more insight into the concept. It helps in designing the bearing surface of a three degrees of freedom actuation system. The final design of the bearing surface of the flowerbed setup and its predicted performance has been presented. To summarise, some conclusions can be drawn:

- Similar to single DoF actuators, the force generated by a two DoF actuator does not depend on the location of the inlet. It also does not depend on the actuator's shape. It is proportional to the actuator's area, the tilting angle and the relative outlet pressure.
- The flow is dependent on both the actuator's shape and the inlet's location. Also, it is dependent on the amount of the surface area that is taken for the inlet/outlet. A higher flow is required when the area of the inlet/outlet increases.
- According to the result of the study when the actuators are tilted in different directions, it can be concluded that a circular shape actuator with infinitely small inlet/outlet area has the best performance. However, in reality the hexagonal shape should be used because the outlet area can be minimised with this shape with a resulting reduction in flow.
- For two DoF actuators, there is also an optimal ratio between the step height and the fly height that gives the highest efficiency \bar{F}/\bar{m} . With this ratio, performance limit curves can be obtained. These curves are useful in designing a system with desired specifications.
- With the gained knowledge from the static performance studies, the bearing surface of a three degrees of freedom contactless actuation system has been designed.

5

FLOWERBED - DESIGN DECISIONS AND MANUFACTURING

In order to evaluate the performance of the deformable concept in controlling the position of a thin substrate, a three DoF contactless actuation system has been developed, which is named Flowerbed. In this chapter, first the goal of building this setup is described. Then a predictive model is developed for the estimation of dynamics performance. Finally, the design of Flowerbed and its predicted dynamic behaviour is presented.

5.1. Contactless actuation system - Motion control

5.1.1. Limiting factors of motion control performance

In a controlled motion system, the performance in terms of accuracy, precision and frequency response is limited by its subsystems' properties such as the internal dynamic behaviour of the mechanical system, the performance of the sensing system and the behaviour of the actuator (in combination with its amplifier or driver). This thesis focuses on developing a force actuation system that can be used in a controlled motion system in which an object needs to follow a pre-defined trajectory with an ability of rejecting physical disturbances, e.g. vibrations from the environment. For this application, the performance of an actuation system is determined mainly by two factors: the maximum force that can be generated and the dynamic response to an input (command) signal. Of course the output disturbance of the actuation system is also important since it will contribute to the error of the controlled motion. However, it is not in the scope of this investigation.

In order to illustrate how these two limiting factors affect the performance of motion control, the following example is presented. Shown in Figure 5.1, a schematic of a simple mechatronics system, a force actuator is used to drive a floating mass $m = 1$ kg to follow a desired trajectory that is assumed to be sinusoidal with an amplitude $x_p = 10^{-2}$ m. The

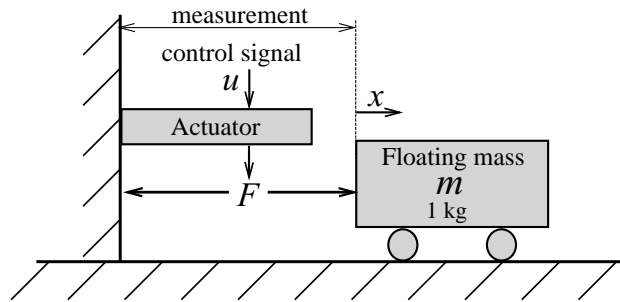


Figure 5.1: Schematic of an illustrative example of controlled motion systems

goal is to make this sinusoidal scanning motion achieve as high frequency as possible. In this example, the distance sensor that is used to measure the position of the body mass is assumed to be ideal (there is no sensing dynamics involved). Two types of actuation systems are compared to be used for this application:

5

Type 1: The force can be produced instantly, but is limited to a maximum value (here 40 N) Theoretically, in this ideal example without other dynamics than the mass, after closing an extremely high gain feedback loop the mass can follow a sinusoidal trajectory up till extremely high frequencies, although not at any amplitude. Due to the fact that the force is maximised, it defines also a maximum acceleration for the given mass. In the example of Figure 5.1 with a maximum force of 40 N with a desired amplitude of the sinusoidal trajectory $x_p = 10^{-2}$ m, the highest frequency that the body mass can follow will be:

$$f_{\text{lim}} = \sqrt{\frac{F_{\text{max}}}{x_p}} \frac{1}{2\pi} = \sqrt{\frac{40}{10^{-2}}} \frac{1}{2\pi} \approx 10 \text{ Hz} \quad (5.1)$$

For trajectories with the same amplitude at a frequency higher than f_{lim} , the required force becomes larger than the maximum of 40 N, and the body mass cannot follow the set point anymore. Even though the position controller has been realised with a high bandwidth, the maximum frequency with which this system can be applied in this application is approximately 10 Hz because of the force limitation. In this situation, the high bandwidth of the controller is beneficial in terms of disturbance rejection as long as the magnitude of the disturbances are small enough (depends on the frequency) that they can be reduced sufficiently by the limited force produced by the actuation system.¹

Type 2: The force is not limited, but the force response is delayed by a certain amount (here 0.01 s) When this type of actuator is used, and if there are stoppers at the two ends, the body mass can move from one side to the other side 100 times in a second, just

¹It should be mentioned here that this difference between small signal bandwidth and large signal frequency limitation is a property of any mechatronic system, however in view of the limited forces of this pneumatic actuation system the frequency limitation is more severe than with many electromagnetic actuators.

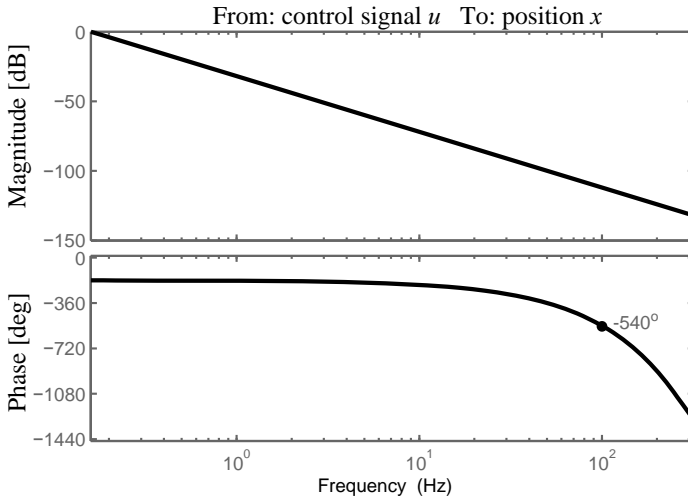


Figure 5.2: Frequency response from the control signal u to the output position x of a system that has a delay of 0.01 s in the force response

because of the delay (the force is assumed to be unlimited). In order to track a sinusoidal reference signal, a controller is required. Shown in Figure 5.2 is the Bode plot of the open loop system from the control signal u to the position x . The delay of the response force causes a phase lag, which is proportional to the frequency. At 100 Hz the phase lag is 360° . Assuming that a PD-feedback controller is used, in order to have a stable close loop system, the controller bandwidth must be realised at a frequency that is much smaller than 100 Hz, e.g. 10 Hz (approximately). Indeed, the theoretical maximum phase lead that can be created by a D-controller is 90° , which is equal to the phase lag at 25 Hz for this delayed system. In other words, for this system it is not possible to realise a stable PD-controller with a bandwidth that is higher than 25 Hz.

Via this example, it is evident that the performance of a controlled motion system is dependent on two properties of the actuation system: the maximum force that can be delivered and the dynamic response of the force. Of these two, the maximum force is important only when the magnitude of the desired trajectory or of the disturbances are specified. Whereas the dynamic response is much more important since it might limit the achievable control bandwidth, resulting in a reduction of the positioning/tracking performance.

5.1.2. Motion control using a contactless actuation system

Very similar to the illustrative example presented above, in the applications of positioning thin substrates, the object, of which the motion needs to be controlled, is a pure floating mass. The thin air film created by the actuation system levitates the substrate and allows it to move freely (zero stiffness in planar degrees of freedom). Of course, there is some viscous damping, however that is negligible for the typical speeds in these systems. Next to this bearing function, a force can be generated and controlled by the actuation

system in order to drive the substrate following a pre-defined trajectory. This force is the integration of the viscous traction of the thin film flow that is the result from the pressure difference between the inlets and outlets. As explained in previous chapters, two different concepts have been introduced to control the force: pressure variation concept and deformable surface concept. The main goal of this chapter is to characterise the dynamics performance of the second concept to observe how it will compare to the first concept, which has been researched in [56].

Since the maximum force that can be delivered by a contactless actuation system has been studied in the static performance analysis, the main focus of the following studies will be on the dynamic response of the created force. Shown in Figure 5.3 is a typical control strategy for the motion of the substrate. The positioning controller gives force commands to the actuation system based on the error of the position. Depending on the requirements on the controlled motion performance, the positioning controller should be realised at a desired bandwidth. As presented in the example above, the realisable bandwidth of this controller is strongly dependent on the dynamic response of the actuation system, especially on the phase lag of the responding force.

5

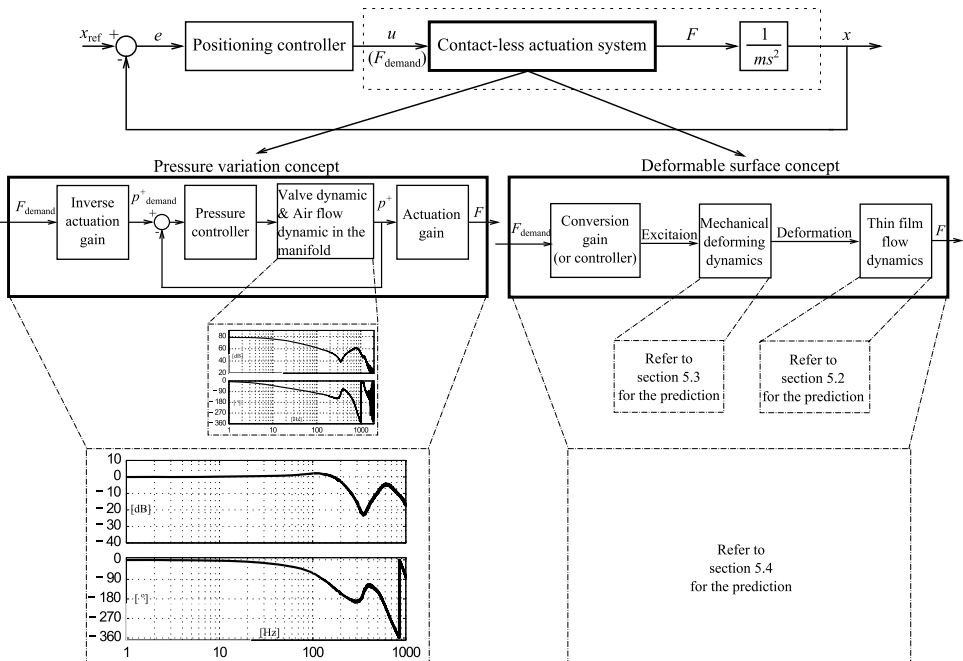


Figure 5.3: A typical control strategy of a positioning system using a contactless actuation system. The positioning controller bandwidth depends strongly on the dynamic response of the actuation system

In the pressure variation concept, when the actuation system receives a force command, air valves are excited correspondingly in order to produce the pressure that is required for the desired force. The frequency response from the valve excitation to the resulted pressure is shown in Figure 5.3. Because of the real pole at approximately 13 Hz, which is the dynamics of filling/exhausting air into/from the cavity of the manifold

through a valve, the phase lag is significantly big even at low frequency. Therefore, an additional pressure control loop has been added. The bandwidth of this pressure controller is limited to about 120 Hz due to the higher order dynamic behaviour of the air flow in the manifold. With the additional pressure controller, the dynamic response from the commanded force to the actual force has been improved. However, the phase lag at 120 Hz is still 90° , resulting in a limitation of the positioning controller bandwidth, approximately at 30 Hz. This experimental result has been obtained with a setup that is build to handle 100-mm diameter wafers. For a larger substrate, a bigger manifold is needed if this concept is used. The positioning bandwidth might be limited to a lower frequency due to the fact that the higher order dynamics of the air flow in the manifold occurs at lower frequency because of the longer channels.

If the deformable surface concept is used, when a force command is given, the actuating elements are excited in order to deform the bearing surface. As it will be presented in later sections, depending on the chosen mechanical structure of the system, the actuating elements can be any types of displacement actuators such as piezo actuators, Lorentz actuators or reluctance actuators. In this concept, the force can be controlled as the result of the change of the pressure distribution that is caused by the varied distribution of the film thickness. As shown in Figure 5.3, the dynamic response of this type of system involves two main components: the dynamic response from the actuating elements to the deformation of the bearing surface (mechanical domain); and the dynamic response from the change of film thickness distribution (deformation) to the traction force (thin film flow domain). In the next sections, these two factors are investigated and the Flowerbed setup is designed with the goal of increasing the dynamics performance of the created force.

5.2. Thin film flow dynamics

In this section, the study on the dynamic behaviour of the thin film flow is presented. A contactless actuator works very similar to externally pressurised air bearings, which have been used widely in precision systems because of their advantages such as low friction, zero wear and long life. In literature, many studies can be found on both static and dynamic behaviour of air bearings. In order to design an air bearing, first the static characteristics should be analysed for the applicability to a specific application, mainly the properties of load capacity, static bearing stiffness and flow rate. An extensive and fairly complete study on steady gas films can be found in [16]. The dynamic behaviour is then analysed in order to complete the bearing design procedure. Indeed, the dynamic stability of an air bearing is known to be an additional limitation when one is designing or optimising an air bearing system for a required set of static characteristics. Usually, in order to increase the static bearing load capacity (for the same supply pressure p_s), a recess is made on the bearing surface as shown Figure 5.4a or a conical shape is used (convergent gap) as shown in Figure 5.4b. For the second case, it has been proven that not only the load capacity but also the static bearing stiffness can be increased, particularly when the gap height is small [47]. However, with the presence of the additional volume in the film due to the modification, the mass inflow might not be equal to the mass outflow at the same time interval because of the compressibility of gas. As a re-

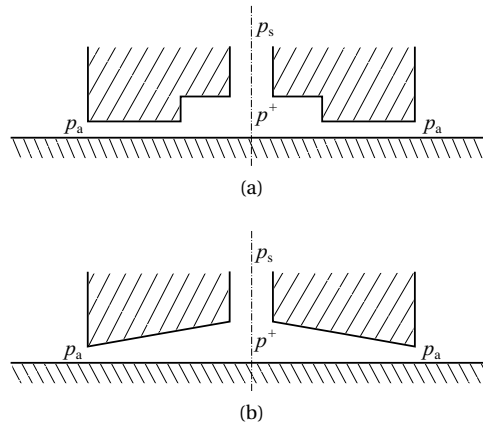


Figure 5.4: The bearing surface is modified in order to increase the static performance

5

sult, under some conditions, energy can be periodically added in phase with the (out of plane) motion of the carried object, thus self-excited vibration develops. The possibility for this instability, which is usually called pneumatic hammer effect to occur seems to increase with increasing effort in enhancing the static performance [47].

In the history of air bearing development, researches on the dynamic behaviour have been conducted focusing mainly on two aspects: to understand the pneumatic hammer phenomenon so that the likelihood of this instability occurring can be predicted; And to be able to predict the behaviour of (self-acting) squeeze films. Following, the study of pneumatic hammer in literature is summarised. It has been an extremely difficult task to establish a stability analysis starting from first principles. In early papers, standard thin film assumptions have been made in order to obtain approximate solutions. The first solutions have been obtained using quasi-static perturbation approach in which the steady state Reynolds equation is used, combined with dynamic mass flow balancing [43, 28]. This method could not find accurate stability criteria but it could give some hints to enhance the stability that has been proven experimentally in [4, 49]. For a better prediction, researchers started using small perturbations to obtain solutions for the time-dependent Reynolds equation [29]. Gradually, also with the time-dependent Reynolds equation, numerical solutions have been obtained also for large amplitude oscillations, for both parallel bearing gaps [48] and convergent bearing gaps [38]. Based on this model, not only the stability criteria of gas bearing can be determined more accurately but also the dynamic behaviour (stiffness) can be improved by means of control, i.e. support control, conicity control or supply pressure control [2]. All studies described above have been conducted with the assumption that inertial forces can be ignored. In literature, research has been published taking into consideration the inertia terms with a modified Reynolds equation. As presented in [22, 55], these models are complicated but can produce more accurate results.

Presented above is just a very brief summary of research in this area. Actually, the dynamic behaviour of externally pressurised air bearings has been studied extensively. Apart from some quantitative discrepancies, they all show a good qualitative agreement

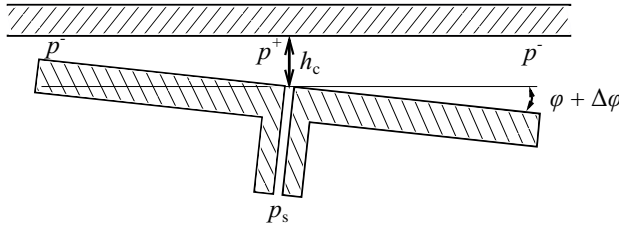


Figure 5.5: Tilt actuator configuration

in the conclusion that the likelihood of the instability occurrence is reduced if the recess volume and the inlet pressure drop ($p_s - p^+$) are minimised. In this thesis, since the requirement of the static load capacity is low because of the small weight of thin substrates, it is not necessary to add a recess on the actuator (bearing) surface. Therefore the instability analysis is less important in designing this type of contactless actuation system. Of course, as discussed in Chapter 4, if one wants to use a smaller supply pressure p_s , a recess can be used with the expense of additional air consumption and increase of instability possibility. This is however not in the scope of this research. Instead, with the absence of recesses, the thin film flow dynamic behaviour study in this thesis focuses on the dynamic response of the planar force created when the film gap is deformed, particularly when the actuator surface is tilted (Figure 5.5).

A study on tilt characteristics of centrally fed air bearings has been reported in [3]. Based on the time dependent Reynolds equation, it investigates the tilt stiffness and damping. In the current analysis, the same approach is applied with the additional step of obtaining the dynamic viscous traction force in order to observe the force response of a tilting actuator. The flow in the bearing gap is assumed to be purely viscous, laminar and isothermal so that the Reynolds equation is applicable. The analysis uses the same actuator geometry described in Chapter 4. It has a circular shape with an area $S_a = 1 \cdot 10^{-4} \text{ m}^2$. The optimised tilting angle is approximately 4 mrad, thus the analysis is limited to ± 4 mrad. Similar to obtaining static solutions, the dynamic force is calculated from the dynamic pressure distribution, which is the solution of the time dependent Reynolds equation:

$$\frac{\partial}{\partial x} \left(-\frac{H^3}{12\mu} \frac{p}{R_g T} \frac{\partial p}{\partial x} \right) + \frac{\partial}{\partial x} \left(-\frac{H^3}{12\mu} \frac{p}{R_g T} \frac{\partial p}{\partial x} \right) + \frac{\partial}{\partial t} \left(\frac{p}{R_g T} H \right) = 0 \quad (5.2)$$

in which H is a function of x and the tilting angle $\varphi(t)$, $H = h_c + \varphi x$. The tilting motion is assumed to be about the central point (inlet) so that the average film thickness is h_c that can be defined as the fly height at the inlet point.

In this study, the supply pressure p_s is kept constant while tilting. The flow is fed to the film from p_s through an inlet restriction that is assumed to be constant. The solved variable is the pressure distribution, including the resulting inlet pressure p^+ . The solution is obtained by three steps. First, using static model, the required supply pressure p_s is calculated for a desired fly height. This step can be done as described in Chapter 3, the Reynolds equation is solved in combination with the zero load condition. Then this result of p_s is used as an input for the second step, calculating the initial states of the

time dependent solution. Finally, numerical solutions are obtained in time domain with the input tilting motion $\varphi(t) = \Delta\varphi \cdot \cos(2\pi f t)$, $\Delta\varphi = 4$ mrad. In this step, the pressure distribution and the average fly height h_c are solved from Equation 5.3, combined with the motion equation of the carried mass

$$m\ddot{h}_c = \int (p - p_a) dA \quad (5.3)$$

in this study, m is chosen to be $0.25 \cdot 10^{-3}$ kg, representing 1 mm thickness glass substrate.

Shown in Figure 5.6 is the result of this study for different frequencies of the tilting motion. The relative vacuum pressure ($p_a - p^-$) is set to 50 kPa. The desired initial average fly height $h_c(0)$ is chosen to be 35 μm , that will result in a minimum film thickness (at the edge, full tilt) of about 10 μm . Observing the force response, at 1000 Hz there appears a small difference compared to the static solution. The difference is more visible at higher frequencies. Showing a "phase-lead" behaviour, it responds slightly in advance to the static solution. This might be explained by the observation that the pressure that is caused by the squeeze film flow creates a force in the direction of the tilting motion. The average fly height, at low frequency, e.g. 100 Hz, 500 Hz, is identical with the static solution where it is just the result of the mass flow balancing with a constant supply pressure. At higher frequencies, it behaves similarly to a mass spring damper system, in which the spring and the damper arise from the air film.

Because the size of the actuator in practice is not much different from the actuator size in this analysis, from this result, it is safe to conclude that the thin film flow dynamics does not have a strong influence in this contactless actuation system. The force can be considered to be able to respond instantly to a tilt motion. To summarise, the box named 'thin film dynamics' in Figure 5.3 can be approximated accurately by a proportional gain for all relevant frequencies. This gain is defined by the area of the actuator surface and the operating relative vacuum pressure ($p_a - p^-$).

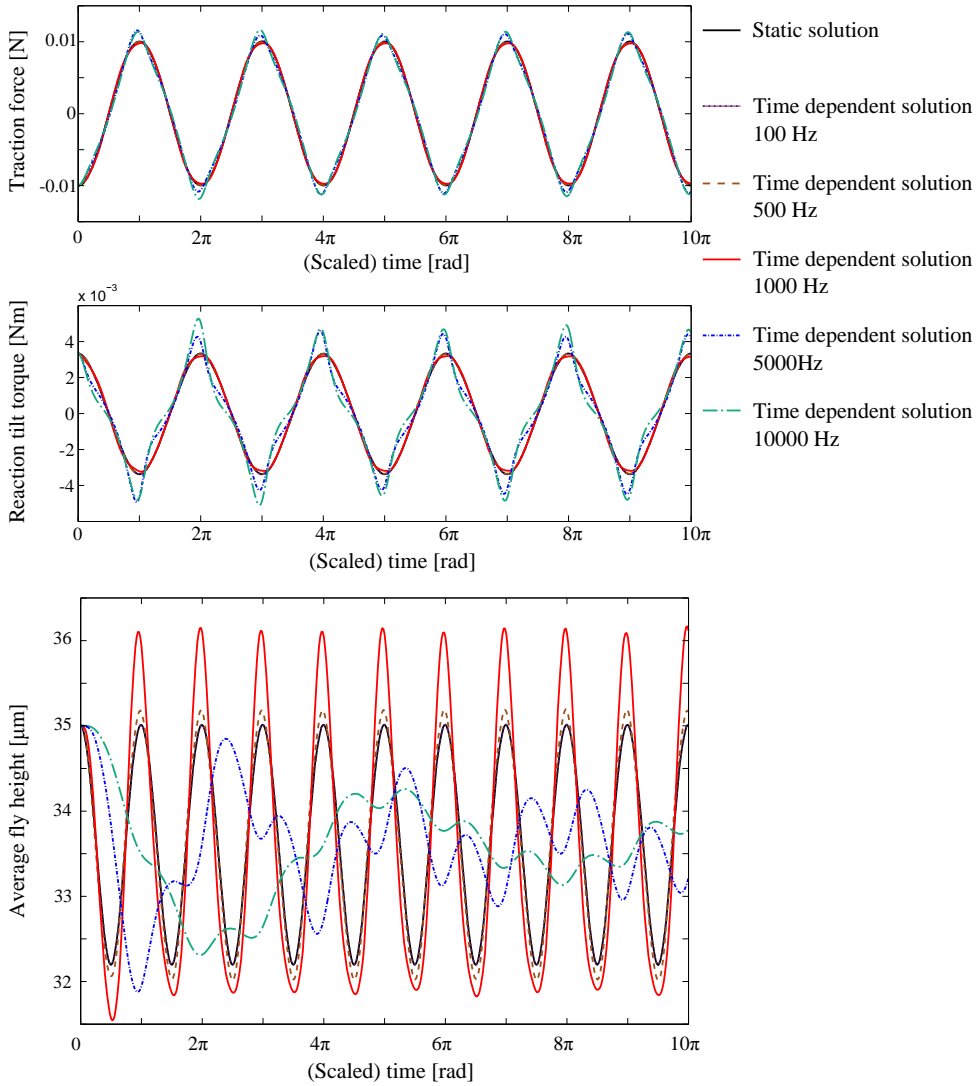


Figure 5.6: Dynamic responses to the a tilt $\varphi(t) = 4 \cdot \cos(2\pi f t)$ mrad of the actuator. The force response shows a very little difference compared to the static solution. This difference is visible at high frequencies only, showing a "phase-lead" behaviour. The fly height behaves similarly to a mass spring damper system. At low frequency it is identical to the static solution, which is just the result of the mass flow balancing when the supply pressure is kept constant.

5.3. Mechanical structure of the flowerbed

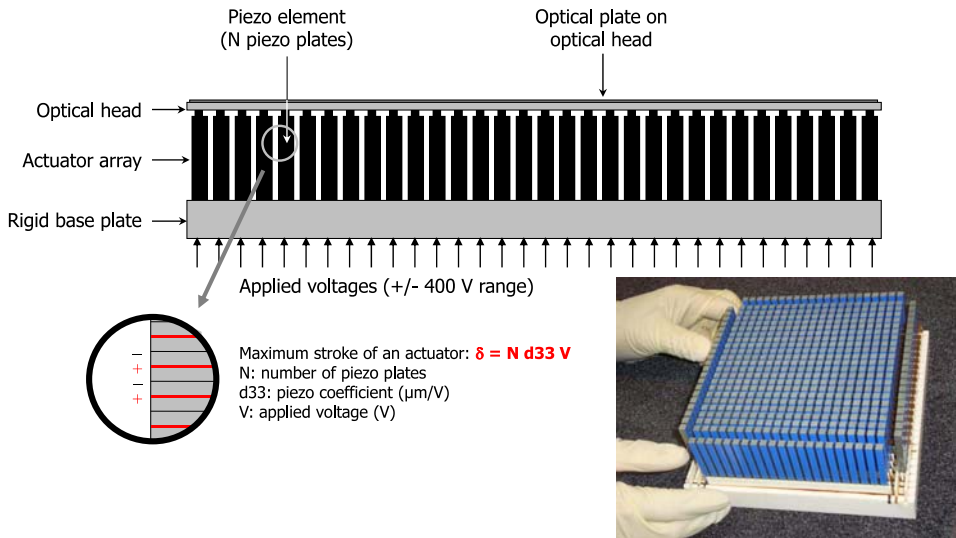
Since it has been analysed that the thin film flow dynamic behaviour can be assumed to be a pure proportional gain up to very high frequencies, the dynamics performance of the whole contactless actuation system depends only on the dynamic response of the deformation, particularly the tilting motion, when a command is sent to the mechanical actuator. From this point onwards, the word "mechanical actuator(s)" is used to refer to the actuating elements that generate the tilting motion of the bearing surfaces, in order to make a clear distinction from the air-based contactless actuators (in short "air actuators") discussed in previous chapters. In this section, first, the chosen mechanism designed to generate the tilting motion is described. Then, the mechanical dynamic behaviour is investigated. Finally, a control algorithm for a positioning application is proposed.

5.3.1. Design decisions

5

In the field of adaptive optics, surfaces that are able to deform actively have been developed for different applications, from large scale in astronomical telescopes to small scale in microscopy, and laser beam shaping applications. At the heart of an adaptive optics system, a controlled deformable mirror is used to compensate for phase errors in a wave front. Different technologies have been developed to fulfil various requirements of adaptive optics systems. Research on this development has been reported in [32]. Starting from introducing the main drivers for the design of different deformable mirrors, it describes in detail the technologies that are available for current manufacturing techniques. In general, a deformable mirror contains an mirror plate that is relatively flexible and an array of actuators that is placed underneath the mirror plate to control its deformation. The main difference between technologies is the type of the actuators that is used to construct the actuating array. Many different types of actuators have been proposed and studied for this purpose. Initially, mainly due to the requirements of mechanical stroke and positioning bandwidth, piezoelectric actuators have been most popular in this application field, both stacked and bimorph bending types. Recently, especially for large deformable mirrors, voice coil actuators have been used. Because of the fast increase in computing power of real time computers, it is possible to have each voice coil actuator controlled by a positioning loop that is fed back with a local distance sensor. High computational power is demanded because the number of actuators in this application is enormous, from hundreds to thousands. More recently, a new generation of deformable mirrors that uses MEMS technologies has been introduced. Similar to other concepts, a thin mirror membrane is attached to an intermediate flexible support. It is actuated by electrostatic or electromagnetic fields generated by an actuator array that is made using MEMS technologies. For an illustration, three examples of deformable mirrors [46, 13, 17] are depicted in Figure 5.7, 5.8 and 5.9.

In the field of adaptive optics, first, the error budget is analysed for different applications. Based on that, the design of a deformable mirror is specified, mainly for four properties: number of actuators, actuator pitch, mechanical stroke and control bandwidth. The number of actuators varies from hundreds to thousands. The actuator pitch,



5

Figure 5.7: A deformable mirror developed based on an array of stacked piezo actuators. The stroke can reach $10 \mu\text{m}$ for 5 mm actuator pitch up to $60 \mu\text{m}$ for 25 mm actuator pitch (source [46])



Figure 5.8: A secondary deformable mirror (1.2 m diameter) developed using 1170 voice coil actuators that have a stroke of $100 \mu\text{m}$ with local positioning control (source [13])

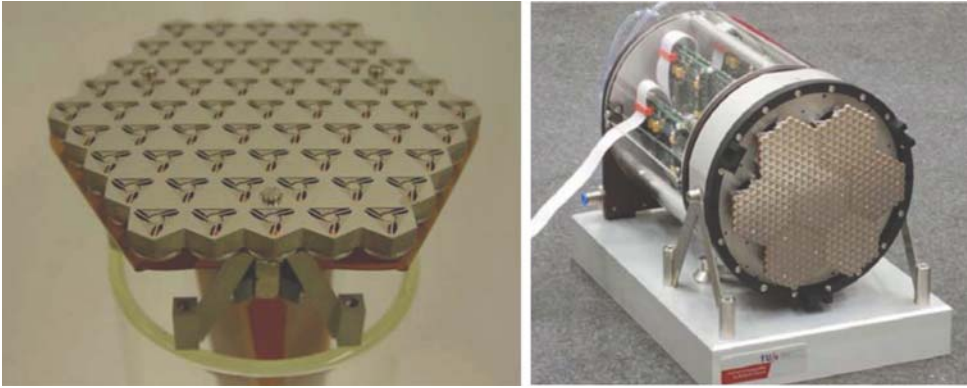


Figure 5.9: A deformable mirror using MEMS like actuators operating on an electromagnetic force principle.

Left: single module consists of 61 actuators. Right: the assembled 150 mm diameter prototype (from 7 modules), without membrane mirror. The stroke is approximately $20\ \mu\text{m}$ with the actuator pitch of 6 mm (source [17])

5

which represents the distance between two actuators in the array, is in the range from 1 mm to 30 mm. The mechanical stroke needs to be from several μm to about $80\ \mu\text{m}$. These requirements are very comparable to the requirements of a deformable surface used in an air-based contactless actuation system. This means that it is possible to apply one of these developed technologies in constructing a deformable surface used in this field, contactless actuation system. However, there are some differences that allow the use of other alternatives. First, the tilting motion of the air actuators is not required to be controlled individually because the total force is the summation of all the forces created by every air actuator. Actually, a more uniform tilting motion results in a better performance due to the fact that the fly height can be smaller, thus the air consumption can be reduced. With the extra expense in cost of using many mechanical actuators, individual control of air actuators might be advantageous, especially in the calibration process where the initial angle of each air actuator is set, e.g. for flattening the global bearing surface of the system. The second difference is the presence of the pneumatic channel system. If an array of mechanical actuators is used, it is a big challenge in realising this pneumatic system in a design space that is reduced by the mechanical actuators' volume. In addition, the large cable bundles, which have already been a very serious practical issue in constructing a deformable mirror, make the pneumatic system design even more challenging. The third difference is caused by the external forces exerted on the deformable surface. Even though the bearing load capacity is small, the pressure distributed on the surface is at a high level because of the requirement of the large pressure difference. This external load makes it a challenge to use MEMS technologies because of the small force that can be created by this type of mechanical actuators. For these reasons, a new concept has been proposed that allows to deform the bearing surface with just a few mechanical actuators. As shown in figure 5.10, when all the air actuators are connected mechanically, for instance by an intermediate plate, any in-plane movements of the intermediate plate will cause the same change in the angle of all air actuators' sur-

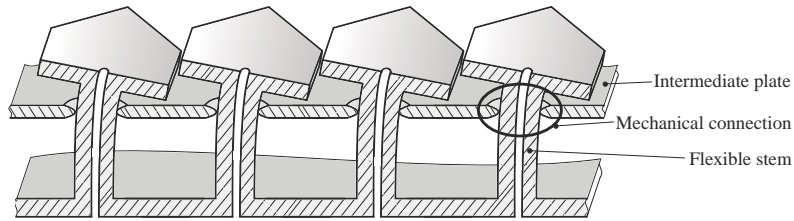


Figure 5.10: A solution to reduce the number of mechanical actuators is to connect the air actuators to an intermediate plate. Any in-plane movements of this plate will cause the same change in the angle of all air actuators' surfaces

faces. Therefore, only three mechanical actuators are required in order to control the position of the intermediate plate, thus the force on the substrate, in three planar degrees of freedom.

Connecting mechanically is the key for reducing the number of mechanical actuators in this application. Connecting with an intermediate plate as shown in Figure 5.10 is just one of many different configurations that have been considered. For instance, the connection can be configured such that the air actuator surfaces will react to an out-of-plane movement or tilting movement of the intermediate object. The configuration in Figure 5.10 has been chosen because the in-plane stiffness of a plate is high so that the energy of the mechanical actuator can be transferred into the motion of the air actuators' surfaces efficiently.

Considering the efficient transfer of energy, answering the question how to connect the intermediate plate to the air actuators is a challenge. Ideally, this connection should be a perfect spherical joint. The high translational stiffness is useful for the motion transmission from the plate to the air actuators. Whereas the low rotational stiffness is beneficial in eliminating the resistance to the tilting motion. Although conventional spherical bearings have been used widely in industry, they are not the option for this application since the operating motion is in the order of tens of μm where the backlash effect will be significant. Therefore, compliant joints are best suited for the connections in this application.

In literature, research has been conducted on compliant joint mechanisms. A spherical compliant joint can be built from some basic blocks of compliant joints, e.g. from three revolute joints or from one universal joint in combination with one revolute joint. Some examples for this type of joints can be found in a recent overview report [31]. In general, they all have a three dimensional structure that is too complicated to be implemented into an array of many joints using a conventional assembly method. However, with additive manufacturing technologies, the possibilities of which are rapidly improving, it might be possible. The challenge will be addressed not only in the functional design of the joint but also in adopting the constraints of this new manufacturing method, for instance its relatively poor accuracy, limited detail size (big wall thickness) and the feasibility of removing support structure (or material). This is a very interesting and challenging topic, but is not in the scope of this research. Instead, the connecting structure has been chosen to be a simple thin membrane, which does not perfectly represents a spherical joint but does have a high in-plane translational stiffness and a

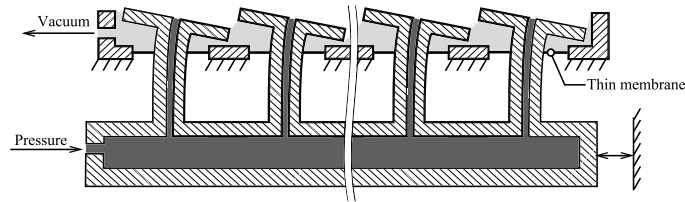


Figure 5.11: Schematic cross view of a flowerbed. A thin membrane has been chosen for the connections between the thick plate and the flexible stem. This membrane does not act perfectly as an ideal spherical joint, but it is sufficient because of its high in-plane translational stiffness and a low out-of-plane rotational stiffness. Furthermore, it is also used as a seal for the vacuum chamber.

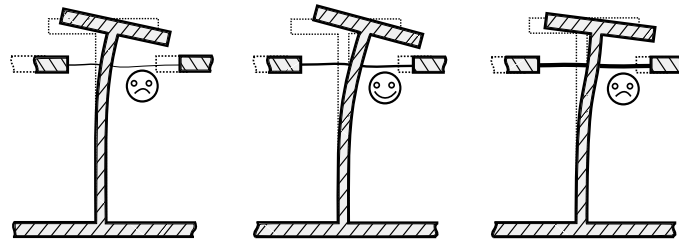


Figure 5.12: The influence of the thickness of the membrane connection. Left: too thin membrane, the displacement of the actuator is smaller than of the intermediate plate. Right: too thick membrane, its high rotational stiffness reduce the tilting angle of the air actuator's surface

5

low out-of-plane rotational stiffness. Furthermore, using a thin membrane for the mechanical connection is not only because of its simple structure but also because of an additional function, the sealing air of a chamber, as presented in the schematic shown in Figure 5.11.

With this design decision, the thickness of the membrane is the first parameter that needs to be examined. As illustrated in Figure 5.12, if the membrane is too thin, as explained previously, a low in-plane stiffness might reduce the efficiency in transferring the plate's motion to the air actuators' motion. On the other hand, if the membrane is too thick, the high rotational stiffness of the membrane reduces the tilting angle of the air actuator's surfaces. This effect, however, is critical only for designs that are made for using additive manufacturing technologies, in which the structure material must be homogeneous and the minimum thickness is limited to 0.5 mm (typical state-of-the-art technology in 2014). For designs made with conventional (assembling) methods, spring steel can be chosen for the membrane and the minimum thickness is available in the order of tens of μm , the effect illustrated in Figure 5.12 can be avoided easily with an appropriate design. Details for the membrane thickness design will be presented later in this section.

The design starts with static calculations concerning the capability of mechanical actuators. The dynamics performance will be checked later in order to modify the design if it is necessary. Two types of mechanical actuators are considered to be used in this setup. The first one is low stiffness force type of actuators such as linear motors or reluctance actuators. The second type is piezoelectric actuator that has high stiffness with a limited

stroke.

Before starting to design the setup, the design space is described, starting with a typical set of specifications. A 200 mm diameter wafer has been chosen to be the carried object for this setup. In order to be fully covered by the substrate, the bearing surface is decided to have 150 mm diameter, resulting in a maximum travelling distance of ± 25 mm. From the study of static performance in Chapter 2 and Chapter 4, the size of each air actuator can be optimised based on a specified desired force or flow. However, because the main goal of this setup is to study the dynamic behaviour of a typical flowerbed actuator, the required static performance is not specified with a specific application in mind. Instead, the size of the air actuator is selected based on convenience for manufacturing. As reasoned in Chapter 4, presenting a study on two DoF tilting air actuators, the most suitable air actuator shape is a hexagon. The distance between two opposite edges of the hexagon is chosen to be 14 mm. For the assembling process, a gap of 1 mm is required between actuators. These chosen dimensions result in an array of 61 tilting actuators arranged in the designated area. The bearing surface of this setup has been presented in Chapter 4, Figure 4.9.

For each actuator, the design space is not so much limited in height, but it is in planar dimensions. It is limited to the region of a hexagon that has 15 mm distance between two opposite edges. The connecting membrane must be designed within this area. In addition, due to the requirement to have an inlet restrictor, the minimum diameter of the flexible stem is assumed to be 3 mm (practical requirement). Therefore, the inner diameter of the membrane cannot be designed to be smaller than 3 mm. From a study on the influence of the ratio between the outer and inner diameter of the membrane, the outer diameter has been chosen to be as big as possible. Indeed, a higher ratio between diameters results in a higher ratio between the in-plane translational stiffness and out-of-plane rotational stiffness. Again, because of practical matters, the outer diameter of the membrane has been reduced from 15 mm (design region) to 13 mm. Finally, as shown in Figure 5.13, the design in planar dimensions is presented.

The next step is to determine the length of the flexible stem, or more accurately the distance between the base and the thin membrane L_s as shown in Figure 5.14. The goal is to achieve the optimal tilting angle of the designed air actuators, 5 mrad. Qualitatively, a longer flexible stem requires a smaller force but a larger stroke of the mechanical actuator and vice versa. In this step, the in-plane translational stiffness of the thin membrane is assumed to be infinitely large so that the displacement of the thick intermediate plate d_p is equal to the displacement of the connecting point of the stem d_s . Next to that, the out-of-plane rotational stiffness is assumed to be zero, so that the effect described in Figure 5.12 does not occur.

If a force type mechanical actuator is used, the relation between the input force and the tilting angle is:

$$\varphi = \frac{F_p L_s^2}{2EI} \quad (5.4)$$

And the required stroke of the mechanical actuator is:

$$d_{p\text{-required}} = \frac{2}{3}\varphi L_s \quad (5.5)$$

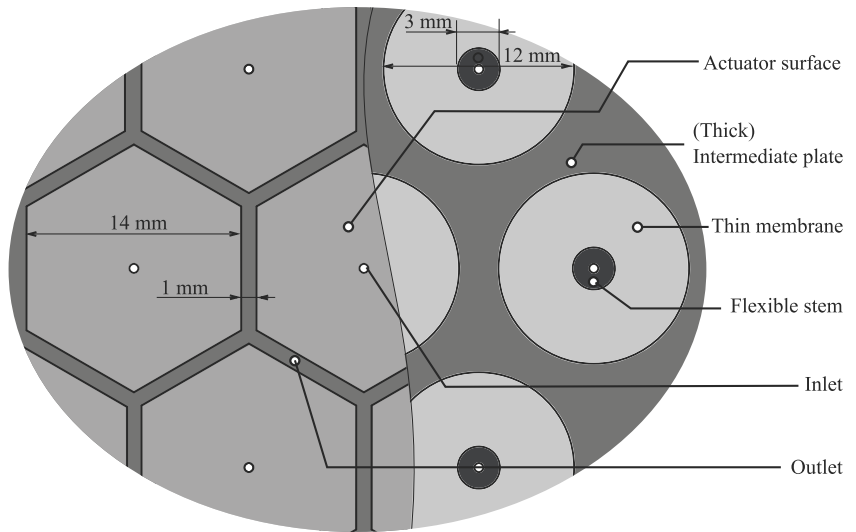


Figure 5.13: Top view of the actuator array design

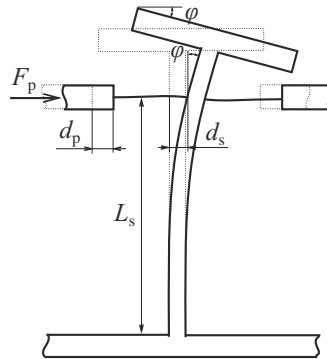


Figure 5.14: For force type actuators: variables description used to calculate the relation between the length of the stem and the input force as well as the required stroke in order to create a desired tilting angle

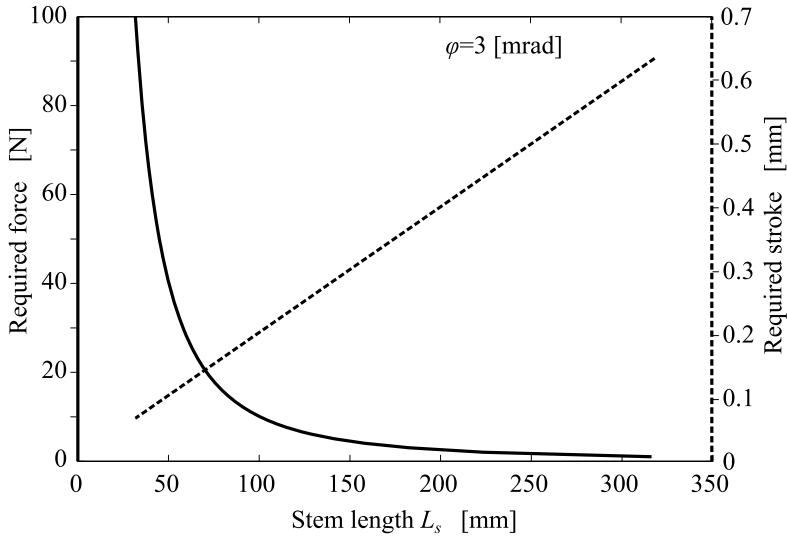


Figure 5.15: A graph that can be used to select a suitable force actuator or a suitable length of the stem for a given force actuator. From this plot: a longer stem requires less force but more stroke from a mechanical actuator.

in which E is the elasticity modulus of the stem material and I is the second moment of area of the stem cross section.

Assuming that aluminium is selected to be the material of the stem and the stem's cross section has 3 mm diameter, using Equation 5.4 and 5.5, a plot can be obtained as shown in Figure 5.15 in order to choose a suitable mechanical actuator for actuating 61 stems that have a given length, or to choose an appropriate length of the stem for a given mechanical force actuator. As expected, a longer stem requires less force and more stroke of the mechanical actuator. Because the design space is not limited in height, it is possible to design a very long flexible stem. However, from the dynamics point of view, a longer stem will result in a worse dynamics performance due to the fact that resonances will occur at lower frequencies.

If a displacement type actuator (piezo) is used, the calculation can be performed with an equivalent schematic shown in Figure 5.16a, and Figure 5.16b if a mechanical amplifier, e.g a lever, is used to increase the mechanical stroke. A piezo can be modelled as an ideal (infinitely stiff) displacement actuator that generates a displacement d_a through a spring with a finite stiffness k_a , in order to make a movement d_p of the intermediate plate. The maximum value of d_a is described as the stroke of the piezo, whereas k_a is the stiffness described in the specification sheet of the piezo actuator. In Figure 5.16, the spring k_s represents the stiffness of the bending structure of the stem, $k_s = \frac{3EI}{L_s^3}$. When a voltage difference is applied between two electrodes of the piezo actuator, the resulting d_a , which is proportional to the voltage difference, will create a movement of the intermediate plate d_p that can be calculated:

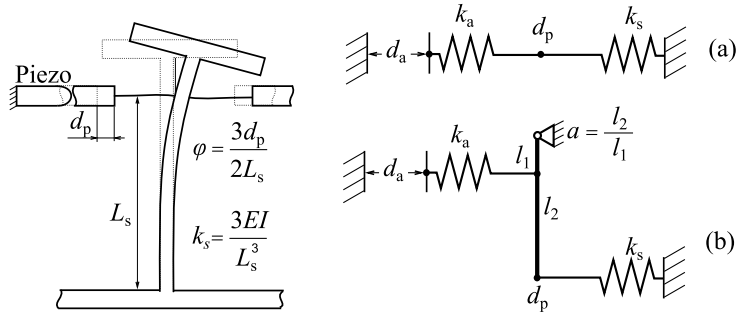


Figure 5.16: A schematic for the calculation when a piezo type mechanical actuator is used: without a mechanical amplifier (a), and with a mechanical amplifier that has an amplifying ratio $a = \frac{l_2}{l_1}$ (b)

$$d_p = a \frac{k_a}{(k_a + a^2 k_s)} d_a \quad (5.6)$$

in which a is the amplifying ratio, and the lever is assumed to be infinitely stiff. The tilting angle φ will be:

$$\varphi = \frac{3d_p}{2L_s} \quad (5.7)$$

For an illustration, a commercial piezo, identified as P-888.91, is assumed to be used. It is the biggest piezo of the most cost effective series of stacked piezo actuators from PI, and has dimensions of 10 mm x 10 mm x 36 mm. The stroke and the stiffness of this piezo are $\pm 18 \mu\text{m}$ and $100 \cdot 10^6 \text{ Nm}^{-1}$ respectively. Using the equations described above, the maximum tilting angle can be calculated for various lengths L_s with different amplifying ratios a . The result is presented in Figure 5.17. For small values of L_s , the stiffness k_s is high, resulting in a small displacement of the intermediate plate d_p . For large values of L_s , d_p approaches d_a because of the small stiffness k_s , however, the tilting angle φ is small due to the fact that the piezo stroke d_a is limited. For each selected amplifying ratio, there is an optimal length of the stem that can create the largest tilting angle. However, the result shows that very high amplifying ratio and long stem length are required in order to achieve the desired tilting angle of 3 mrad.

From the initial calculations, considering both types of actuators, the appropriate range for the length of the stems is from 20 mm to 50 mm, with a structure stiffness k_s from $0.02 \cdot 10^6 \text{ Nm}^{-1}$ to $0.35 \cdot 10^6 \text{ Nm}^{-1}$. These values of the stiffness make the selection of membrane thickness very easy. For instance, if the membrane is made of spring steel and has dimensions described previously (3 mm inner diameter, 13 mm outer diameter), with a thickness of $50 \mu\text{m}$ the in-plane translation stiffness is $28 \cdot 10^6 \text{ Nm}^{-1}$, much higher than k_s . Whereas the out-of-plane rotational stiffness is very small, 0.78 Nm rad^{-1} . These stiffness values have been obtained by a numerical calculation, using a commercial FEM package. For the membrane thickness in the range from $50 \mu\text{m}$ to $100 \mu\text{m}$, the results do not change significantly if the calculations include the actual stiffness of the membrane,

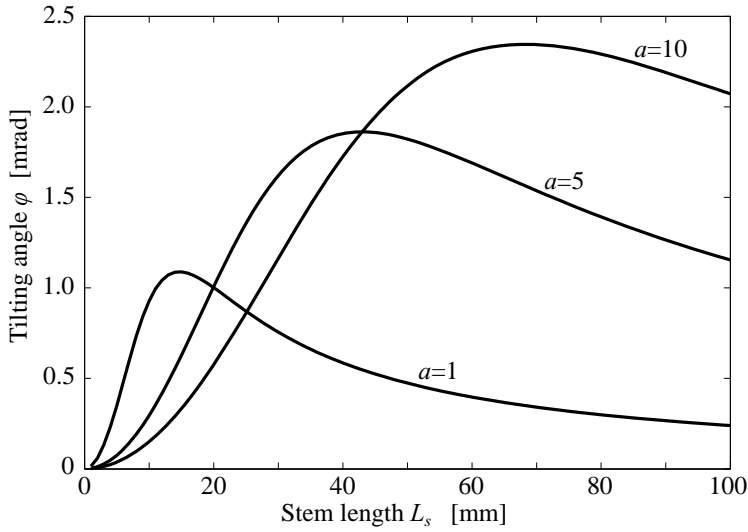


Figure 5.17: Assuming a piezo that has a stroke of $\pm 18 \mu\text{m}$ and a stiffness of $100 \cdot 10^6 \text{ N m}^{-1}$ is used, the tilting angle ϕ is calculated for various lengths L_s with different amplifying ratios a . For very small values of L_s , the stiffness k_s is high, resulting in almost no displacement of the intermediate plate d_p . For very large values of L_s , d_p approaches ad_a , but the tilting angle ϕ is small because of the limited stroke d_a , and $\phi = \frac{3d_p}{2L_s}$

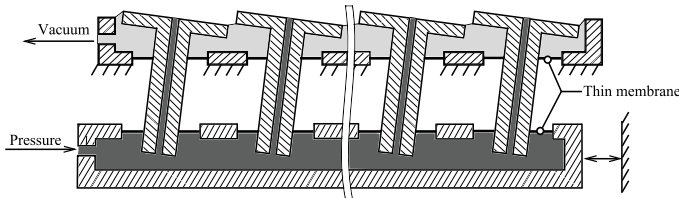


Figure 5.18: The configuration with two membranes can be used in order to reduce the required force for tilting the air actuator surfaces

instead of assuming an infinite in-plane translation stiffness and a zero out-of-plane rotational stiffness.

Compared to the in-plane stiffness of the membrane, the stiffness k_s of the bending stem is small. However, it is the main factor that complicates the selection of an appropriate actuator. Therefore, as shown in Figure 5.18, another design has been proposed that reduces the required force for tilting 61 air actuator surfaces. In this design, the resulting tilt of the air actuator surfaces is not the result of the bending motion of the stems but of the two membranes. Because the out-of-plane rotational stiffness of the membrane is very small, the force required to produce displacement of the intermediate plate is small:

$$d_p = \frac{F_p L_s^2}{(\kappa_{o_1} + \kappa_{o_2})} \tag{5.8}$$

in which $\kappa_{o,1}$ and $\kappa_{o,2}$ are the out-of-plane rotational stiffness of the top and bottom membranes respectively. The tilting angle in this configuration will be:

$$\varphi = \frac{d_p}{L_s} \quad (5.9)$$

Similar to the investigation of the relation between the stem length L_s and the mechanical actuator in the bending configuration presented earlier, Equation 5.8 and 5.9 can be used to analyse this configuration, using two membranes. The result shows that it is easier to choose a mechanical actuator in this configuration, for both types of actuator. If piezo actuators are used, because of their high stiffness, the stem length L_s can be designed from 3 mm to 5 mm for the optimal tilting angle without an additional mechanical amplifier. If force type actuators are used, L_s is fairly easy to choose, depending on the actuator capability. For a reasonable range of the force requirement from 15 N to 30 N, L_s is advised to be chosen in the range from 10 mm to 20 mm.

Clearly, the connecting membrane does not represent a perfect spherical joint. First, the in-plane rotational stiffness of the membrane is very high. This high stiffness causes troubles for the mechanical actuators to rotate the intermediate plate when a torque is required on the substrate. In order to solve this problem, holes have been added in the lower membranes, resulting a structure similar to the spoke structure of a bike wheel. However, this modification does not solve the problem completely because it also reduces the in-plane translation stiffness that is required to be high. The second imperfection of using a thin membrane to connect the stem and the intermediate plate is that the out-of-plane translational stiffness is small. If the bending stem configuration is used, this low out-of-plane stiffness is not a problem. It might be a problem for the two membrane configuration. However, because the bearing stiffness of the thin air film is very high, the influence of this low out-of-plane stiffness of the membrane is expected to be negligible. Balancing automatically, the bearing stiffness of the air film will prevent contact between the substrate and the system, ensure that the substrate can float freely on top of the actuation system. Also, because of the low out-of-plane stiffness of the flowers and the high air film stiffness, any height variation in the flowers will be compensated in axial displacement of the flowers. Furthermore, since the out-of-plane positioning is not in the scope of this research, the two membrane configuration has been chosen for Flowerbed where the in-plane studies can be performed without much effort in searching for suitable mechanical actuators. To summarise, the design decisions made for Flowerbed is described in Table 5.1

5

5.3.2. Flowerbed construction

With the design decisions described above, Flowerbed can be constructed. Shown in Figure 5.19 is the construction of a single "flower". Each of these consists of five parts: an actuator head, an inlet tube and three spacers. The two thin membranes are clamped between three spacers by fastening an M3 bolt at the end of the inlet tube. At the outer edges of the membranes, they are clamped between two thick plates, both for the top and the bottom one. In order to reduce the in-plane rotational stiffness, six holes have been made in the bottom membrane. The top membrane is not perforated because it has an additional function, sealing the vacuum chamber.

Property	Decision
Design	
Carried substrate	200 mm diameter wafer
Number of air actuators	61
Air actuator surface	14 mm hexagon
Connecting configuration	Two membranes (Figure 5.18)
Stem length L_s	13 mm ⁽¹⁾
Stem diameter (inner diameter of membranes)	5 mm ⁽²⁾
Membrane outer diameter	13 mm
Membrane material	Spring steel
Membrane thickness	50 μm
Actuation requirements (static) ⁽³⁾	
Force	14.6 N
Translational stroke	39 μm
Torque	2.4 Nm
Rotational stroke	0.65 mrad

Table 5.1: Design decisions made for Flowerbed

- (1) This length has been chosen for being able to use both types of actuators (force type and displacement type)
- (2) Since the flexibility of the stem is not important in the two membrane configuration, this diameter is increased slightly in order to make it easier for manufacturing
- (3) The requirements for the static optimal tilting angle, 3 mrad

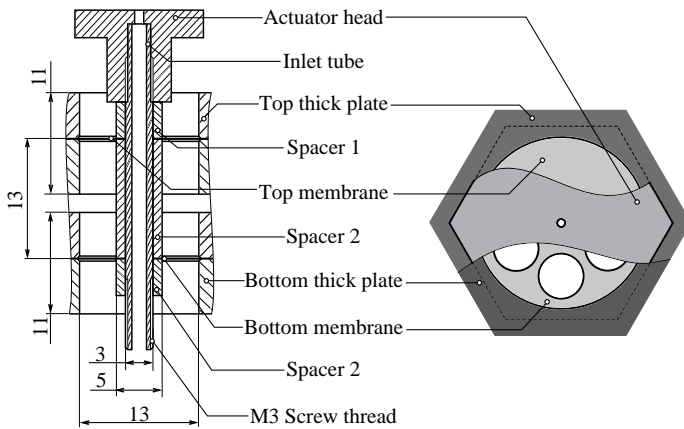


Figure 5.19: The construction of an actuator.

The final constructed Flowerbed is presented in Figure 5.20. It is the result of the construction procedure of following steps:

- The top membrane is clamped between two thick plates by screws. Then, this plate is attached with the top part that contains the sealing ring and the vacuum supply port.

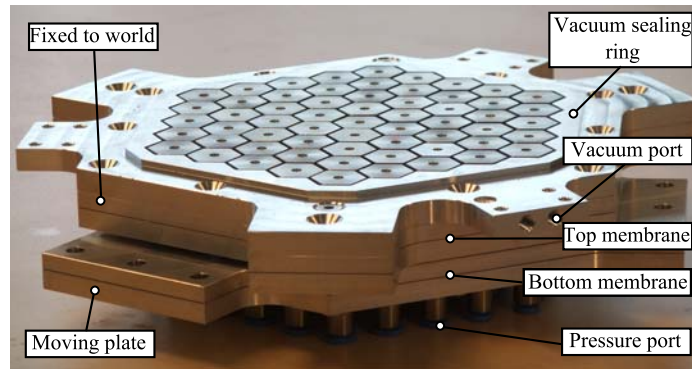


Figure 5.20: The constructed flowerbed.

5

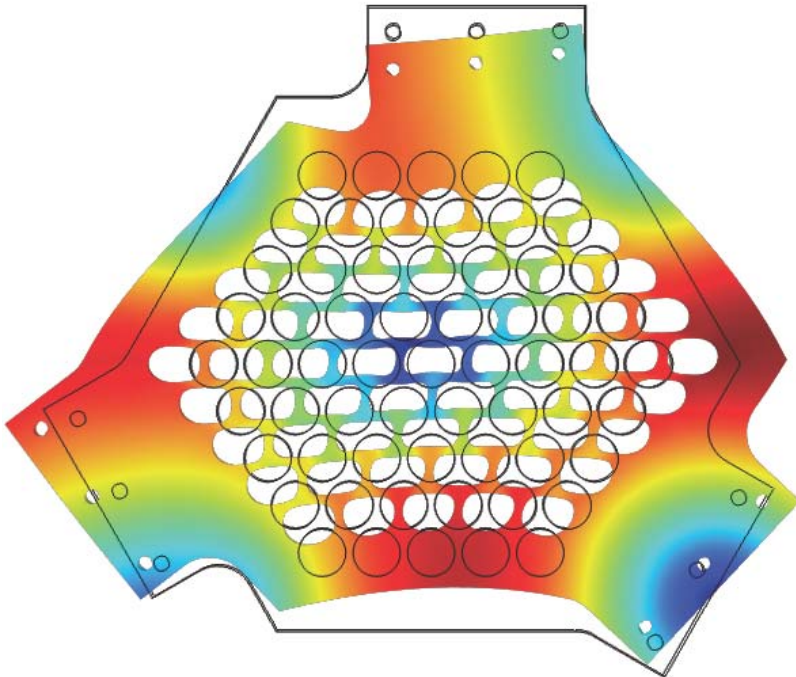
- Similarly, the bottom membrane is also clamped between two plates. Positioning pins have been added in the design such that all the plates are in the right position while clamping.
- All 61 actuator heads with inserted inlet tubes are placed on a reference plate that keeps the actuator heads in the correct orientation and distance.
- The first spacers are inserted into the inlet tubes. Followings are the top plate (result of step 1), second spacers, the bottom plate (result of step 2) and the third spacers.
- Finally, 61 air connectors (pressure ports), which have M3 female thread, are fastened at the end of the inlet tubes using an adjustable limiting torque screw driver. This special screw driver has been used in order to assure an identical fastening torque applied on every actuator.

5.3.3. Mechanical dynamics

The structure of Flowerbed is too complex to efficiently perform a mechanical dynamics analysis of the full structure. Therefore this has been performed based on the study of the dynamic behaviour of a single "flower". In order to do this, the thick intermediate plate has been assumed to be a rigid body. First, an eigen frequency study has been performed for this thick plate using a FEM model, in order to determine the range of frequencies that the rigid body assumption is valid.

Shown in Figure 5.21 is the thick intermediate plate and its first in-plane mode shape, at the frequency of 4910 Hz. This result indicates that the thick intermediate plate can be considered to be rigid up till 4910 Hz.

The dynamic behaviour of a single "flower" is then analysed using a FEM model. Assuming that the edge of the top membrane is fixed, presented in Figure 5.22 is the frequency response of the tilting angle φ when a translational motion d_p is applied to the edge of the bottom membrane, which is assumed to be rigid. From the result, the tilting angle can be considered to be proportional to the displacement of the edge of the



5

Figure 5.21: The thick intermediate plate and its first in-plane mode shape (4910 Hz).

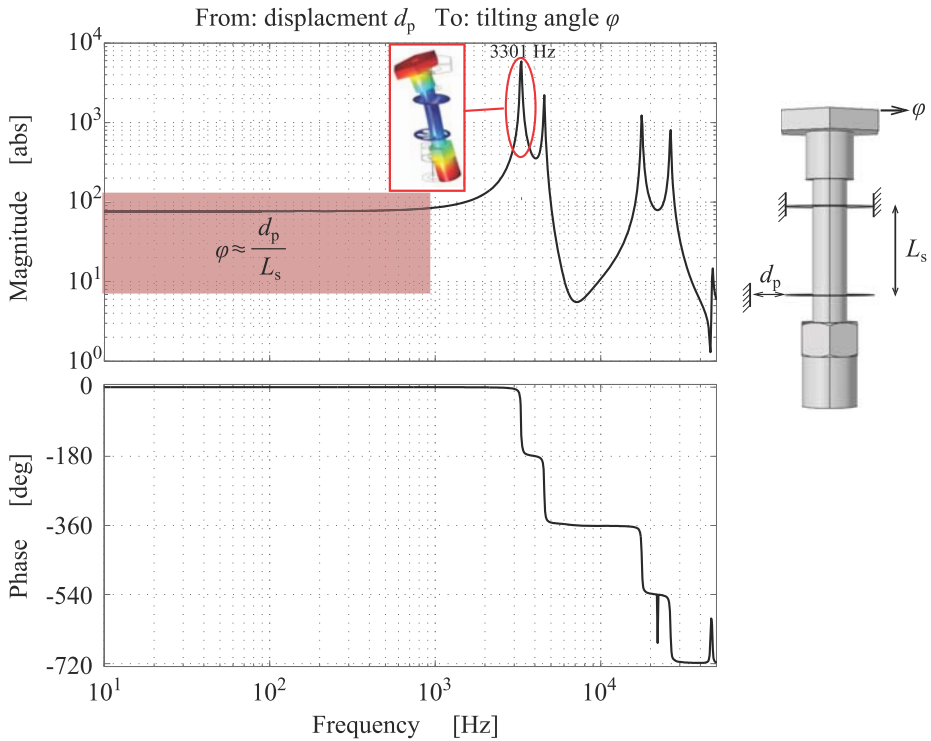


Figure 5.22: The transmissibility response from the displacement of the edge of the bottom membrane d_p to the flower tilting angle φ . From the result it can be observed that at 3300 Hz the tilt is decoupled from the displacement d_p because of the strain of the bottom membrane. In this analysis, the edge of the top membrane is fixed and the edge of the bottom membrane is assumed to be rigid.

membrane up till about 1000 Hz. At 3300 Hz, the tilt is decoupled from the displacement d_p because of the strain of the bottom membrane.

Considering the performance of the full system's dynamics, when a translational motion is applied to the thick movable plate, all the edges of the bottom membranes can be considered to have an identical translational displacement because of the rigid body assumption (up to 4910 Hz). Therefore the tilting angle of the flowers responding to a translational motion of the thick plate is similar to the behaviour of a single flower, limited at 3300 Hz. On the other hand, a rotational motion applied on the thick movable plate will result in both rotational and translational motion of the edges of the bottom membranes. The rotation of these edges are identical but the translational motion is dependent on the position of each flower as presented in Figure 5.23. From the study in Chapter 4, where it has been stated that the generated force of a tilting air actuator is not dependent on either the actuator shape or the inlet position, the in-plane rotational motion therefore does not influence the output force. Only the translational motion of the edges of the membranes, which cause the tilt of the air actuator surfaces, does generate force. Responding to a rotational movement of the thick plate, even though the resulting tilting magnitude is different for every air actuator surface, the average effect is still

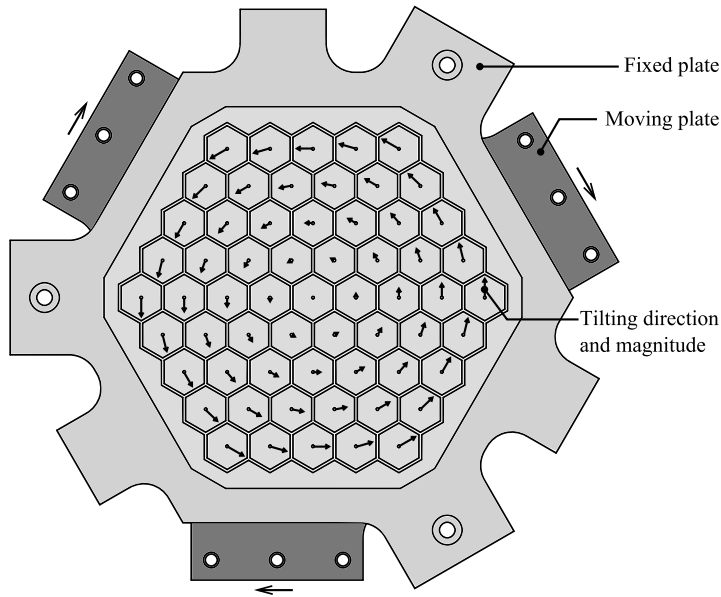


Figure 5.23: An illustration of the tilt of each actuator surface responding to a rotational movement of the thick movable plate. Even though the resulting tilting magnitude is different, the average effect is still represented well by the dynamic behaviour of a single flower described earlier because the tilt is the result of only the translational movement of the (circular) edge of the membrane of each flower.

represented well by the dynamic behaviour of a single flower described earlier.

From the studies above, it can be concluded that 3300 Hz is the first theoretical limitation of this mechanical structure in controlling the tilting angle of the air actuators by varying the position of the thick movable plate. The overall mechanical dynamics performance depends also on how well the position of the thick plate responds to a command. If the movable plate positioning control bandwidth is higher than 3300 Hz, the overall mechanical limitation bandwidth will be 3300 Hz. If this is not the case, the performance of the movable plate positioning control determines the overall performance.

The mechanical actuator used to control the position of the movable plate can be either force type actuator or displacement (piezo) type actuator. If a force actuator is used, the open loop frequency responses from the mechanical actuation force to the movable plate position needs to be analysed in order to estimate the achievable bandwidth of this positioning controller. The result of this open loop frequency response is shown in Figure 5.24 (translational motion of the plate). As expected, at low frequency band, it behaves similar to a mass spring system with a resonance at about 50 Hz. Higher order dynamic behaviour starts to occur at around 3000 Hz, using a rule of thumb, the bandwidth of a closed loop controller can be realised at 1000 Hz approximately. It should be noted that this estimation only describes the limitation due to the mechanical structure itself. In reality, the positioning controller of the movable plate is also influenced by other factors such as the dynamic behaviour of the driver (amplifier), the dynamic behaviour of the position sensor as well as the location of actuation and sensing (collocated and

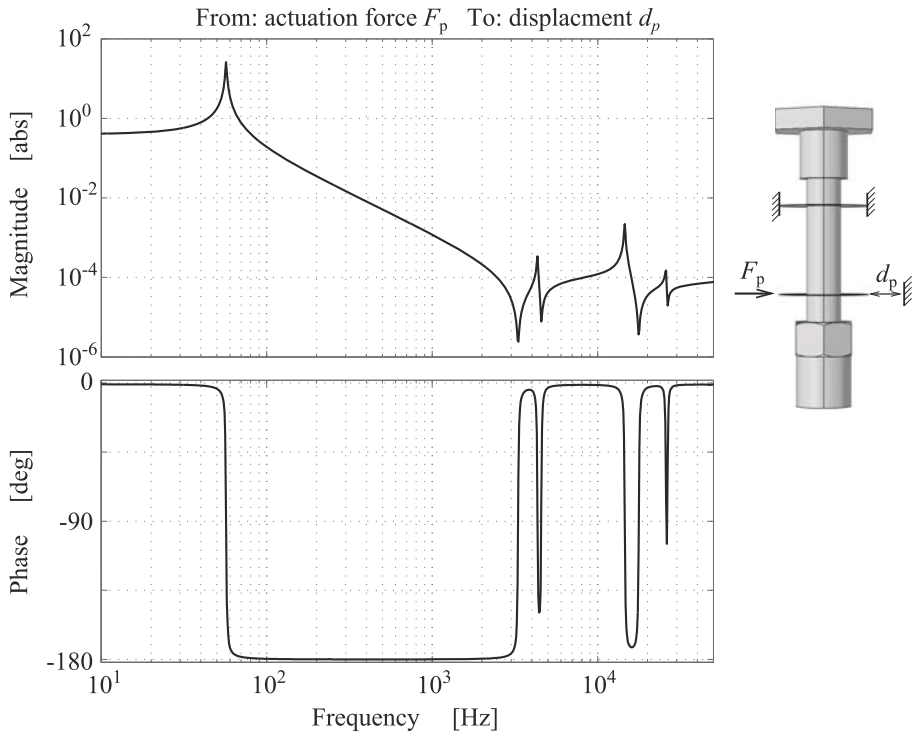


Figure 5.24: The frequency response of the open loop system when a force type actuator is used. Higher order dynamic behaviour starts to occur at around 3000 Hz, a closed loop controller for the position of the movable plate can be realised with a bandwidth of 1000 Hz approximately, using a rule of thumb.

non-collocated problem).

If a displacement type actuator is used, similar to the static study presented earlier, the actuator can be modeled as an ideal displacement source generating a displacement d_a , and transfer this motion to the movable plate through a spring with a finite stiffness k_a . Because the actuator stiffness k_a is relatively high, a closed loop controller is not necessary for this case. If an open loop controller is used, the bandwidth can be determined by the actuator stiffness and the equivalent mass of the moving body (mass of the plate and inertia of flowers). For example, if the actuator stiffness is $100 \cdot 10^6 \text{ N m}^{-1}$, which is achievable with a piezo, the first resonance frequency is estimated to be 2000 Hz.

5.4. Predicted overall dynamics performance

To summarise, from the studies on the thin film flow dynamics and the mechanical dynamics, the overall performance of Flowerbed's dynamics can be predicted and is presented in Figure 5.25. When a force command is received, it can be converted to the required position of the movable plate. The actual response of the plate position is dependent on the type of the mechanical actuators that is used in the system. Described

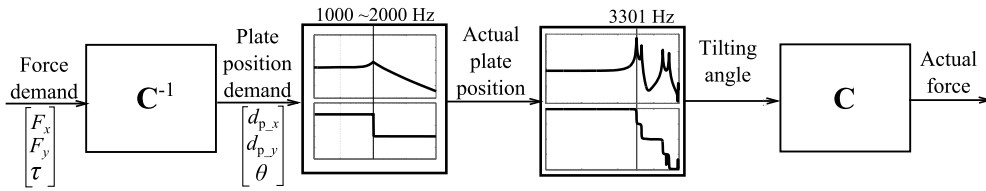


Figure 5.25: Overall performance of Flowerbed's dynamics

in this figure, the range of 1000 Hz to 2000 Hz is a typically achievable bandwidth for this positioning controller. In reality this range is much wider. For an example, if a force type mechanical actuator is used with a closed loop controller, the bandwidth might be limited at a lower frequency because of other factors such as the dynamic behaviour of the driver and/or the position sensor. On the other hand, this bandwidth might be realised at a higher frequency than 2000 Hz with a stiffer (bigger) piezo actuator.

In the case that the plate position controller can be realised with an extremely high bandwidth. The dynamics performance is still limited by the mechanical structure itself. According to the model, the tilting angle can "follow" the position of the movable plate up till maximum 3300 Hz. After this frequency the tilting motion of the air actuator is decoupled from the movement of the movable plate.

Finally, from the thin film dynamics study, the output force can be considered to respond instantly to the tilting motion of the actuator surface. Thus a proportional gain can be used to represent the thin film flow dynamic. In the diagram in Figure 5.25, the constant matrices C and C^{-1} describe the relation between the position of the movable plate and the output force:

$$\begin{bmatrix} F_x \\ F_y \\ \tau \end{bmatrix} = C \begin{bmatrix} d_x \\ d_y \\ \theta \end{bmatrix}, \quad C = (p_a - p_v) \frac{S_a}{2} \frac{1}{L_s} \begin{bmatrix} 61 & 0 & 0 \\ 0 & 61 & 0 \\ 0 & 0 & \sum_{i=1}^{61} r_i^2 \end{bmatrix} \quad (5.10)$$

in which $(p_a - p_v)$ is the operating relative vacuum pressure, S_a is the area of an air actuator, L_s is the distance between the two membranes and r_i is the distance of each flower to the centre of Flowerbed.

5.5. Conclusion

In this chapter, first the goal of building a contactless actuation system, designated Flowerbed, has been described: to investigate and enhance the dynamic behaviour for a controlled motion application. Then a predictive model has developed for the estimation of the dynamics performance. Finally, the design of Flowerbed and its predicted dynamic behaviour has been presented. To summarise, some conclusions can be drawn:

- For a controlled motion system, the dynamic response of the actuation system is very important, a longer delay of the output force will result in a lower achievable positioning control bandwidth. The concept of using a deformable surface has

been proposed with the expectation that the output force will respond fast to the command.

- In this chapter, design decisions have been presented for a experimental setup, named Flowerbed. It has been built in order to investigate the dynamics performance of such a contactless actuation system.
- The dynamic response of Flowerbed is determined by two main components: mechanical dynamic behaviour (mechanical actuating element to tilt of flowers) and thin film flow dynamic behaviour (tilt of flowers to output force). Of these two, the mechanical dynamics is predicted to be slower, and that will be the main factor limiting the performance of the system's dynamics.
- Using a model based on the time dependent Reynolds equation, the thin film flow dynamics is predicted to not have a strong influence, the output force can be considered to respond instantly to a tilt motion.
- With respect to the mechanical dynamic behaviour, an analysis has been performed for a structure that has been chosen for Flowerbed (Figure 5.18). From the result, with this structure, the tilting motion can be consider to be proportional to the displacement of the movable plate up till about 1000 Hz (resonance at 3300 Hz).
- Finally, combining the results of the analyses, the overall dynamics of this actuation system has been predicted and presented as shown in Figure 5.25

6

DYNAMIC BEHAVIOUR VALIDATION

In the previous chapter, the design of Flowerbed has been presented, and its dynamic performance predicted. In this chapter, first, the experimental setup is briefly described. Then the measurement results of the dynamic behaviour validation are presented.

6.1. Setup description

Presented in Chapter 5 is the structure of Flowerbed, focused mainly on the mechanism for controlling the deformation of the bearing surface. In order to use Flowerbed to levitate and actuate a thin substrate, it must be installed into a setup that can provide mechanical actuation as well as pneumatic pressure and vacuum supply. This installation is illustrated in Figure 6.1.

Shown in this figure, fixed to the base frame is the top plate of Flowerbed that contains the top thin membrane connecting all the flower's stems. In this top plate, a vacuum chamber is created, opened to all the gaps surrounding the flowers, sealed by the thin membrane and the vacuum sealing ring. At the side of this top plate, three vacuum ports have been made for the pneumatic connection with the vacuum supply, i.e. a regulator in series with a vacuum pump.

All the flower's stems are, again, connected together by the second thin membrane that is designed as a mid layer of the bottom plate (dark grey in Figure 6.1). This plate is movable and later is actuated by mechanical actuators for dynamics measurements. An in-plane movement of this plate is expected to generate an identical tilt of all flowers simultaneously. Additionally, not presented in this figure, the movable plate is slightly preloaded by three springs, pulling down from the base frame. This preloading structure has been design in order to remove initial buckling of the membranes that is caused by manufacturing imperfections.

The bottom end of each flower stem is connected to the pressure supply chamber through a flexible tube (made of polyurethane). The pressure inside this chamber is measured and controlled to be constant at a desired level by a regulator. Since this pressure supply block is relatively far from the flowerbed, and also, because of the low stiff-

6

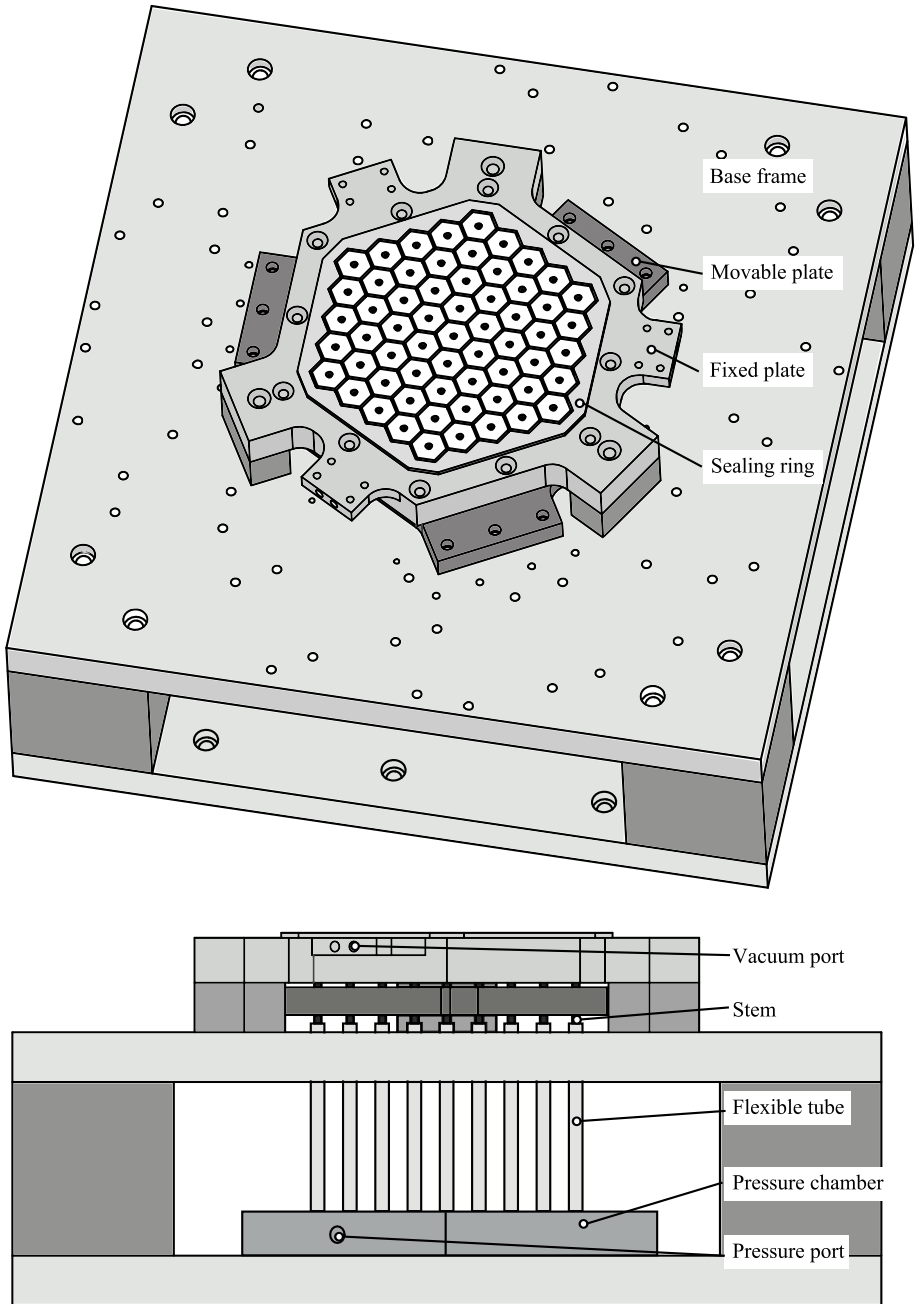


Figure 6.1: Flowerbed is mounted on a base frame so that experiments can be conducted.

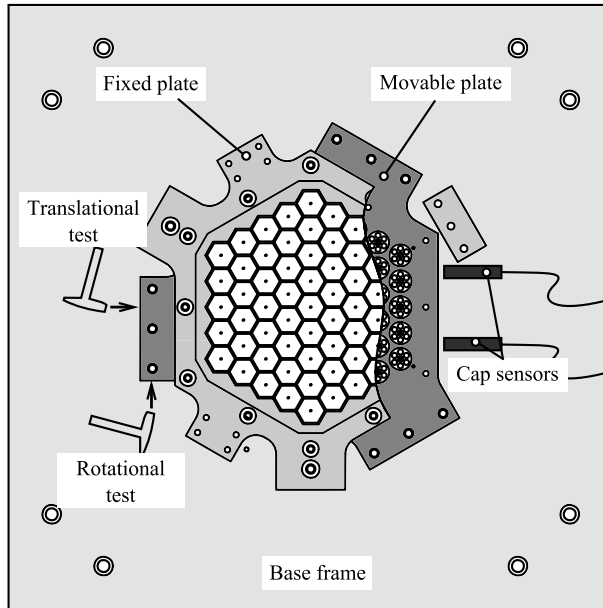


Figure 6.2: Two capacitance sensors are used to measure the position of the movable plate. These sensors have a range of $\pm 25 \mu\text{m}$ with a resolution of 0.5 nm at 1 kHz.

ness of the rubber like tubes, the influence of this block is expected to be small, thus negligible in the experiments.

6.2. Mechanical dynamics validation

The first experiments are conducted to verify the prediction of the mechanical dynamic behaviour of the structure of Flowerbed. These are performed while the bottom plate of the base frame is fixed firmly on a granite table. Shown in Figure 6.2 two capacitance sensors are mounted to the base frame such that both the translational and rotational movement of the movable plate can be extracted from the measurement data. These sensors are from Microsense, have a measuring range of $\pm 25 \mu\text{m}$ with a resolution of 0.5 nm at 1 kHz.

6.2.1. Preliminary resonance test

This experiment is to determine the frequency content of the movable plate planar motion as a result of excitation made with a hammer (Figure 6.2). The result of this experiment is shown in Figure 6.3 for translational mode excitation and in Figure 6.4 for rotational mode excitation. Compared to the prediction presented in Chapter 5, the first resonance, which is the result of an equivalent mass (mass of plate and inertia of flowers) combined with an equivalent stiffness from the two membranes, is quite close. However, higher order dynamics occur slightly sooner than expected, approximately at 1000 Hz.

This might be explained by the assumption that the fixed boundary condition of the top plate of Flowerbed is not fully valid in this experiment. In other words, at high frequency band, there is involvement of the base frame dynamics and/or the sensor mount dynamics. Since the sensors are sensitive, a small misalignment might result in a readout of the out-of-plane motion, e.g. tilting or out-of-plane deformation of the movable plate. Another possible reason is the uncertainty of the mechanism which is constructed using mechanical assembly (clamping screws and such have not been taken into account in the predictive model).

This experiment has been conducted again with a sensor's fixture that is modified to be stiffer, and there are some small changes in the result but only in the frequency range above 2000 Hz. More effort notwithstanding, the author failed in improving the experimental setup and determining the root causes of these higher order resonances. Because of time constraint, it has been accepted that the result of the dynamic behaviour is reliable up till 1000 Hz only.

6.2.2. Transmissibility from plate position to flower angle

The next experiment is to measure the dynamic tilt of the flowers in response to an in-plane movement of the movable plate. Even though the predicted decoupling frequency of 3300 Hz (see Chapter 5) could not be verified due to the fact that the reliable measurement is limited to 1000 Hz, this experiment has been conducted in order to validate if the relation between the tilt of the flowers and the movement of the movable plate can be considered as a proportional gain in this measurable frequency band. Furthermore, this experiment is also used to observe if the tilt of different flowers behaves identically or not.

In this experiment, similar to the previous one, the capacitance sensors are still used to measure the position of the movable plate. Next to these, the tilting angle of a flower is measured by a set of three sensors that are arranged as shown in Figure 6.5. Because of the small size of the flower's surface, fibre optic sensors have been used. This set of sensors is mounted to the granite table to measure the top of the flowers (without contact). The excitation in this experiment is generated by a preloaded piezo that has a stroke of $\pm 5 \mu\text{m}$. It is mounted on the base frame to actuate the movable plate in translational mode, and aligned such that rotational motion is minimised.

Shown in Figure 6.6 is the response of the movable plate when a two μm amplitude sine sweep from 0.5 Hz to 1000 Hz is fed to the piezo. The tilt of nine different flowers responding to this translational motion of the plate is presented in Figure 6.7. The result is not a perfect flat line as predicted because the other dynamics could not be eliminated in this measurement. Since a mass (approximately 1 kg) is actuated by the piezo, reaction forces are created and applied back to the base frame and the granite table. This reaction force is big enough to stimulate other (out-of-plane) modes of the system such as the base frame, the sensor frame and the out-of-plane mode of the flowers. Additionally, because it is not possible to align the piezo such that only the translational motion of the movable plate is actuated, the tilt caused by the plate rotational motion is included in this result (at about 110 Hz). It can be observed that the tilt of the middle flower (blue) is not affected by this mode.

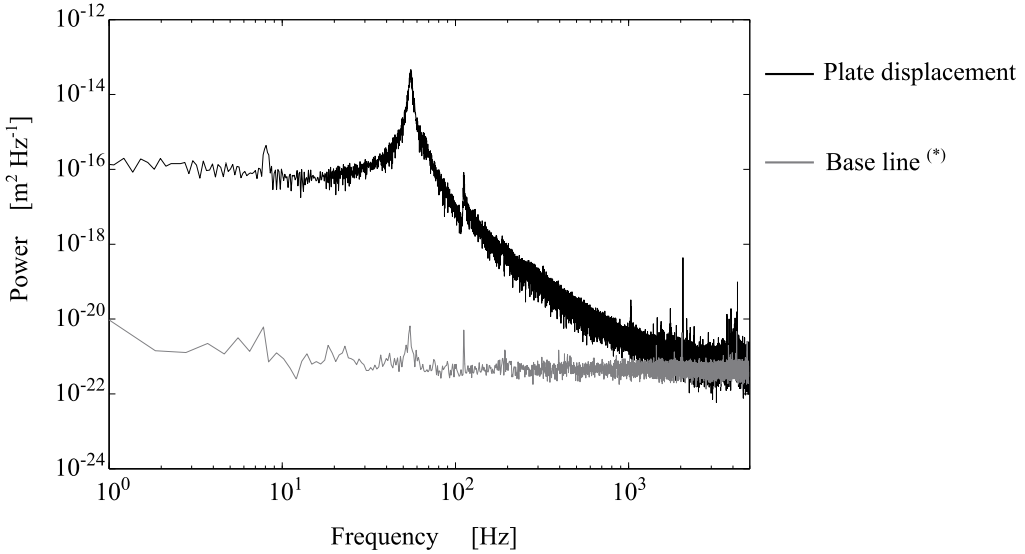


Figure 6.3: Frequency content of the in-plane translational motion of the movable plate when it is excited by a hammer. The first resonance is at 55 Hz which is match with the predicted model in Chapter 5.
 (*) This base line is obtained when the sensors are mounted in the system. Therefore both the translational and rotational resonances at 55 Hz and 111 Hz appear in the base line.

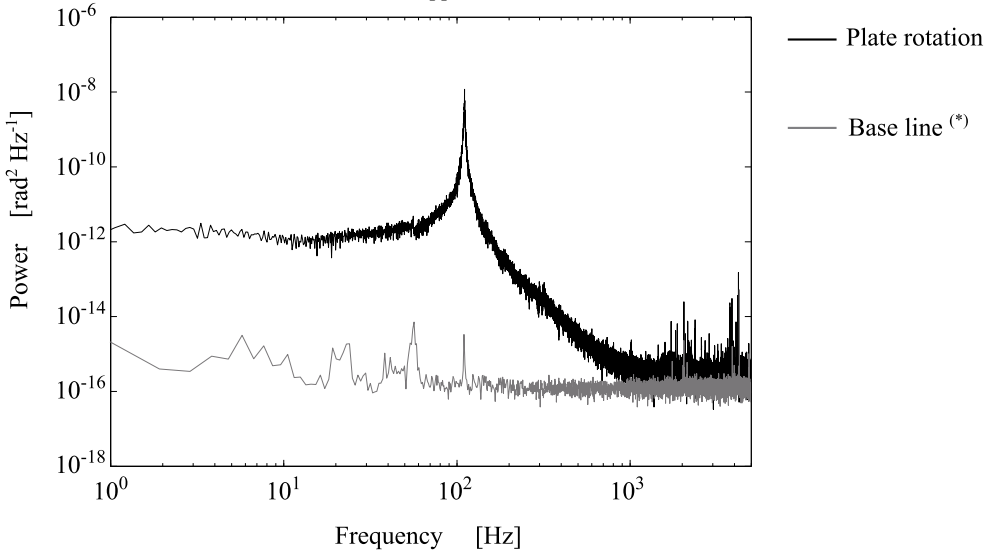


Figure 6.4: Frequency content of the in-plane rotational motion of the movable plate when it is excited by a hammer.
 (*) This base line is obtained when the sensors are mounted in the system. Therefore both the translational and rotational resonances at 55 Hz and 111 Hz appear in the base line.

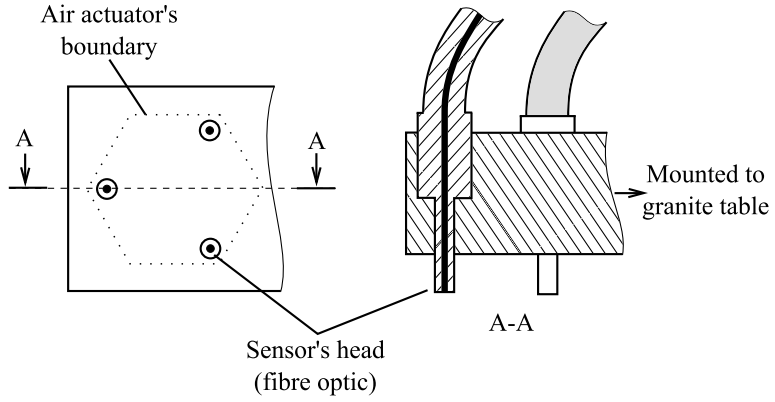


Figure 6.5: A set of three fibre optic sensors used to measure the tilting motion of the flowers.

6

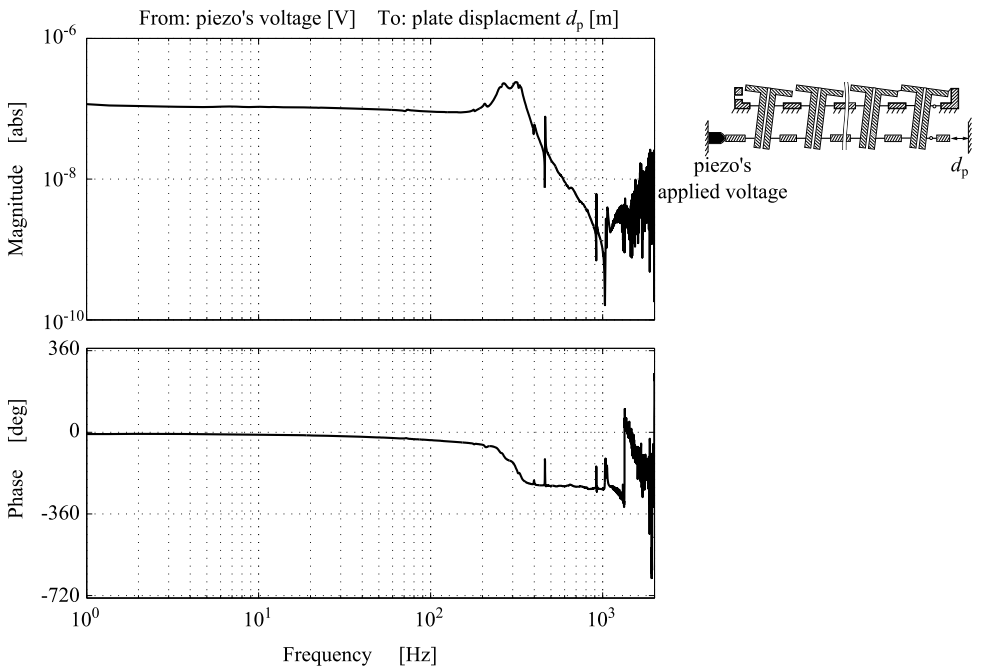


Figure 6.6: Dynamic response of the translational motion measured with a sine sweep input provided by a preloaded piezo

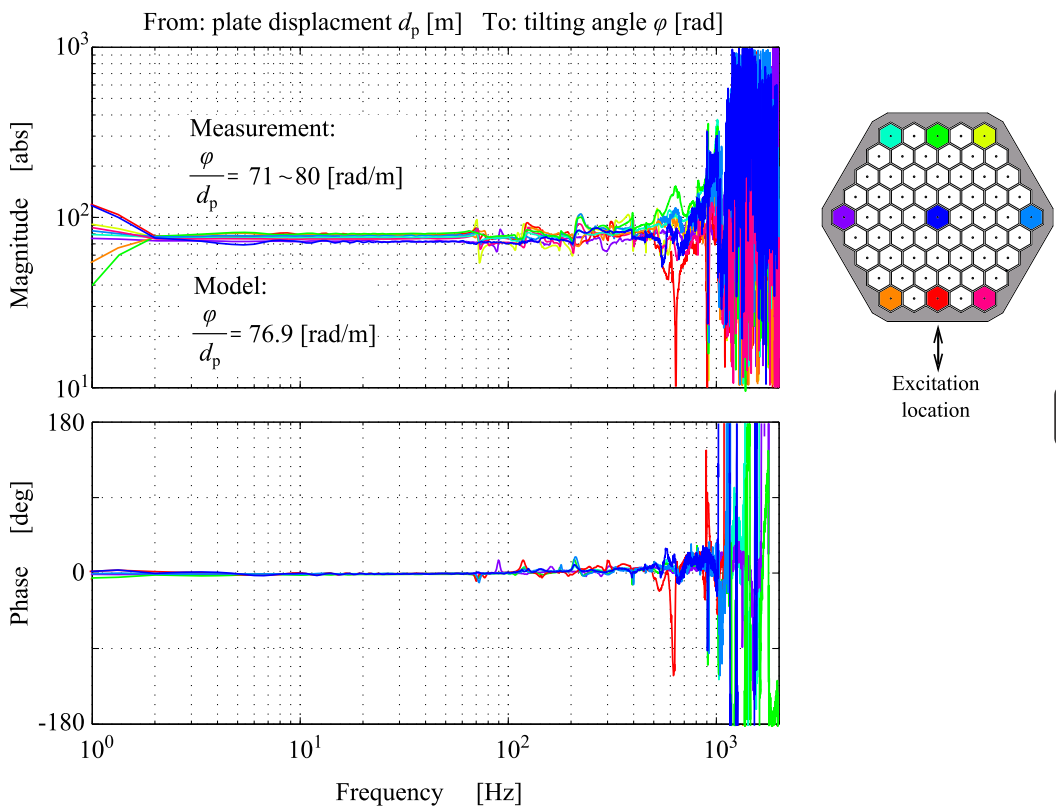


Figure 6.7: Dynamic behaviour from the movable plate motion to the tilting motion of the flower. Discarding imperfections caused by other dynamics stimulated by the reaction force in the experiment, the dynamics relation between the tilting angle of the flowers and the movement of the movable plate can be considered as a proportional gain, in the frequency band below 1000 Hz.

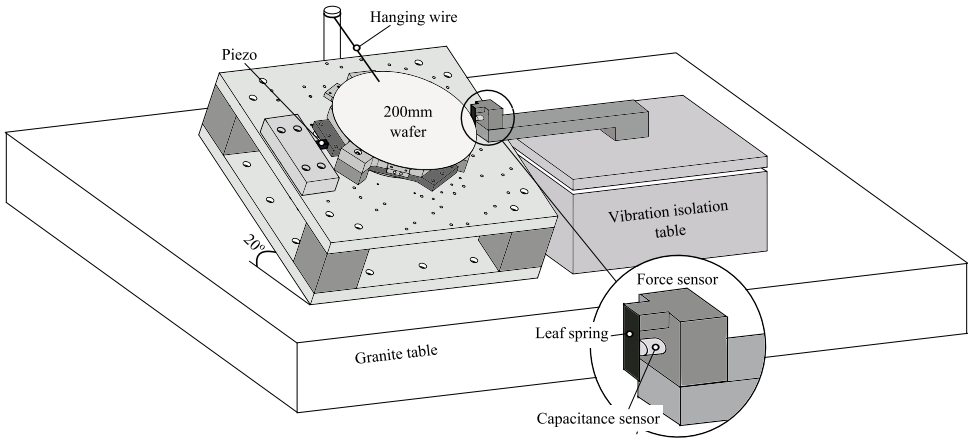


Figure 6.8: The experimental setup used to measure the dynamic response of the generated force. The custom-made force sensor is able to measure a force within the range of $\pm 17 \cdot 10^{-3}$ N with a resolution of $0.34 \cdot 10^{-6}$ N at 1 kHz. It has been built from a well defined leaf spring and a high resolution capacitance sensor.

6

However, from this result, the dynamic behaviour from the movable plate motion to the tilting motion of the flower still can be approximated to be a proportional gain in this frequency band. Furthermore, this measured gain is relatively close to the predicted value, 76.9 rad/m. The deviation of this gain for different flowers might be explained by the error of the tilting sensor in the alignment and/or calibration process.

6.3. Dynamic response of the force

In this section, the results of an experiment are presented, investigating the dynamic force in response to a movement of the movable plate. In an initial test, force and torque have been generated on a substrate by moving the movable plate manually. Since both force and torque can be created both only when the flowers surfaces are tilted (the difference is in the tilting orientation), it is valid to assume that the dynamic response from the plate movement to the force/torque is similar for all the in-plane degrees of freedom. Therefore, this experiment has been conducted for just one degree of freedom, from a translational movement of the plate to the resulting force in the same orientation.

The experiment is set up as shown in Figure 6.8. A 200 mm diameter wafer (mass of $53 \cdot 10^{-3}$ kg) is floated on top of Flowerbed. In this experiment, by regulators, the pressure and vacuum supply are kept at a constant level, e.g. 250 kPa relative and -10 kPa relative respectively. If the movable plate is kept at the initial position as manufactured, no force is exerted on the wafer, thus it can move freely in planar degrees of freedom. For the purpose of measuring the dynamic behaviour in just one degree of freedom, the wafer is constrained by being hung with a wire, and Flowerbed is tilted about 20° .

For measuring the movement of the movable plate, similar to previous experiments, two capacitance sensors that have a stroke of $\pm 25 \mu\text{m}$ are used. For the force measurement, because the resulting force exerted on the wafer is very small, predicted to

be $9 \cdot 10^{-3}$ N for a $2 \mu\text{m}$ displacement of the movable plate, the force sensors that were used in the experiment described in Chapter 3 could not be used due to the lack of resolution. Therefore a custom-made force sensor has been built and implemented into the setup as shown in Figure 6.8. It is built from a leaf spring with a known stiffness, 680 N m^{-1} , in combination with a high resolution capacitance sensor, which is the same type as the one used for measuring the plate's displacement. This results in a force sensor that can measure in the range of $\pm 17 \cdot 10^{-3}$ N with a resolution of $0.34 \cdot 10^{-6}$ N at 1 kHz. Note that the leaf spring stiffness has been identified experimentally, and the results are identical for both static and dynamic cases: measuring displacement when applying known masses (against gravity) and measuring resonance frequency when attached with a known mass. Furthermore, it has been verified to be a constant in the measuring range.

For convenience, the results presented in this section is chosen to be the measured displacement of the leaf spring, d_{sensor} , instead of the actual force values. Since the wafer is a pure floating mass, if an ideal force is applied on the wafer, the frequency response of d_{sensor} will be similar to the compliance transfer function of a mass spring system, containing only one resonance. In this case, this resonance is predicted to be 18 Hz, which is the result of the mass of the wafer combined with the stiffness of the sensor's leaf spring.

In this experiment, the excitation is provided by a stacked piezo that has a stroke of $\pm 5 \mu\text{m}$. Compared with the piezo used in the previous experiment, this piezo performs slightly better. Shown in Figure 6.9, the frequency response from the piezo voltage to the plate displacement, the first resonance is higher, achieves 450 Hz. Additionally, a filter has been designed and applied on the input sine sweep such that the resulting displacement of the plate has a more uniform amplitude over the measured frequency band. Shown in Figure 6.10 are the frequency content of the filtered input voltage and of the resulting displacement of the movable plate. With this method, the plate resonance at 450 Hz is eliminated in order to reduce the disturbance in the force measurement which is presented later in this section.

With the preparations described above, the experiment measuring the force dynamic response has been conducted. The result is presented in Figure 6.11. As expected, the response of d_{sensor} is similar to a mass spring system, resonating at approximately 18 Hz. Furthermore, up to about 400 Hz the magnitude of d_{sensor} reduces with a -2 slope and no additional phase lag is observed. This means that the resulting force on the wafer reacts instantly to a change in position of the movable plate within this frequency range. In the region after 400 Hz, some strange measured dynamic behaviour is observed. However it is not caused by the properties of Flowerbed itself. Indeed, starting from 400 Hz, the influence of mechanical disturbance becomes dominant compared to the force created by Flowerbed. Therefore the resulting response d_{sensor} no longer represents the dynamics performance of Flowerbed. This can be explained by Figure 6.12 where the frequency content of d_{sensor} is measured in three different cases. The red line is obtained with the data of d_{sensor} acquired while the experiment is conducted. The dark blue line is more or less the base line representing the performance of the force sensor. It is obtained with the data recorded while the movable plate is kept at stand still (static force). The light blue line shows the influence of mechanical disturbance. It is obtained with the data when the piezo is excited but no force is generated (the wafer floats with only pressure

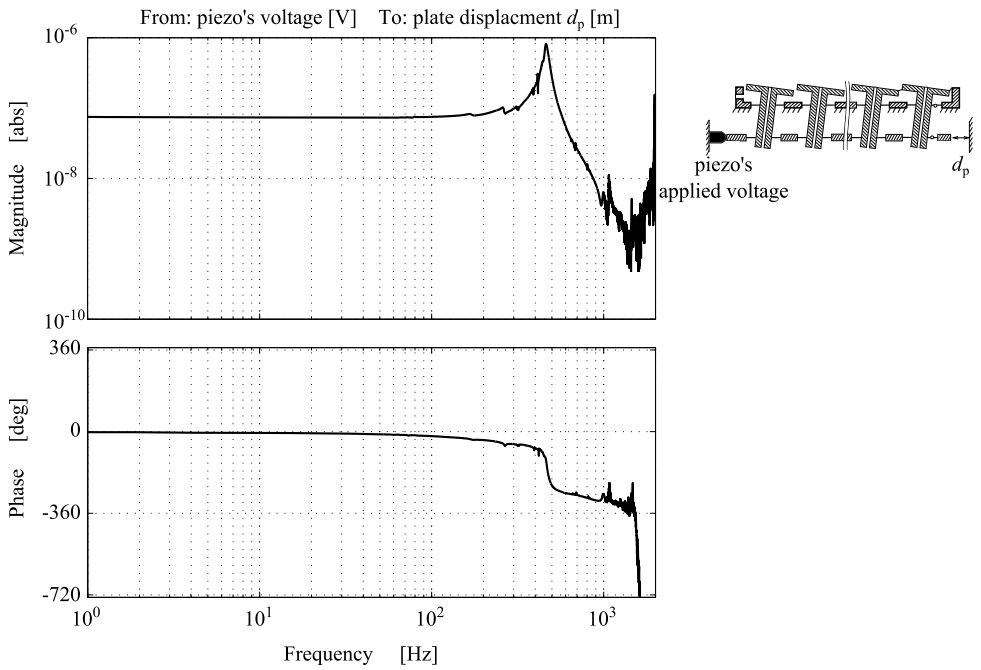


Figure 6.9: Dynamic response of the displacement of the movable plate when a new piezo is used in this experiment

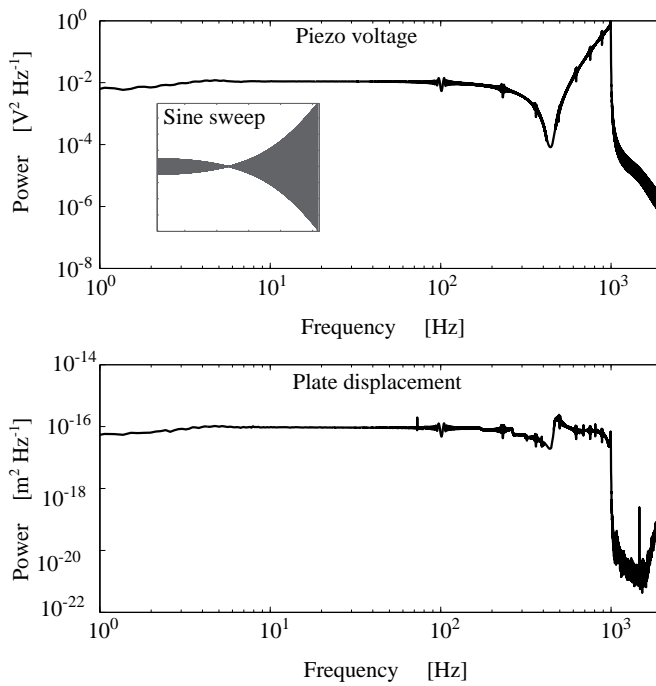


Figure 6.10: In order to produce a more uniform amplitude of the plate displacement over the measuring frequency band, a filter has been applied on the sine sweep signal fed into the piezo. This figure shows the result of this filter

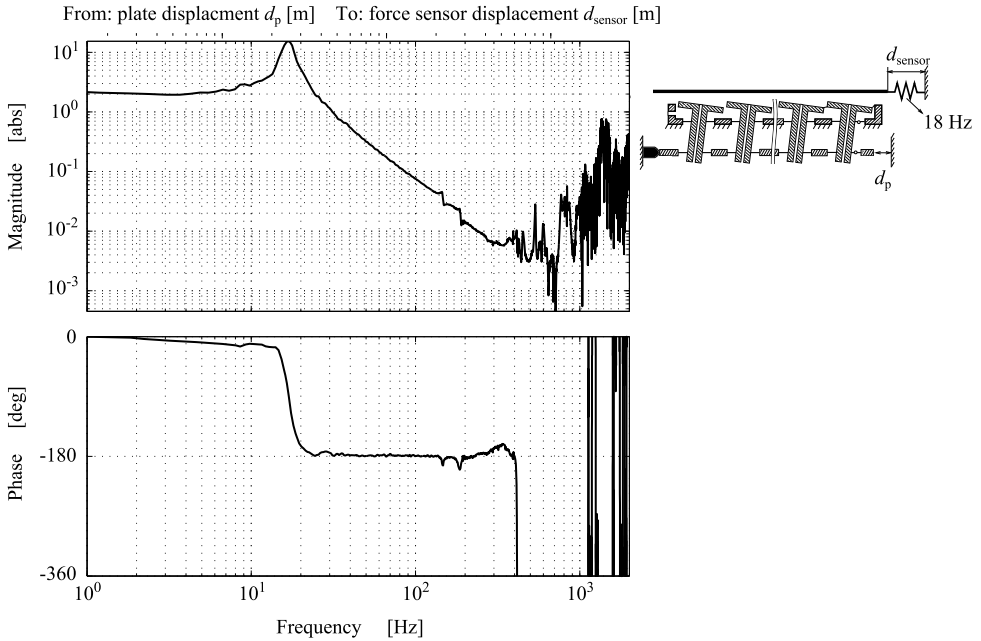


Figure 6.11: Dynamic response from the displacement of the movable plate to the displacement of the force sensor's leaf spring. This result shows that up to 400 Hz, the resulting force can be considered to be proportional to a change in the position of the movable plate. After 400 Hz, the measurement no longer reflects the dynamics performance of Flowerbed because the mechanical disturbance becomes more dominant. This influence of the mechanical disturbance can be explained by Figure 6.12.

6

supply, vacuum supply is turned off). Even though the force sensor has been placed on an electronic vibration isolation table, mechanical disturbance, which is stimulated by the piezo excitation, still enters the experiment result, affects heavily in the high frequency band. Therefore no conclusion can be drawn for the dynamics performance of Flowerbed after 400 Hz.

From this experimental result, it is safe to conclude that a proportional gain can be used to represent the dynamics relation between the generated force and the displacement of the movable plate in the frequency band below 400 Hz. For this operating conditions ($p_s - p_a = 250 \text{ kPa}$ and $p_v - p_a = -10 \text{ kPa}$), this gain is determined to be $1.4 \cdot 10^3 \text{ Nm}^{-1}$. Compared to the predicted value, it is just about one third. The main reason for this large difference is that the actual relative vacuum pressure at the edge of each flower is significantly reduced due to the pressure drop across the pipe line that is used to connect to the vacuum source (again the matter of designing the vacuum supply for such a system is really important). Finally, with the gained knowledge via this experiment, controllers can be designed for positioning the wafer. Using the rule of thumb, the achievable bandwidth for a feed back controller is estimated to be 150 Hz.

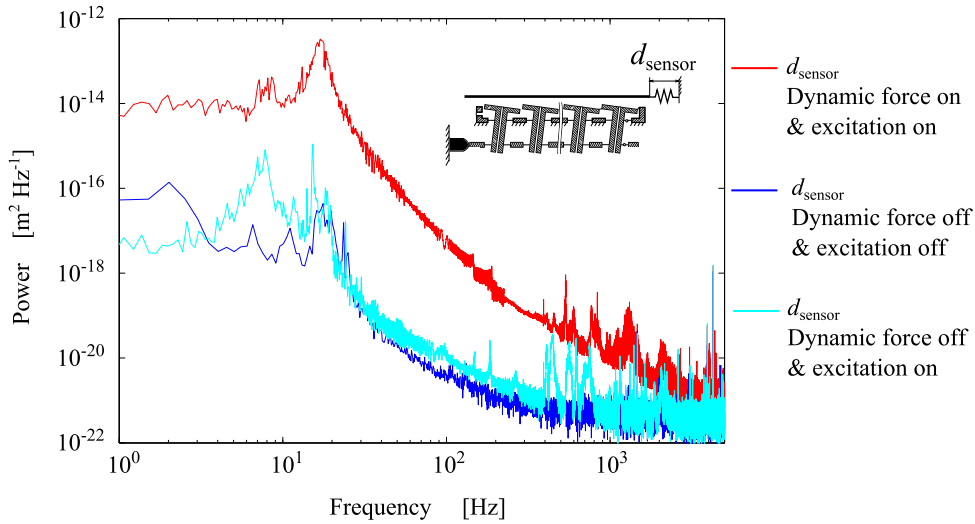


Figure 6.12: Frequency content of d_{sensor} measured in three different cases. The red line is obtained with the data acquired while the experiment is conducted, force is changed by the motion of the movable plate. The dark blue line is more less the base line representing the performance of the force sensor. It is obtained with the data recorded while the movable plate is kept stand still (static force). The light blue line shows the influence of mechanical disturbance that is stimulated by the piezo excitation (reaction force). It is obtained with the data when the piezo is excited but no force is generated: the wafer floats with only pressure supply, vacuum supply is turned off.

6.4. Conclusion

Described in this chapter, an experimental setup has been built, then experiments have been conducted in order to verify the performance of the Flowerbed's dynamics. From the result of these experiments, some conclusions can be drawn:

- With Flowerbed, force and torque can be produced on a thin substrate in planar degrees of freedom.
- Up to 1000 Hz, the tilting angle is proportional to the displacement of the movable stage. Measuring different flowers, the tilt response is quite similar, except for a small deviation of the gain. It varies from 71 rad m^{-1} to 80 rad m^{-1} (predicted value is 76.9 rad m^{-1}).
- Up to 400 Hz, the dynamic force responding to a displacement of the plate has been experimentally proven to also be a proportional gain. It does not mean that the force cannot be generated with higher frequencies. The dynamic force response just cannot be validated in the frequency band that is higher than 400 Hz, due to the limitations of the experimental setup.

7

CONCLUSIONS AND RECOMMENDATIONS

Closing this thesis, this chapter summarises the most important results obtained in this research. Also, experiences gained from less successful experiments and methods while conducting this research will be described. Based on that and on the current state of the research, recommendations for future research in this topic are provided.

7.1. Conclusions

The research of this new principle for developing a contactless actuation system has been started with the recognition that viscous traction forces of a thin film flow can be used very effectively to actuate thin substrates, due to the fact that viscous forces are dominant when the air film thickness is small, and thus the required flow rate is small. "How effective this principle can be" was the question that defined the goal for the research presented in this thesis. It was determined to be an exploration of the principle, focusing on two aspects: the efficiency in terms of the ratio between achievable force and flow rate, and the dynamic response of the force.

Aiming for this goal, the research started by introducing several potential concepts that can be used to control the force exerted on the substrate. In order to characterise these concepts, a model has been developed to predict the achievable force and the required flow. In Chapter 3, this model has been validated successfully by experimental results. It can be concluded that a model based on Reynold's equation for thin film media is sufficient for the prediction of the static performance of such a system. Furthermore, the deformation of the carried objects has been predicted and validated experimentally.

Based on this predictive model, optimal designs have been found for different configurations. Using the optimal geometry, the highest achievable force can be obtained for different operating conditions such as the minimal vacuum pressure, and the flow capacity of the supply. With this optimisation, a fair comparison between concepts can be produced in regard of the static performance. For a single-directional system, the

best performance is from the static step surface concept. For a bi-directional system, the best choice would be the deformable step surface that has a moderate performance and is simple to manufacture. Of course with some modifications, the static step surface concept can be used to structure a bi-directional system. However, it will be either more complex or have less performance. For a three planar degree of freedoms system, because of simplicity and feasibility, the deformable tilt surface is most suitable even if its performance is slightly lower than the deformable step surface.

Combining the results of the optimisation and characterising the bearing function, a design guideline on the pneumatic aspect of this type of contactless systems has been proposed. It can be presented in brief in three steps. First, the operating fly height needs to be chosen according to the manufacturing capability (smaller fly height is better). Second, based on the air supply specifications, the actuator array can be designed such that the highest force can be achieved. Third, the air flow restriction of the inlet can be chosen in order to make the system operated as desired, also the highest bearing stiffness can be achieved.

During the investigation of the static performance of two DoF tilted air actuators (Chapter 4), an interesting phenomenon has been found and proven both analytically and numerically. The created force is dependent only on the area of the actuator and the relative vacuum pressure, not on the actuator shape nor the inlet/outlet area. In other words, the traction force created by a tilt actuator is proportional to the preloaded load. Formulating this understanding differently, the third method for controlling the actuation force can be proposed: control of the propulsion force by varying the preload force. For example, if there are two identical actuator arrays that clamp the thin substrate in between, as long as the inlet pressure is high enough to ensure zero contact, the propulsion force will be proportional to the clamping force (Appendix B). This method does not require a vacuum source, the limitation due to the absolute vacuum is not applicable, and thus higher static performance can be achieved. The main disadvantage of this concept is that both sides of the substrate are (partially) covered by the system, and not fully available for processing steps. However, of course the property of zero mechanical contact is maintained.

The first main contribution described in this thesis is the exploration that has been performed on the static behaviour of this principle. The second contribution described in this thesis is an investigation on the dynamic behaviour of such a contactless actuation system. It was assumed that the dynamic response of the force can be enhanced by the deformable surface concept since it does not suffer the slow dynamic response of the air flow in a manifold. This assumption was confirmed by the work presented in Chapter 5 and 6. Firstly, a mechanism has been proposed for the purpose of deforming the bearing surface by a relative motion of two components. Based on this, an experimental setup, named Flowerbed, has been built. Secondly, with a developed model regarding the dynamic response from the change of the thin air film to the resultant force and subsequent the mechanical dynamic response, the propulsion force is predicted to be proportional to the relative mechanical motion up to about 1000 Hz. The limitation of the response of this system is caused by the mechanical dynamic behaviour since there are no clear dynamics involved in the response of the viscous traction force to the tilting of the flowers. Finally, presented in Chapter 6, this proportional behaviour has been

verified up to 400 Hz with experimental results. This lower frequency compared to modelling results of the verification does not reflect a limitation of the Flowerbed's dynamics. It is caused by the limitations of the experimental setup and the measuring equipment.

To summarise, in general, the knowledge gained from the research which has been presented in this thesis can help the system designer to be more confident in translating the requirements of an application into a real design that uses this principle of contactless actuation.

7.2. Recommendations

This section starts with a description of some knowledge learned from less successful roads taken while conducting this research. Based on that and on the current state of this research, some recommendations can be made for further research on the principle of using viscous traction force of a thin film flow to actuate a thin substrate. First, recommendations for further investigation on Flowerbed and the concept of deformable surfaces are described. Then a more general vision of research on this contactless actuation principle and its applications is presented.

The first recommendation is on the air restrictor type. Inheriting from the previous research, the capillary type of air flow restrictor has been used in this research for the inlet restriction because of its perceived linear and predictable properties. However, for the experiments presented in this research, due to the higher operating pressure difference, the flow inside these restrictors is found not laminar at all, but turbulent and compressible. And then, orifice restrictors become more predictable since they have been researched and used widely in conventional air bearings. For further research, orifice restrictors are strongly recommended to be used.

The second recommendation is based on a long period that the author tried to use additive manufacturing methods to build Flowerbed. Because there are many different technologies developed in this field, the design Flowerbed has been modified repeatedly to adopt the various constraints of these techniques. Furthermore, because of the lack of material quality that is not reported explicitly, a robust Flowerbed could not be built using this new manufacturing method. Still, from the author point of view, additive manufacturing is a potential alternative for building such a system. It will require more research both on the manufacturing technique and on the Flowerbed structure. This is a nice challenge for further research. However, since additive manufacturing is a rapid prototyping method that requires just a short period to make a prototype from a design, there might be a serious pitfall that the research evolves in a "trial and error" process.

Also from this period, it is learned that the mechanical deformation due to internal pressure and vacuum can be easily underestimated. Any chambers that are supplied with pressure or vacuum might have a deformation that is big enough to fail the system to operate. In order to have a successful design, this matter needs to be considered carefully.

7.2.1. Recommendations on Flowerbed

Firstly, with Flowerbed, the dynamic behaviour of a system that uses the deformation of the bearing surface to control the force/torque on a substrate has been investigated experimentally, but for just one degree of freedom. Therefore the next step on Flowerbed should be closing the loop for the positioning control of the substrate. In this step, the coupling effect between different degrees of freedom of the actuation will be investigated. Also unforeseen problems can be revealed.

Secondly, since the Flowerbed setup has been designed and built such that both the force type (low stiffness) and displacement type (high stiffness) mechanical actuators can be implemented, it is interesting to make a comparison on the pros and cons of using each type. Based on this comparison, the next version of a deformable surface contactless actuation system can be designed more effectively for the selected mechanical actuator.

Thirdly, an advise on the research on the deformable surface concept is to investigate the out-of-plane effect. As has been predicted, the substrate's attitude in space (compared to fixed world) changes when the deformation, which is the tilting motion of flowers, is controlled for a desired planar force. For some applications, the out-of-plane motion is not acceptable or at least must be predicted precisely. Therefore, the model used for predicting the fly height is recommended to be verified experimentally. With the gained knowledge in this matter, a zero out-of-plane motion actuation system might be designed, for example, a system consist of different bearing sections that are initially tilted so that a further tilt motion around this neutral position does not change the total restriction of the film.

Finally, also regarding to the out-of-plane motion matter, it is recommended to investigate the effect of substrate's deformation. As predicted and observed experimentally with Flowerbed, because of the substrate's deformation, when the substrate flies with a small height, contact between the substrate and the system might occur at the edges, especially the corners, of the bearing surface. In order to avoid this, a (passive) bearing system is recommended to be designed at the vacuum sealing ring so that the fly height can be realised with a smaller value thus reducing the air consumption.

7.2.2. General recommendations on the principle

For a general vision of the research in this topic, the following observations are outlined:

Firstly, even though the matter of the actuator shape has been considered in this research, a full topology study has not been performed yet, especially for the concept of controlled pressure variation. As presented in this research, the best actuator shape has been determined for the tilting actuator where the resulting force is independent of the shape. However, this is not the case for the step like surface (normally used in the pressure variation concept) or other types of deformation (not tilting). Therefore, there is still room for a topology study in this concept such as what would be the most efficient shape of the actuator, where is the best location for the inlet and outlet, what is the effect of the size and the shape of the inlet/outlet port.

Secondly, all the experimental setups in this research can be operated only while the bearing surface is fully covered by the substrate. Thus it is now suitable just for position-

ing applications not for transporting. The reason of this problem is mainly caused by the vacuum supply: the vacuum pressure cannot be maintained at a desired level when there are some vacuum ports opened to ambient pressure. This is because the outlet restriction needs to be small. In order to solve this problem, two approaches are proposed as following. The first approach is to modify the vacuum supply system such that the vacuum port will only be turned on whenever it is covered by the substrate, e.g by mean of valves. The second approach is to use another method for preloading, instead of vacuum, e.g. magnetic force or applying pressure on the other side of the substrate.

Thirdly, as it has been stated, the deformable surface concept is just one of the alternatives that can be used to enhance the dynamics performance. Using distributed proportional valves that are placed close to the bearing surface will result in a faster dynamic response as well. This is a nice direction for the research in this topic, especially when MEMS technologies have a strong growth nowadays that enable the possibility of manufacturing micro actuators at low costs.

Last but not least, the final recommendation is to search for efficient solutions that can be used to manufacture this type of system. The trend of the future substrates is not only to be thinner but also to become larger, and accordingly, the actuator array is required to be larger while the size of each actuator is expected to be smaller. These requirements pose a challenge in building such a contactless actuation system.

A

OVERVIEW OF PREVIOUS RESEARCH

This appendix describes briefly the research that has been conducted in TU Delft in the period 2007-2011, investigating and building a contact-less wafer positioning system using an air film as a motor/bearing unit. Firstly, the motor function and the bearing function of an active air film are interpreted. Secondly, the positioning performance of an experimental setup, the contact-less wafer stage, is summarized. Finally, recommendations and remaining questions from this research are identified and reviewed for the next period of the research in this topic.

A.1. Contactless actuation using an active air film

The bearing function of the contactless actuation system using viscous traction force of an air film works comparatively to a conventional vacuum preloaded air bearing. It is constructed to have a surface that contains multiple inlets connected to a high supply pressure source and multiple outlets connected to a sub-ambient vacuum pressure sink. The additional motor function is obtained by modifying the bearing surface into an array of actuator cells such that the total viscous traction force resulted from all the local air flows is non-zero.

A.1.1. Motor Function

Shown in Figure A.1, one way to modify the surface to obtain the motor function is to partly recess the surface with a pocket in the order of several tens μm . The inlet and outlet grooves are placed inside this recess, at two opposite sides. Each recess with the surrounding dam can be identified a one actuator cell. The dimensions for a single cell are described in Figure A.1b. The size of the actuator cell and its recess are l and αl respectively, the dam width is therefore defined as $(1 - \alpha)l$, with $\alpha < 1$. The film thickness or the fly height above the dam and the recess is given by h and βh , where β is defined as the ratio between these two fly heights, $\beta \geq 1$.

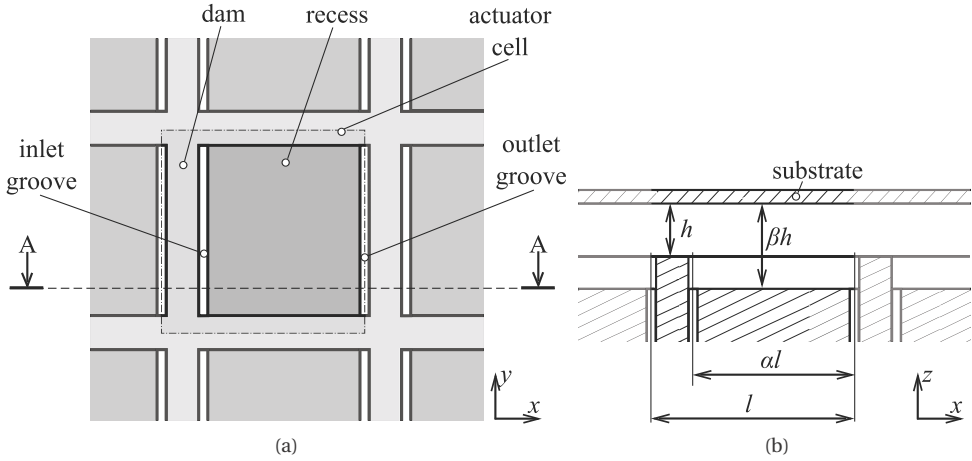


Figure A.1: Top view of an actuator array (a), Cross section A-A with a substrate on top (b)

In this research, the actuator cell is assumed to be square in shape and has a size in the order of $10\text{ mm} \times 10\text{ mm}$. The typical size of the recess is $8\text{ mm} \times 8\text{ mm}$, resulting in a dam width of 2 mm ($\alpha = 0.8$). The fly height above the dam and the recess are normally set at $10\text{ }\mu\text{m}$ and $30\text{ }\mu\text{m}$ respectively, ($\beta = 3$). With these chosen dimensions of the actuator cell geometry, a force can be generated on the wafer when a pressure difference is applied between the inlet and outlet of the actuator cells in the array.

For the initial analysis, the actuator cells are assumed to have infinite width (the dimension in y -axis). With this simplification, when a pressure difference ($p^+ - p^-$) is present between the inlet and outlet grooves, there are only two flow paths in each single cell, both perpendicular to the grooves: one from the inlet groove through the recess to the outlet groove (main flow) and another one from the inlet groove over the dam to the outlet groove of the neighbour cell (drag flow). Assuming that these flows are "zero-slip" and can be considered to be Poiseuille type, the velocity profile $v(z)$ can be determined to be parabolic (Figure A.2). At the interface with the substrate (and the actuator surface), the flow has zero velocity, and induces a viscous shear stress that can be derived from its velocity profile. Integrating the shear stress over the length of the flow paths results in the force per unit width generated by these flows. The calculations can be performed for the recess domain and the dam domain:

Recess domain - the main flow: Assuming a uniform film height and laminar flow, the Navier-Stokes equation in vertical direction reduces to:

$$\eta \frac{\partial^2 v}{\partial z^2} = - \frac{\partial p}{\partial x} \quad (\text{A.1})$$

where μ is the viscosity of air. Furthermore, according to standard thin film flow conditions, it is assumed that the pressure is constant in the z -direction and the pressure gradient dp/dx can be approximated. Equation A.1 becomes:

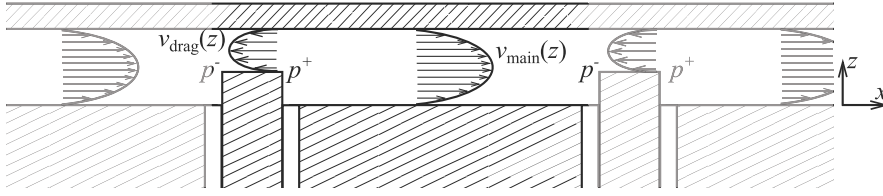


Figure A.2: The assumed velocity profile of the main flow and the drag flow inside an actuator cell

$$\eta \frac{\partial^2 v}{\partial z^2} = -\frac{p^+ - p^-}{\alpha l} \quad (\text{A.2})$$

Integrating twice with respect to z with the "zero-slip" boundary condition results in the equation of the velocity profile of the main flow

$$v_{\text{main}}(z) = -\frac{p^+ - p^-}{2\alpha l \eta} (z^2 - \beta h z) \quad 0 \leq z \leq \beta h \quad (\text{A.3})$$

The shear stress on the substrate is equal to the reaction of the viscosity times the gradient of the velocity profile at the interface

$$\tau_{\text{main}} = -\eta \left. \frac{dv}{dz} \right|_{z=\beta h} = \frac{\beta h}{2} \frac{p^+ - p^-}{\alpha l} \quad (\text{A.4})$$

Integrating this shear stress over the length of the recess yields the force per unit width of the actuator generated by the main flow

$$F_{\text{main}} = \frac{\beta h}{2} (p^+ - p^-) \quad (\text{A.5})$$

Dam domain - the drag flow: Similar to the calculations for the main flow, the velocity profile of the drag flow, the shear stress and the force per unit width resulted from the drag flow can be derived:

$$v_{\text{drag}}(z) = \frac{p^+ - p^-}{2(1-\alpha)l\eta} (z^2 - hz) \quad 0 \leq z \leq h \quad (\text{A.6})$$

$$\tau_{\text{drag}} = -\eta \left. \frac{dv}{dz} \right|_{z=h} = -\frac{h}{2} \frac{p^+ - p^-}{(1-\alpha)l} \quad (\text{A.7})$$

$$F_{\text{drag}} = -\frac{h}{2} (p^+ - p^-) \quad (\text{A.8})$$

Summing the viscous force generated by the main flow and the drag flow results in the net force per unit width of a single actuator cell

$$F_{\text{actuator}} = F_{\text{main}} + F_{\text{drag}} = \frac{(\beta-1)h}{2} (p^+ - p^-) \quad (\text{A.9})$$

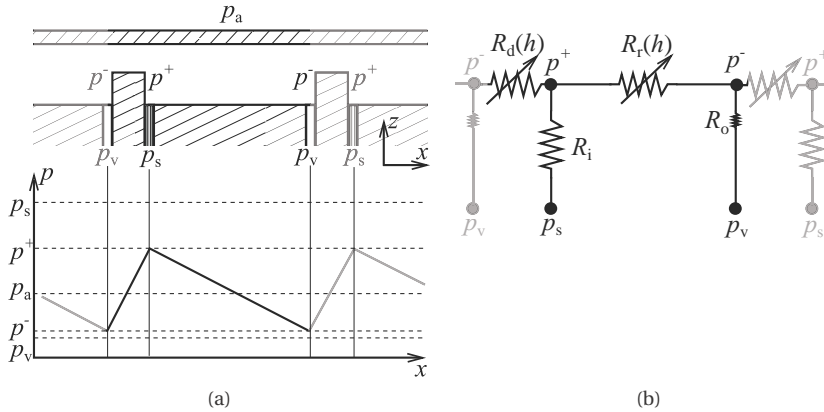


Figure A.3: Actuator with an additional restrictor at the inlet and the resulted pressure distribution (a), Flow schematic used for explaining the bearing function (b)

It should be noted that the term $(\beta - 1)h$ is a geometric constant, i.e. the depth of the recess. Equation A.9 clearly proves that modifying a flat bearing surface into an array of actuator cells is necessary for achieving a non-zero force on the substrate. If the recess depth is set at zero ($\beta = 1$), the net traction force would also be zero independent of the magnitude of the pressure difference.

A.1.2. Bearing Function

As stated earlier, a contactless actuation system using this principle works similar to a vacuum preloaded air bearing with an additional motor function obtained by modifying the bearing surface. This section interprets the bearing function of the contactless actuation system. The bearing function is a combination of two properties: the load capacity and the bearing stiffness. The load capacity of an air bearing determines the capability of carrying the weight of the borne object. As shown in Figure A.3a, because the pressure drops linearly over the recesses and the dams from the inlet to the outlets, the load capacity per unit area of the actuator is therefore an average of the inlet and the outlet pressure

$$\bar{w} = \frac{p^+ + p^-}{2} \quad (\text{A.10})$$

For the applications relevant for this study, in which the borne object is a thin substrate, the load capacity does not have to be high. Since a 0.5 mm-thickness wafer/glass sheet has a weight per unit area of about 12 N m^{-2} , the load capacity per unit area should be 12 Pa higher than ambient pressure p_a , whereas the pressure difference ($p^+ - p^-$) is in the order of several tens of kPa.

The second property of the bearing function is the bearing stiffness (vertical stiffness). This distributed stiffness is needed for preventing mechanical contact even for substrates that initially are not flat. Placing a flow restrictor before the inlet in the flow network is required to realize a positive stiffness. The flow schematic shown in Figure

A.3b can be used to explain how bearing stiffness is created. The inlet pressure inside the pocket p^+ is the result from connecting the inlet to a pressure source p_s through an air restrictor R_i . The air flow streams from the inlet to the outlet across the recess and the dam. R_r and R_d are defined as the restriction of the recess flow path and the dam flow path respectively. They are dependent on the film height. The outlet pressure p^- is below ambient pressure because of the connection to a sub-ambient pressure sink p_v . This connection typically has a small restriction value R_o . In the analysis of the bearing stiffness, the supply pressure source p_s and sink p_v are considered to be kept constant. When the film height decreases, the restriction of the air film increases resulting in a lower flow through the actuator. Since p_s and p_v are constant, p^+ increases due to the reduction of the pressure drop over the inlet restrictor which is the result of the decrease of the air flow. The increase of p^+ acts like a spring, generates a force tending to push the substrate back to its original height. Using the same manner, it can be explained that an increase of outlet restriction R_o will reduce the bearing stiffness.

Following is the explanation for the bearing stiffness based on a mathematical model. From the flow schematic shown in Figure A.3b, with the incompressible flow assumption, the volume flow is conserved. Then, the system equations can be derived

$$p_s - p^+ = QR_i \quad (\text{A.11})$$

$$p^+ - p^- = QR_a(h) \quad (\text{A.12})$$

$$p^- - p_v = QR_o \quad (\text{A.13})$$

where Q is the volume flow, $R_a(h)$ is a function of the film height h , represents the restriction of actuator. It is the combination of the two restrictors R_r and R_d , $R_a = (R_r^{-1} + R_d^{-1})^{-1}$. With a constant set of supply pressure p_s and p_v , the resulting pressure at the inlet and outlet are

$$p^+ = \frac{p_s(R_a(h) + R_o) + p_v R_i}{R_i + R_a(h) + R_o} \quad (\text{A.14})$$

$$p^- = \frac{p_v(R_a(h) + R_i) + p_s R_o}{R_i + R_a(h) + R_o} \quad (\text{A.15})$$

the load capacity per unit area will be

$$\bar{w} = \frac{p^+ + p^-}{2} = \frac{p_s + p_v}{2} + (p_s - p_v) \frac{R_o - R_i}{2(R_o + R_i + R_a(h))} \quad (\text{A.16})$$

the vertical stiffness per unit area can be derived by taking the derivative of the load capacity with respect to the film height

$$\bar{k} = -\frac{d\bar{w}}{dh} = -\frac{R'_a(R_i - R_o)}{2(R_i + R_a + R_o)^2} (p_s - p_v) \quad (\text{A.17})$$

where R_a and R'_a are the actuator restriction and its the derivative at a designed nominal fly height. The stiffness is positive since R'_a has a negative value due to the fact that the restriction of the air film increases when the fly height decreases.

A.2. Contactless wafer positioning stage

A.2.1. Multi-DoF contactless actuation system

The actuator cell described previously can generate a force in only one direction because of its asymmetric design, to wit the difference between the inlet and outlet restriction. In order to construct a multi-DoF contactless actuation system, two alternatives have been considered. One is to use multi-directional actuator cells in which the flow can be controlled by a multi-port (proportional) valve. Using this method however results in a challenge: the bearing stiffness is more difficult to be ensured. The restriction of an air port must be increased whenever it is used as an inlet and reduced when it is an outlet. Furthermore, at the crossover moment while switching the flow direction, the flow is zero, the bearing stiffness therefore becomes zero. Some potential solutions have been thought of to solve this problem. The first one is to attain the bearing function separately from the motor function by a part of the active surface. The second potential solution, which is more complicated, is to use variable restrictors so that the inlet restriction can be maintained to be higher than the outlet restriction. The third solution is to obtain the bearing stiffness actively by means of controllers that use local (mini) valves and sensors to preserve a constant fly height. The fourth solution is to use separate inlet and outlet restrictors in one groove.

The other alternative is to construct a multi-DoF contactless actuation system based on clusters of single DoF actuators. Each cluster consists of three or four actuator cells that are arranged in such a way that the force can be generated in various direction. Figure A.4 shows three among many possibilities for a multi-DoF cluster of actuators. The '+' and '-' signs represent the inlet and outlet. The dash arrows shows the main flow direction, while the solid arrows illustrate the force direction of each actuator. In this concept, the outlet pressure is always kept at a constant level, only the pressure at the inlets is varied. For instance in the first configuration (Figure A.4a), when there is no force required to exert on the substrate (neutral operating point), all actuators still produce forces that cancel each other out because they have the same magnitude in opposing directions. When a non-zero net force is needed, the inlet pressure will be controlled in order to unbalance these forces in a desired manner. The second and the third configurations (Figure A.4b and A.4c) also use this way to control the generated force. The only difference is that each actuator cell is able to act in two opposing directions. In other words, for these two configurations, the balanced forces in the neutral operating point do not happen between two cells but inside each cell.

In the scope of the research of Wesselingh, the second alternative, using multi-DoF clusters of actuators, was selected to be the most appropriate option because it is simple and good enough to prove the feasibility of this new principle of handling thin substrates without mechanical contact.

A.2.2. Contactless wafer positioning stage

In order to demonstrate the new principle for contactless actuation systems, three experimental setups have been built. The first one has proven that a force can be achieved

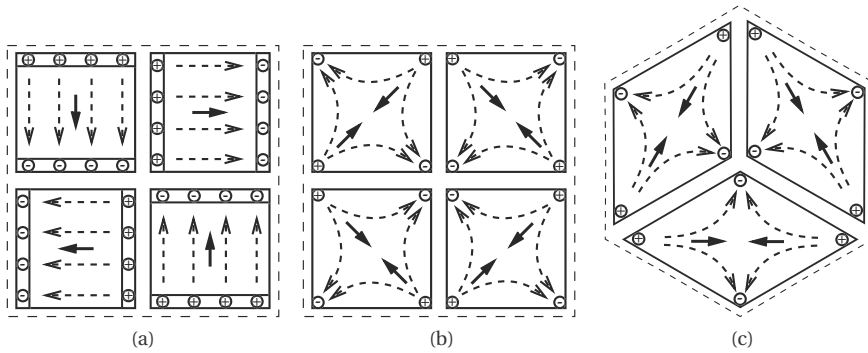


Figure A.4: Three examples for multi-DoF actuator clusters

on a substrate carried on top of an air film. The second setup, a 1-DoF positioning system, has showed that the substrate position can be controlled by varying the supply pressure with proportional valves. The third one, which is named "Waferstage", has successfully demonstrated how it performs in using an active air film to position a thin substrate without mechanical contact. Only the third setup is briefly presented in this thesis. Its performance is described as the "state of the art", starting point for the subsequent research described in this thesis.

Waferstage design: For multi-DoF actuation, Waferstage uses the second configuration of the options presented in previous section in Figure A.4. It has been built as an array of 9 clusters that is designed to handle a 100 mm wafer. Each cluster consists of 4 square actuators with a size of 10 mm \times 10 mm including the dam width of 2 mm. The recess depth is designed to be 20 μm resulting in a predicted force constant of $0.118 \cdot 10^{-6} \text{ N Pa}^{-1}$ in all directions for each cluster. The force constant is defined as the net force that can be generated by 1 Pa of pressure difference. Note that this pressure difference is not the difference between the inlet and the outlet pressure ($p_s - p_v$) but between the two groups of inlets that create unbalanced force inside a cluster. As an example depicted in Figure A.5a, when a force is generated toward the right direction, it is the pressure difference between the two inlet groups that are marked with dark and light '+' signs. For the whole system of 9 clusters, a force constant of $1.062 \cdot 10^{-6} \text{ N Pa}^{-1}$ is predicted. The nominal fly height is chosen to be 10 μm , resulting in a calculated air film restriction of $6.2 \cdot 10^9 \text{ Pa s m}^{-3}$ for each actuator. Using an optimised value for the inlet restriction which is $12.3 \cdot 10^9 \text{ Pa s m}^{-3}$ for each inlet, Waferstage can generate a stiffness of $525 \cdot 10^6 \text{ Pa m}^{-1}$ when it is operated with $p_s - p_v = 40 \text{ kPa}$. This operating point is chosen for Waferstage to be able to deliver a maximum acceleration of 1.5 m s^{-2} on a 100 mm wafer that has a mass of $9.5 \cdot 10^{-3} \text{ kg}$. The designed specifications and properties of Waferstage are summarised in Table A.1.

The structure of Waferstage is shown in Figure A.6. The inlets and outlets of the actuator plate are connected to the air source and sink through a complex manifold, made with additive manufacturing method. This manifold consists of in total nine channels.

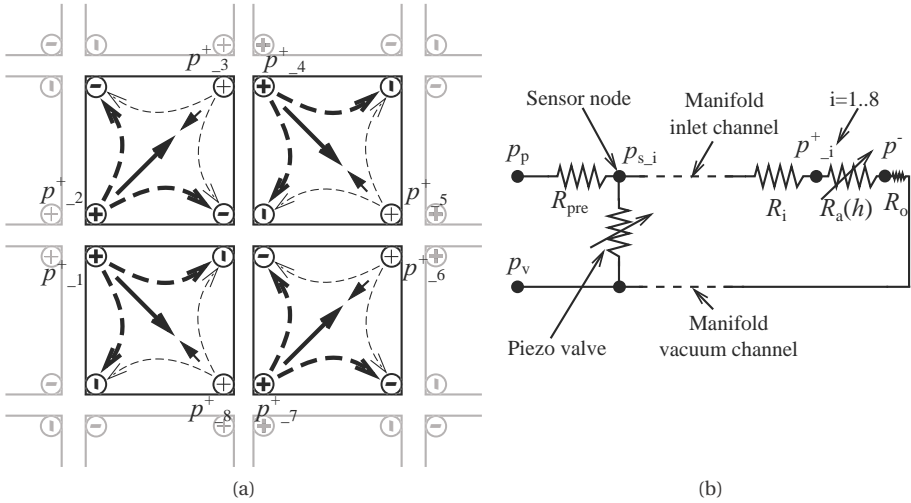


Figure A.5: An example illustrating the force is controlled toward the right direction by a cluster (a), and the flow net work for controlling the inlet pressure (b)

	Property	value
Specifications	Object mass [kg]	$9.5 \cdot 10^{-3}$
	Max acceleration [ms^{-2}]	1.5
	Max velocity [ms^{-1}]	0.75
	Positioning accuracy [μm]	1.3
Designed parameter	Number of actuators [-]	36
	Actuator size [mm \times mm]	10 \times 10
	Recess size [mm \times mm]	8 \times 8
	Recess depth [μm]	20
	Supply inlet pressure $p_{s,i}$ [kPa]	30
	Vacuum pressure p_v [kPa]	-10
	Exciting range [kPa]	± 7.3
	Fly height [μm]	10
Predicted performance	Actuator air restriction [Pa s m^{-3}]	$6.2 \cdot 10^9$
	Force constant [N Pa^{-1}]	$1.062 \cdot 10^{-6}$
	Max force [N]	$15.5 \cdot 10^{-3}$
	Bearing stiffness [Pa m^{-1}]	$525 \cdot 10^6$

Table A.1: Waferstage designed specifications and geometry

One of them is used to evenly distribute the uniform vacuum pressure to all the outlet points on the actuator plate. The remaining eight channels are connected to the eight inlet points of each actuator cluster. Piezo valves and pressure sensors are placed at the other ends of these channels in order to control the inlet supply pressure $p_{s,i}$ ($i = 1..8$). The flow-pressure schematic of one inlet channel is presented in Figure A.5b. The system pressure p_p and vacuum pressure p_v are kept constant by two pressure regulators

(at 70 kPa and -10 kPa for the designed specifications). The porous pre-restrictor R_{pre} is chosen to have a resistance of $1.7 \cdot 10^9 \text{ Pa s m}^{-3}$ so that the inlet pressure $p_{s,i}$ can be excited in a range of ± 7.3 kPa. At the neutral operating point, the valve is set at the middle position (half closed half open), resulting a nominal inlet pressure $p_{s,i}$ of 30 kPa. With this configuration, the inlet pressure can be controlled around the nominal level: it can be increased by closing the valve and reduced by opening the valve.

The wafer position is measured by a set of three linear encoders on the top surface of the wafer. This wafer is specially prepared for the experiment of determining the achievable accuracy. It is engraved with optical grating lines so that the encoder heads can read out its position. Two versions of the encoder heads has been selected that have different resolution: 10 nm per increment and 1 nm per increment. Due to the limited reading speed of the data-acquisition system (5 MHz), the maximum measurable velocity of the wafer is limited at 0.034 m s^{-1} for the 10 nm resolution version, and 0.0034 m s^{-1} for the 1 nm resolution version. As a result the designed maximum wafer velocity of 0.75 m s^{-1} could not be verified with this setup.

Waferstage controller As shown in Figure A.7, the Waferstage controller is structured with two loops. The inner pressure loop controls the supply pressure of the eight inlet channels generating the required force on the wafer. The outer loop controls the position of the wafer in three planar degree of freedom by setting the required pressure to the inner loop.

In order to design the controller for the inner loop, the frequency response from the valve excitation to the pressure at the eight inlet channels has been measured. Figure A.8 shows the measured response of one channel, the first real pole at around 13 Hz is the result of the combination of the channel capacitance and the valve restriction (similar to an electronic RC-effect). The next complex zero pair and pole pair are located at around 350 Hz and 770 Hz respectively. They are caused by the acoustic effect inside the air channel. Based on the measured frequency response, a PI²D-controller has been designed and implemented for the inner pressure loop. A bandwidth of 120 Hz can be achieved with a gain margin of 6 dB and a phase margin of 30° .

The positioning plant of the outer loop is simpler. Since the wafer is carried on an air bearing without any mechanical contacts, the position dynamic behaves purely as a floating mass. The bandwidth of the outer position loop is however limited by the performance of the inner loop where the generated force is controlled. In this setup, a bandwidth of 30 Hz is obtain with a gain margin of 6 dB and a phase margin of 30° .

Waferstage performance Two experiments have been conducted in order to evaluate the performance of Waferstage. Firstly, the standstill positioning accuracy can be assessed using the Cumulative Power Spectrum plot shown in Figure A.9. With the 30 Hz bandwidth positioning controller, combined with a vibration isolation system that rejects the floor disturbance, the positioning error can be kept within a range of 5.8 nm. The contributions to this error are mainly located below 100 Hz. From this experiment, it can be concluded that the internal disturbances, which are mainly caused by the air flow in the supply system, are very small.

The second experiment, point to point positioning, has been used to evaluate the

A

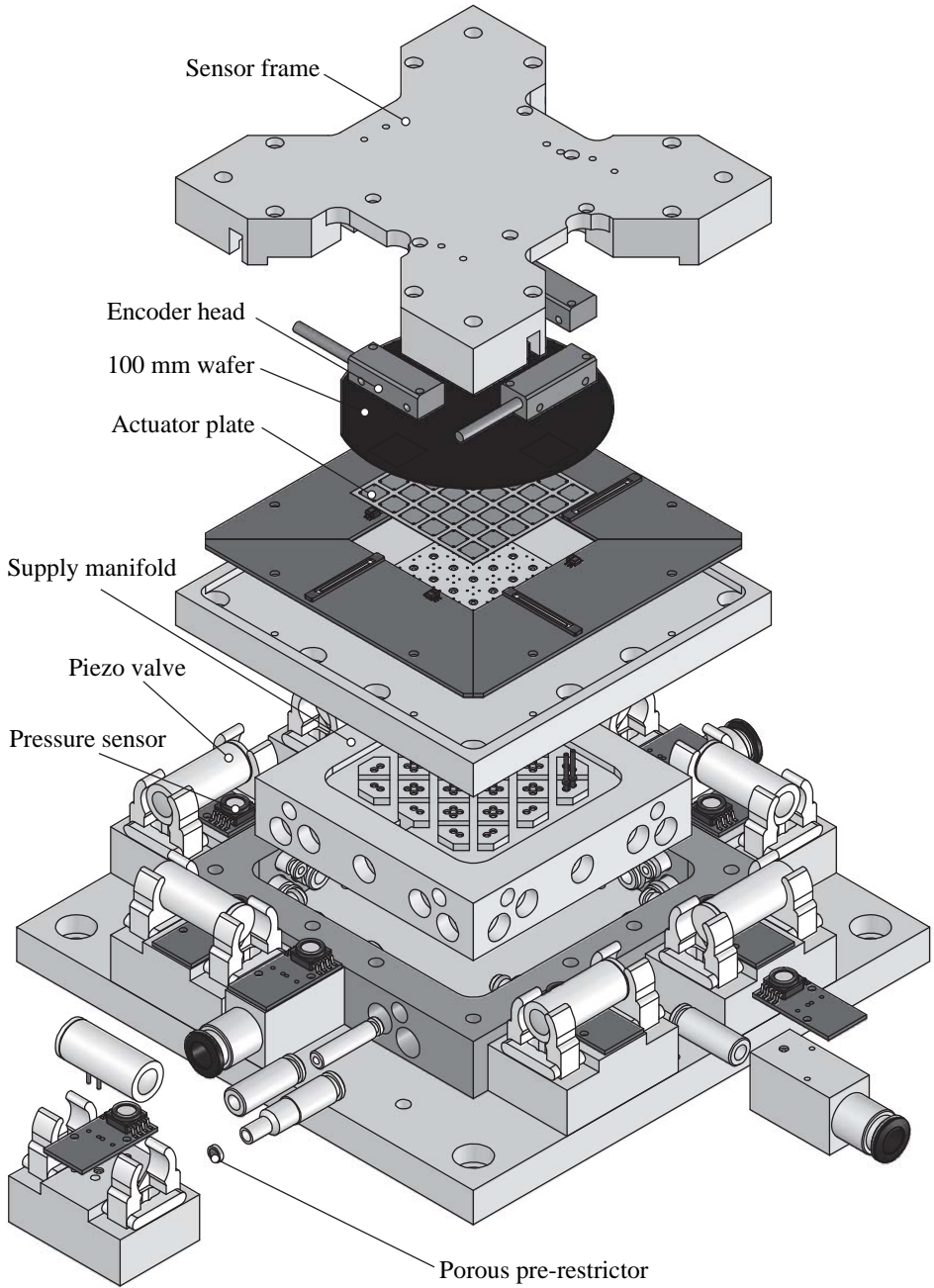


Figure A.6: Structure of Waferstage (source [56])

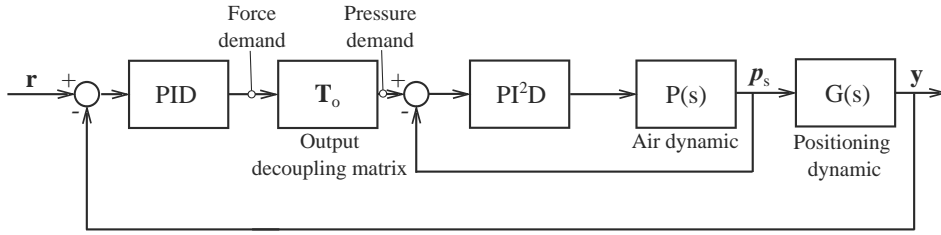


Figure A.7: The controller structured with two loops

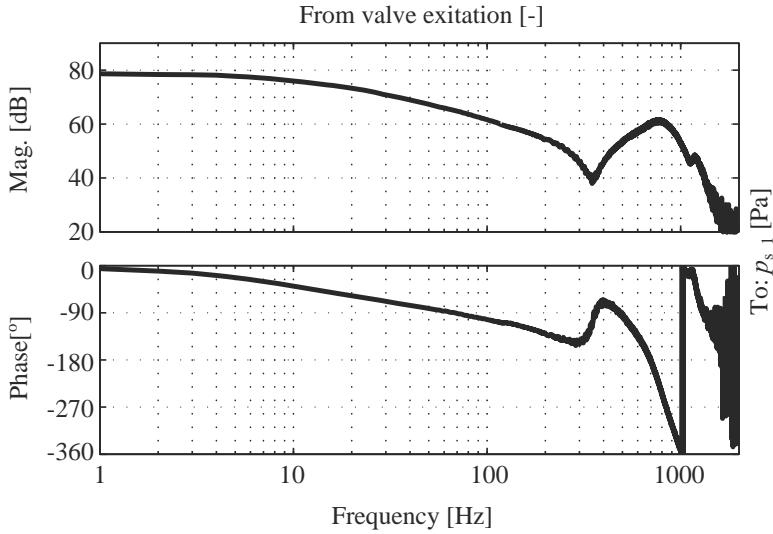


Figure A.8: Measured frequency response of one channel (source [56])

tracking performance. The maximum acceleration of the wafer is limited to 0.6m/s^2 because the valve saturation allows the inlet pressure to be controlled only in a range of $\pm 5\text{kPa}$ instead of $\pm 7.3\text{kPa}$ as designed. The maximum resulting force is $6.2 \cdot 10^{-3}\text{ N}$ instead of $15.5 \cdot 10^{-3}\text{ N}$ as predicted. This force limitation is not caused only by the reduction of the exciting range but also by the lower force constant. In this experiment, the estimated force constant reduces to $0.62 \cdot 10^{-6}\text{ NPa}^{-1}$ due to the fact that the wafer has to fly higher than designed. With the knowledge of maximum acceleration and maximum velocity, an input position profile and a feedforward controller have been added to the controller. Shown in Figure A.10, a 6 mm point to point move can be achieved within 270 ms with a maximum tracking error of $10\ \mu\text{m}$. To summarize, the realized performance of Waferstage is presented compared to the designed specifications in Table A.2.

A

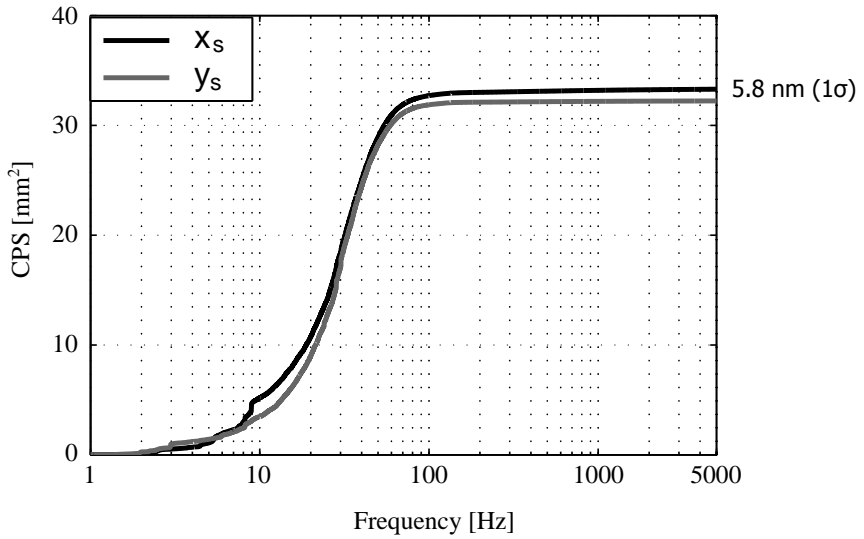


Figure A.9: Cumulative power spectrum of the servo error in standstill positioning case (source [56])

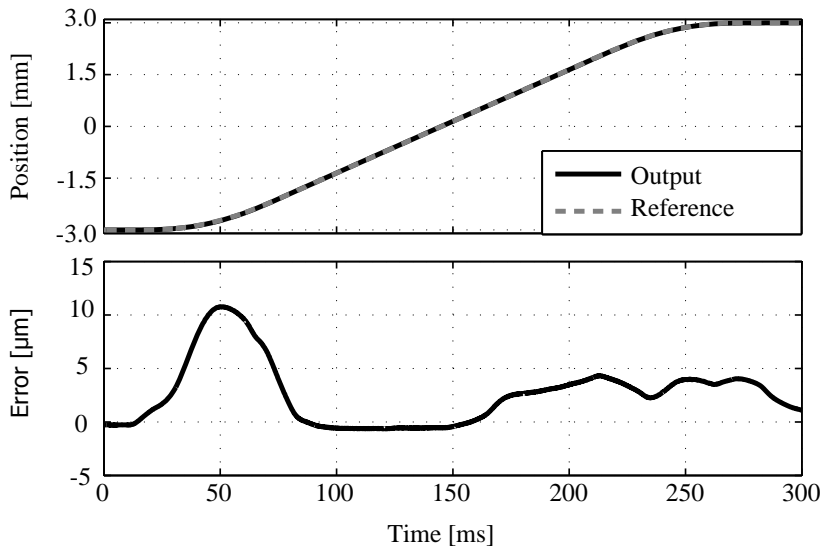


Figure A.10: Tracking performance with a max acceleration of 0.6m/s^2 (source [56])

Property	Designed	Realized
Fly height [μm]	10	15
Exciting range [kPa]	± 7.3	± 5
Force constant [N Pa^{-1}]	$1.062 \cdot 10^{-6}$	$0.62 \cdot 10^{-6}$
Max force [N]	$15.5 \cdot 10^{-3}$	$6.2 \cdot 10^{-3}$
Max acceleration [m s^{-2}]	1.5	0.6
Max velocity [m s^{-1}]	0.75	Not verified
Positioning accuracy [μm]	1.3	0.006
Bearing stiffness [Pa m^{-1}]	$525 \cdot 10^6$	Not verified

Table A.2: Realized performance of Waferstage

A.3. Conclusions and recommendations from previous research

From the research of Wesselingh et al. in this topic, some remarkable conclusions can be drawn:

- The new principle, using viscous traction force of thin air film flow, has been proven theoretically and experimentally to be applicable for contactless actuation systems, by which thin substrates can be handled without mechanical contacts.
- The force exerted on the substrate can be controlled by varying the pressure difference across the actuator pocket. A demonstrator, Waferstage, has been built successfully using this concept. The experimental result shows that the internal disturbances due to the air flow is negligible.
- Similar to conventional air bearings, the bearing stiffness created by this contactless actuation system is very high, more than sufficient to prevent mechanical contacts even when the substrate is not flat initially.

Still, there are some remaining questions that are interesting to investigate to understand more about this new actuation principle. Presented as following, some questions have been selected to be addressed in this thesis:

- Several actuator topologies have been presented in this research. However, a clear comparison has not been performed yet. There is room for exploring different actuator shapes and configurations.
- It has been stated that the performance of the air actuator array can be increased if the actuators are scaled down. The size of the actuator in this research is determined by manufacturing technologies. The questions: how to scale down the actuator? What is the appropriate pocket depth? How the dam width affect to the performance? are interesting but not answered yet by the research.
- The position control bandwidth is limited by the performance of the pressure control loop. In Waferstage, the pressure control bandwidth is limited to 120 Hz because of the dynamic behaviour occurring in the air channels when the control valves are placed externally. In order to increase the dynamic performance, it requires research on either small proportional valves that can be integrated near the air actuators or another concept that does not affected by the air dynamic inside the channels.

B

CLAMPING MODULE - THE THIRD METHOD OF FORCE CONTROL

During the analysis of the static performance of the actuators that use the principle presented in this thesis (Chapter 2 and 4), an interesting characteristic has been found that the force generated by an actuator is proportional to the actuator area and the relative vacuum, and not dependent on the inlet pressure. Formulating this understanding differently, the propulsion force can be considered to be proportional to the preload force. Therefore, the third method for controlling the propulsion force is introduced in this appendix: control by varying the preload force.

As shown in Figure B.1, if a substrate is clamped between two actuator arrays that are supplied with positive pressure p_s only, when the clamping force is zero, and the air gap is large, the inlet pressure in the film is equal to ambient pressure. The resulting propulsion force in this case is zero due to the fact that the pressure difference between the inlet and outlet (exhausts to ambient) in the film is zero. If the clamping force increases, the two actuator arrays move towards each other, resulting a reduction of the air gap thickness. When the gap thickness becomes sufficiently small, the pressure at the inlet in the film increases, and approaches p_s when the gap is close to zero. This increase of the inlet pressure results in an increase of viscous traction force, thus the propulsion force exerted on the substrate.

Since the actuator arrays in this concept still work similarly to a conventional air bearing, the bearing stiffness can be designed to be high. This means that the gap just varies slightly even when the clamping force changes in a wide range. Furthermore, because of this bearing stiffness, the substrate is balanced automatically between the two arrays. In this operating condition, as long as there is no contact between the substrate and the arrays, the force can be formulated by extending the analysis in Chapter 2 with a non-zero load capacity. For the tilt actuator array:

$$F_{\text{propulsion}} \approx \frac{d}{L} F_{\text{preload}} \quad (\text{B.1})$$

B

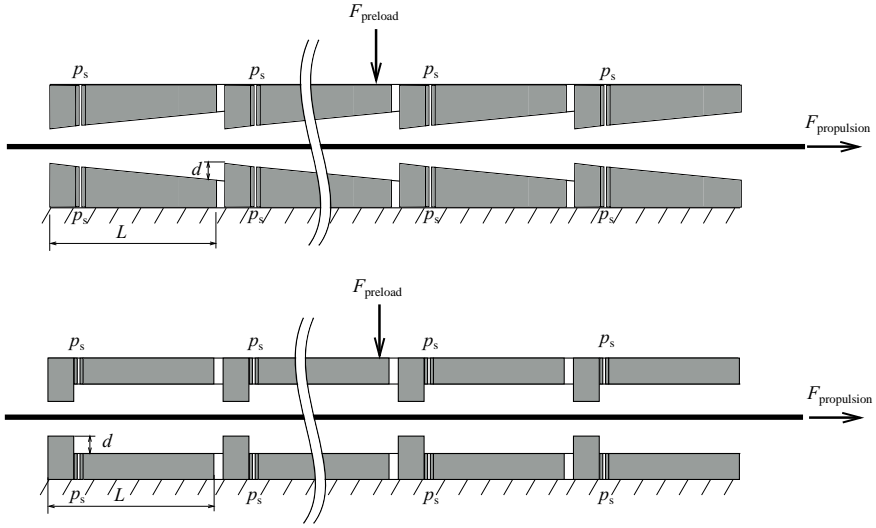


Figure B.1: The propulsion force can be controlled by varying the clamping force

And for the step actuator array:

$$F_{\text{propulsion}} \approx 2 \frac{d}{L} F_{\text{preload}} \quad (\text{B.2})$$

in which $F_{\text{propulsion}}$ is the total resulting force created on both sides of the substrate. d and L describe the geometry of each section as shown in Figure B.1. These formulas have been obtained for the case that ambient pressure is applied at the outlets.

At a glance, the first main advantage of this concept is the absence of the vacuum requirement. Because of that, the limit performance curve presented in the previous chapters of this thesis is not applicable. The challenges for designing such a system might be defined differently. Therefore, further research on this concept is recommended. The second advantage of this clamping concept is the possibility of handling very thin substrate. Since the two actuator arrays are identical, the resulting pressure distribution on both sides of the substrate is also identical, thus the substrate's deformation caused by the pressure is eliminated (theoretically). The only disadvantage of using this concept is that both sides of the substrate are (partially) covered by the transport system, and not fully available for processing steps. However, of course the property of zero mechanical contact is maintained.

NOMENCLATURE

α	Actuator geometry ratio in length (inlet position)	[-]
β	Actuator geometry ratio in height	[-]
φ	Tilt angle of actuator	[mrad]
η	Dynamic viscosity of air, taken as $18.2 \cdot 10^{-6}$	[Pa s]
ρ	Air density	[kgm ⁻³]
a	Mechanical amplifying ratio	[-]
d_a	Displacement created by a mechanical actuator (piezo type)	[m]
d_p	Displacement achieved at the movable plate	[m]
F	Traction force	[N]
\bar{F}	Traction force per unit area	[Nm ⁻²]
F_p	Force exerted on the movable plate	[N]
h	Fly height, defined as the smallest thickness of the air film	[μ m]
h_c	Fly height at the central point (inlet) of a tilted actuator	[μ m]
H	Function describing the air film thickness with respect to x	[-]
\bar{k}	Bearing stiffness per unit area	[Nm ⁻¹ m ⁻²]
k_a	Stiffness of a mechanical actuator (piezo)	[Nm ⁻¹]
k_s	Stiffness of the stem of 'flowers'	[Nm ⁻¹]
L	Length of an (contactless) actuator	[m]
L_s	Length of the stem of 'flowers'	[m]
m	Mass of the substrate	[kg]
\dot{m}	Mass flow rate	[kgs ⁻¹]
\bar{m}	Mass flow rate per unit area	[kgs ⁻¹ m ⁻²]
p	Pressure distribution in the air film	[Pa]
p^+, p^-	Inlet and outlet pressure (in the air film)	[Pa]
p_s	Supply pressure	[Pa]
p_v	Supply vacuum	[Pa]
R_i, R_o	Restriction of the inlet and outlet restrictors	[Pasm ⁻³]
R_a	Restriction of the actuator gap (air film)	[Pasm ⁻³]
R_g	Specific gas constant for air, taken as 287	[J kg ⁻¹ K ⁻¹]
S_a	Area of the bearing surface of an actuator	[m ²]
T	Temperature, taken as 293	[K]
U	Substrate velocity	[ms ⁻¹]
w	Bearing load capacity	[N]
\bar{w}	Bearing load capacity per unit area	[Nm ⁻²]

B

REFERENCES

- [1] International technology roadmap for photovoltaic-2014 results, 2014.
- [2] Farid Al-Bender. On the modelling of the dynamic characteristics of aerostatic bearing films: From stability analysis to active compensation. *Precision Engineering*, 33(2):117 – 126, 2009.
- [3] Farid Al-Bender and Hendrik Van Brussel. Tilt characteristics of circular centrally fed aerostatic bearings. *Tribology international*, 25(3):189–197, 1992.
- [4] DS Allen, PJ Stokes, and S Whitley. The performance of externally pressurized bearings using simple orifice restrictors. *ASLE transactions*, 4(1):181–196, 1961.
- [5] Wolfgang M Arden. The international technology roadmap for semiconductors—perspectives and challenges for the next 15 years. *Current Opinion in Solid State and Materials Science*, 6(5):371–377, 2002.
- [6] Andrew Berlin, David Biegelsen, Patrick Cheung, Markus Fromherz, David Goldberg, Warren Jackson, Bryan Preas, James Reich, and Lars-Erik Swartz. Motion control of planar objects using large-area arrays of mems-like distributed manipulators. *Xerox Palo Alto Research Center CA/USA, presented at Micromechatronics*, 2000.
- [7] Stephen Carey, D Martin Knotter, Eric Ooms, Johannes Boersma, Elfried van der Sar, Robbert Cop, Wim Gerritzen, Hans van Zadelhoff, and Henk Bouma. Yield impact of backside metal-ion contamination. In *Solid State Phenomena*, volume 187, pages 287–290. Trans Tech Publ, 2012.
- [8] Chien-Jen Chen and Daniel B DeBra. A laminar flow motor for precision machining. *CIRP Annals-Manufacturing Technology*, 36(1):385–390, 1987.
- [9] Bassem Dahroug, Guillaume J Laurent, Valérian Guelpa, Le Fort-Piat, et al. Design, modeling and control of a modular contactless wafer handling system. In *Robotics and Automation (ICRA), 2015 IEEE International Conference on*, pages 976–981. IEEE, 2015.
- [10] Guido MJ Delhaes, Anton van Beek, Ron AJ van Ostayen, and Robert H Munnig Schmidt. The viscous driven aerostatic supported high-speed spindle. *Tribology International*, 42(11):1550–1557, 2009.
- [11] D Dowson. A generalized reynolds equation for fluid-film lubrication. *International Journal of Mechanical Sciences*, 4(2):159–170, 1962.

B

- [12] Yamato Fukuta, Yoshio Mita, Makoto Arai, and Hiroyuki Fujita. Pneumatic two-dimensional conveyance system for autonomous distributed mems. In *TRANS-DUCERS, Solid-State Sensors, Actuators and Microsystems, 12th International Conference on, 2003*, volume 2, pages b1019–b1022. IEEE, 2003.
- [13] Daniele Gallieni and Roberto Biasi. The new vlt-dsm m2 unit: construction and electromechanical testing. In *Third AO4ELT Conference (Simone Esposito and Luca Fini, eds.), Proc. AO4ELT, AO4ELT*, volume 5, 2013.
- [14] Ulrich K Gengenbach and James C Boole. Electrostatic feeder for contactless transport of miniature and microparts. In *Intelligent Systems and Smart Manufacturing*, pages 75–81. International Society for Optics and Photonics, 2000.
- [15] Peter Glynne-Jones, Christine EM Démoré, Congwei Ye, Yongqiang Qiu, Sandy Cochran, and Martyn Hill. Array-controlled ultrasonic manipulation of particles in planar acoustic resonator. *Ultrasonics, Ferroelectrics, and Frequency Control, IEEE Transactions on*, 59(6):1258–1266, 2012.
- [16] W.A. Gross. *Gas film lubrication*. Wiley, 1962.
- [17] Roger Hamelinck, Rogier Ellenbroek, Nick Rosielle, Maarten Steinbuch, Michel Verhaegen, and Niek Doelman. Validation of a new adaptive deformable mirror concept. In *SPIE Astronomical Telescopes+ Instrumentation*, pages 70150Q–70150Q. International Society for Optics and Photonics, 2008.
- [18] Yoshiki Hashimoto, Yoshikazu Koike, and Sadayuki Ueha. Transporting objects without contact using flexural traveling waves. *The Journal of the Acoustical Society of America*, 103(6):3230–3233, 1998.
- [19] R John Hill. Teaching electrodynamic levitation theory. *Education, IEEE Transactions on*, 33(4):346–354, 1990.
- [20] T Hirata, T Akashi, A Bertholds, HP Gruber, A Schmid, MA Gretillat, OT Guenat, and NF De Rooij. A novel pneumatic actuator system realised by microelectro-discharge machining. In *Micro Electro Mechanical Systems, 1998. MEMS 98. Proceedings., The Eleventh Annual International Workshop on*, pages 160–165. IEEE, 1998.
- [21] Junhui Hu, Kentaro Nakamura, and Sadauki Ueha. An analysis of a noncontact ultrasonic motor with an ultrasonically levitated rotor. *Ultrasonics*, 35(6):459–467, 1997.
- [22] S Ishizawa, Tooru Watanabe, and Koji Takahashi. Unsteady viscous flow between parallel disks with a time-varying gap width and a central fluid source. *Journal of fluids engineering*, 109(4):394–402, 1987.
- [23] Jong Up Jeon and Toshiro Higuchi. Electrostatic suspension of dielectrics. *Industrial Electronics, IEEE Transactions on*, 45(6):938–946, 1998.
- [24] Jong Up Jeon and Toshiro Higuchi. Induction motors with electrostatic suspension. *Journal of electrostatics*, 45(2):157–173, 1998.

- [25] Ju Jin, Tachung C Yih, Toshiro Higuchi, and Jong Up Jeon. Direct electrostatic levitation and propulsion of silicon wafer. *Industry Applications, IEEE Transactions on*, 34(5):975–984, 1998.
- [26] Guillaume J Laurent, Anne Delettre, and Nadine Le Fort-Piat. A new aerodynamic-traction principle for handling products on an air cushion. *Robotics, IEEE Transactions on*, 27(2):379–384, 2011.
- [27] Hyung-Woo Lee, Ki-Chan Kim, and Ju Lee. Review of maglev train technologies. *Magnetics, IEEE Transactions on*, 42(7):1917–1925, 2006.
- [28] L. Licht, D. D. Fuller, and B. Sternlicht. Self-excited vibrations of an air-lubricated thrust bearing. *Trans.ASME*, 80(2):411–414, 1958.
- [29] Lazar Licht and Harold Elrod. A study of the stability of externally pressurized gas bearings. *Journal of Applied Mechanics*, 27(2):250–258, 1960.
- [30] Jonathan Luntz and Hyungpil Moon. Distributed manipulation with passive air flow. In *Intelligent Robots and Systems, 2001. Proceedings. 2001 IEEE/RSJ International Conference on*, volume 1, pages 195–201. IEEE, 2001.
- [31] D Farhadi Macheuposhti, N Tolou, and JL Herder. A review on compliant joints and rigid-body constant velocity universal joints toward the design of compliant homokinetic couplings. *Journal of Mechanical Design*, 137(3):032301, 2015.
- [32] P-Y Madec. Overview of deformable mirror technologies for adaptive optics and astronomy. In *SPIE Astronomical Telescopes+ Instrumentation*, pages 844705–844705. International Society for Optics and Photonics, 2012.
- [33] Asier Marzo, Sue Ann Seah, Bruce W Drinkwater, Deepak Ranjan Sahoo, Benjamin Long, and Sriram Subramanian. Holographic acoustic elements for manipulation of levitated objects. *Nature communications*, 6, 2015.
- [34] Lewis F Moody. Friction factors for pipe flow. *Trans. Asme*, 66(8):671–684, 1944.
- [35] Yoichi Ochiai, Takayuki Hoshi, and Jun Rekimoto. Pixie dust: graphics generated by levitated and animated objects in computational acoustic-potential field. *ACM Transactions on Graphics (TOG)*, 33(4):85, 2014.
- [36] Yoichi Ochiai, Takayuki Hoshi, and Jun Rekimoto. Three-dimensional mid-air acoustic manipulation by ultrasonic phased arrays. *PloS one*, 9(5):e97590, 2014.
- [37] Kristofer J Pister, Ronald Fearing, and Roger Howe. A planar air levitated electrostatic actuator system. In *Micro Electro Mechanical Systems, 1990. Proceedings, An Investigation of Micro Structures, Sensors, Actuators, Machines and Robots. IEEE*, pages 67–71. IEEE, 1990.
- [38] P Plessers and R Snoeys. Dynamic identification of convergent externally pressurized gas-bearing gaps. *Journal of tribology*, 110(2):263–270, 1988.

- [39] G Reinhart and J Hoeppepner. Non-contact handling using high-intensity ultrasonics. *CIRP Annals-Manufacturing Technology*, 49(1):5–8, 2000.
- [40] Gunther Reinhart, Michael Heinz, Johannes Stock, Josef Zimmermann, Michael Schilp, Adolf Zitzmann, and Jens Hellwig. Non-contact handling and transportation for substrates and microassembly using ultrasound-air-film-technology. In *Advanced Semiconductor Manufacturing Conference (ASMC), 2011 22nd Annual IEEE/SEMI*, pages 1–6. IEEE, 2011.
- [41] Gunther Reinhart, Juergen Hoeppepner, and Josef Zimmermann. Non-contact wafer handling using high-intensity ultrasonics. In *Advanced Semiconductor Manufacturing Conference, 2001 IEEE/SEMI*, pages 139–140. IEEE, 2001.
- [42] Hossein Rezaei and Sadegh Vaez-Zadeh. Modelling and analysis of permanent magnet electrodynamic suspension systems. *Progress In Electromagnetics Research M*, 36:77–84, 2014.
- [43] H. Richardson. Static and dynamic characteristics of compensated gas bearings. *Trans.ASME*, 80(2):1503–1509, 1958.
- [44] EOJ Salbu. Compressible squeeze films and squeeze bearings. *Journal of Basic Engineering*, 86(2):355–364, 1964.
- [45] R.M. Schmidt, G. Schitter, and A. Rankers. *The Design of High Performance Mechatronics - 2nd Revised Edition: High-Tech Functionality by Multidisciplinary System Integration*. IOS Press, 2014.
- [46] Jean-Christophe Sinquin, Jean-Marie Lurçon, and Claude Guillemard. Deformable mirror technologies for astronomy at cilas. In *SPIE Astronomical Telescopes+ Instrumentation*, pages 70150O–70150O. International Society for Optics and Photonics, 2008.
- [47] R. Snoeys and F. Al-Bender. Development of improved externally pressurized gas bearings. *KSME Journal*, 1(1):81–88, 1987.
- [48] A Kent Stiffler and Ricardo R Tapia. Amplitude effects on the dynamic performance of hydrostatic gas thrust bearings. *Journal of Tribology*, 101(4):437–443, 1979.
- [49] TB Stowell. Pneumatic hammer in a gas lubricated externally pressurized annular thrust bearing. *Journal of Tribology*, 93(4):498–503, 1971.
- [50] Takeshi Takaki, Shoji Tanaka, Tadayoshi Aoyama, and Idaku Ishii. Position/attitude control of an object by controlling a fluid field using a grid pattern air nozzle. In *Robotics and Automation (ICRA), 2014 IEEE International Conference on*, pages 6162–6167. IEEE, 2014.
- [51] Sadayuki Ueha, Yoshiki Hashimoto, and Yoshikazu Koike. Non-contact transportation using near-field acoustic levitation. *Ultrasonics*, 38(1):26–32, 2000.
- [52] R. A. J. van Ostayen. Apparatus for carrying and transporting a product, 03 2008.

- [53] Ron AJ van Ostayen, Jan van Eijk, and Rob H Munnig Schmidt. Contact-less thin substrate transport using viscous traction. In *Design, Control and Software Implementation for Distributed MEMS (dMEMS), 2012 Second Workshop on*, pages 14–21. IEEE, 2012.
- [54] Vincent Vandaele, Alain Delchambre, and Pierre Lambert. Acoustic wave levitation: Handling of components. *Journal of applied physics*, 109(12):124901, 2011.
- [55] Zuwen WANG, Shingo ISHIZAWA, and Koji TAKAHASHI. Unsteady viscous flow between two parallel disks with a time-varying gap width and central fluid source: The case in which the rate of flow from the source is forcibly varied with time. *JSME international journal. Ser. 2, Fluids engineering, heat transfer, power, combustion, thermophysical properties*, 33(3):446–453, 1990.
- [56] J. Wesselingh. *Contactless positioning using an Active Air Film*. PhD thesis, Delft University of Technology, 2011.
- [57] RR Whymark. Acoustic field positioning for containerless processing. *Ultrasonics*, 13(6):251–261, 1975.
- [58] Shao Jü Woo, Jong Up Jeon, Toshiro Higuchi, and Ju Jin. Electrostatic force analysis of electrostatic levitation system. In *SICE'95. Proceedings of the 34th SICE Annual Conference. International Session Papers*, pages 1347–1352. IEEE, 1995.
- [59] Ryuto Yano, Manabu Aoyagi, Hideki Tamura, and Takehiro Takano. Novel transfer method using near-field acoustic levitation and its application. *Japanese Journal of Applied Physics*, 50(7S):07HE29, 2011.
- [60] Rabah Zeggari, Reda Yahiaoui, Julien Malapert, and Jean-François Manceau. Design and fabrication of a new two-dimensional pneumatic micro-conveyor. *Sensors and Actuators A: Physical*, 164(1):125–130, 2010.

CURRICULUM VITÆ

Phuc Hong VUONG

23-11-1984 Born in Binh Duong, Vietnam.

Education

- 1999–2002 High School
Hung Vuong, Binh Duong, Vietnam
- 2002–2007 B.Sc. in Mechatronics
Ho Chi Minh city University of Technology, Faculty of
Mechanical Engineering, Ho Chi Minh city, Vietnam
- 2009–2011 M.Sc. in Mechatronics
Sungkyunkwan University, School of Mechanical Engineering,
Suwon, Korea
- 2011–2016 Ph.D. in Mechatronics
Delft University of Technology, Faculty of Mechanical, Maritime and
Materials Engineering, Delft, the Netherlands
Thesis: Air-based contactless actuation system for thin sub-
strates
Promotor: Prof. ir. R. H. Munnig Schmidt
Co-promotor: Dr. R. A. J. van Ostayen

Awards

- 2007 Wining “The most creative robot design” award
in Robocon, a Vietnamese national robot design competition
- 2013 Winning the first place in EUSPEN challenge,
a European competition in solving technical challenges

LIST OF PUBLICATIONS

1. M. Krijnen, **P. H. Vuong**, and R. A. J. van Ostayen, *Floating on a Flowerbed*, Mikroniek (a quarterly magazine for professionals in the field of precision engineering) (2016).
2. **P. H. Vuong**, R. A. J. van Ostayen, and R. H. Munnig Schmidt, *Using deformable surface for thin substrate transport and positioning system: Initial design and preliminary results*, In Proc. of the 14th EUSPEN International Conference, volume 2,(2014).
3. **P. H. Vuong**, R. A. J. van Ostayen, and R. H. Munnig Schmidt, *Deformable surface for a contact-less actuation system*, In Proc. of the ASPE Spring Topical Meeting: Precision Control for Advanced Manufacturing Systems, volume 55,(2013).
4. **P. H. Vuong**, R. A. J. van Ostayen, and R. H. Munnig Schmidt, *An apparatus for carrying and transporting a product*, European patent office,(2014).